NEXT GENERATION ADAPTIVE OPTICS

by

Colin G. A. Ross

Submitted in partial fulfillment of the requirements
for the degree of Doctor of Philosophy

at

Dalhousie University
Halifax, Nova Scotia
October 2020

This dissertation is dedicated to my uncle, Brian Beanlands, who inspired me to pursue a degree in sciences and engineering at a young age. As I sat there writing this, I realized how difficult it was to put in to words how you have affected my choices over the years. I was always conflicted between a degree in physics or engineering, but you have helped me to achieve the best of both worlds. As a kid, I remember seeing pictures of you on an ice breaker deploying equipment up north and I never forgot how this sparked a keen interest in me to pursue a career that enabled me similar opportunities. As the years went on and I developed a deeper understanding of your work, it became clear to me that I would tailor my future work in a way that would allow me to accomplish this goal. Whether it was reading papers at your dining room table, doing oceanography assignments in your office at BIO until late at night, or learning to program a microcontroller over the telephone on the completely opposite coast, you have always been there for me and taught me so much. For this I will always be grateful and will always strive to be someone you would be proud of. I love you Uncle Brian.

Table of Contents

List of Tables

List of Figures

ix

Abstract

Adaptive Optics (AO) is an integral part of modern astronomy. Current systems are pushing the limits of large diameter telescopes to achieve near diffraction limited performance. Historically, AO systems have been limited to a small field-of-view, a constraint that must be addressed to achieve the full capability of next-generation extremely large telescopes (ELTs) (e.g. Thirty Meter Telescope). As the size of the deformable mirror (DM) scales to meet the requirements of these large diameter telescopes, traditional technologies commonly employed on smaller telescopes are reaching their breaking point in terms of the number of high voltage connections and the overall power dissipation of the DM system.

This thesis addresses the need for a scalable DM electronics driver topology in high actuator count applications and provides the foundation for a science case targeted at resolving star-formation dynamics in the host galaxy of hyper-luminous quasi-stellar objects (HLQSOs) using adaptive optics. The DM driver explored in this thesis is the first effort towards a scalable low-voltage integrated solution for pairing with a low-voltage/current micro-electro mechanical system (MEMS) DM. A 9-channel prototype driver is shown experimentally to provide ± 20 μm of stroke on a Lorentz force MEMS actuator using a ± 5 mA current in a 0.1T magnetic field.

One of the main applications for this technology is future AO systems destined for ELTs, which will provide the resolution and sensitivity required to study host galaxy properties of systems containing extremely bright QSOs. In the second half of the thesis, a population of rare and extremely bright HQSOs and their host galaxy environments were explored to understand how the relationship between QSO luminosity and host galaxy IR luminosity scales to the most luminous HQSOs. This thesis finds that QSOs can continue to become more luminous while the host galaxies have reached their maximal SFR, and that only approximately 1/3 of our galaxies truly are abnormally luminous after accounting for the general trend in increasing LUV with LIR and the fractional of population expected have host galaxies in a starburst mode.

List of Abbreviations Used

Jy	Jansky (unit) [1 Jy $= 1 \times 10^{-26}$ W Hz^{-1} m^{-2}], spectral flux density.
k_b	Boltzmann constant [$k = 1.38 \times 10^{-23}$ J K^{-1}].
AU	Astronomical Unit [1 AU$=1.5 \times 10^{11}$ m], Earth to Sun distance.
pc	Parsec (unit) [1 pc $= 3.086 \times 10^{16}$ km], astronomical distance.
RDL	Redistribution Layer.
z	Redshift ($1 + z = \lambda_{\mathrm{observed}}/\lambda_{\mathrm{emitted}}$).
H$_2$	Molecular hydrogen.
SMURF	Sub-Millimetre User Reduction Facility.
AGN	Active Galactic Nuclei.
ALMA	Atacama Large Millimeter/submillimeter Array.
ALMA	ALTtitude conjugate Adaptive optics for the InfraRed.
AO	Adaptive Optics.
ASIC	Application-Specific Integrated Circuit.
CCD	Charge-Coupled Device.
CMB	cosmic microwave background.
CMOS	Complimentary Metal-Oxide Semiconductor.
DAC	digital-to-analog converter.
DM	Deformable Mirror.
DNTUB	Deep N-type Well.
DSP	Digital Signal Processing.
ELT	Extremely Large Telescope.
ESD	Electrostatic Discharge.
FoV	Field of View.
FWHM	Full Width at Half Maximum.
GLAO	Ground Layer Adaptive Optics.
HLQSO	Hyper-Luminous Quasi-Stellar Object.

HV	High-Voltage.
IFS	Integral Field Spectroscopy.
IR	Infrared.
ISM	interstellar medium.
JCMT	James Clerk Maxwell Telescope.
KBSS	Keck Baryonic Structure Survey.
LGS	Laser Guide Star.
MCAO	Multi-Conjugate Adaptive Optics.
MEMS	Micro-Electro Mechanical System.
NGS	Natural Guide Star.
ALMA	Near-Infrared Integral Field Spectrometer.
NMOS	N-type Metal-Oxide Semiconductor.
PMOS	P-type Metal-Oxide Semiconductor.
MOS	Multi-Object Spectroscopy.
PSF	Point Spread Function.
PWM	Pulse-Width Modulation.
PWV	Precipitable water vapour.
QSO	Quasi-Stellar Object.
SCAO	Single Conjugate Adaptive Optics.
SCUBA-2	Submillimeter Common-User Bolometer Array 2.
SED	spectral energy distribution.
SFR	Star Formation Rate.
SHWFS	Shack Hartmann Wavefront Sensor.
SMBH	Supermassive Black Hole.
SPI	Serial Peripheral Interface.
SR	Strehl Ratio.
SQUID	Superconducting Interference Device.
TES	Transition Edge Sensor.
TSV	Through-Silicon Via.
VLA	Very Large Array.
WFS	Wavefront Sensor.

Acknowledgements

First and foremost, I would like to thank my supervisor, Scott Chapman. To say you have provided me with incredible opportunities would be an understatement. From working on a mountain top in the Andes conducting CMB polarization experiments, to visiting some of the top research institutes around the word, you have shown me that you can make a career out of doing what you love.

I will never forget the first day we met and the chance you took on a recent graduate with very little knowledge in astronomy. For this, I will be forever grateful. Since that day, you have supported me to explore my research interests and provided me with the guidance and freedom to develop as a researcher and person. Not once did I feel like a student working for you, rather an equal and collaborator whose input was truly valued.

Throughout the years, you have become much more than a supervisor to me. You have taught me to take advantage of opportunities and to never shy away from a challenge. I could not have asked for a better supervisor, and I am proud to call you my friend. I look forward to a future of collaborating.

I would like to extent a special thank you to my co-supervisor, Kamal El-Sankary. Without your support, much of the work presented in this thesis would not have been possible. When approached with the very ambitious project of helping a non-electrical engineering student design, fabricate, and test an IC, you accepted the challenge without hesitation. You welcomed me into your group with open arms and made me feel at home. Your patience and passion for teaching extends far beyond this work and has positively impacted the future of many students. From helping me the night before my first chip submission into the wee hours of the morning to our time spent together outside of the university, you have played a critical role in my success and motivate me to be a better researcher. For this, and all our future work, I thank you my friend.

Thank you to my collaborators on this work, Greg Burley and Byoungyoul Park. Greg, your leadership, and continued support on this project has made it the success

it is today. I thank you for the multiple trips to Halifax that you spent helping me test the IC and for not loosing confidence when things did not go as planned. Byoungyoul, your interest in the IC driver development and the time spent with me ensuring the device would meet the requirements of the MEMS DM, enabled us to demonstrate the potential of these types of technologies. Your incredible work on MEMS DM technology is what inspires me to continue developing the technology explored in this thesis, and I hope we can continue to work alongside one another to see this through to maturity.

To my lab mates in the Dunn Building and Sexton campus, I could not have done this without you. Kaja Rotermund and Kevin Lacaille, you have been with me since the beginning and I will never forget our time spent in the basement of the Dunn and local pubs. Your support, both academically and beyond, has played a critical role in helping me through my masters and doctoral studies. Alexey Tikhomirov, I can honestly say I do not know what I would have done without your support and willingness to help me without hesitation. I will never forget our conversations in your office, sharing stories of our travels, fixing broken lab equipment, and working together to design and assemble cryogenic equipment. You have helped shape me a researcher and provided me with the skills to succeed in many industries. Karama Al-Tamimi and Tejinder Sandhu, you welcomed me into your microelectronics research group as if I was there since the first day and spent countless hours helping me learn everything I needed to successfully design, fabricate, and test an integrated circuit. You have shown me that there is a world outside of academia and I know we will one day find an opportunity to build a successful business. I consider each of you a friend for life.

Thank you to all my collaborators on the Polarbear project. While the topic of this thesis was not directly related to our work together, my time spent working with you represents a significant part of my academic career and has made its way into this work in many respects. Kam Arnold, Bryan Steinbach, Dave Boettger, Praween Siritanasak, Greg Jaehnig, Toki Suzuki, Darcy Barron, and Nathan Stebor, your continued support and mentorship has played a critical role in my life. Our time in Chile is one of my most memorable experiences and I hope we can work together

again one day. I would also like to thank Nolberto Oyarce and Jose Cortes for always making me feel at home when I travelled to San Pedro de Atacama.

Thank you to my committee members, Theodore Monchesky and Philip Bennett, as well as my external examiner, David Andersen, for their support and thorough review of this thesis. Your contributions have bettered this work.

Tanya Timmins, you have saved me more than once! Whether it was a registration deadline, or an issue with paperwork, I could always count on your support. I will miss our conversations in the office and hearing your laugh. It always brightened my day.

To my family and friends, you are my source of motivation and my rock. You have been with me since the beginning and will continue to be with me far beyond the end. Regardless of the time of day or distance between us, I knew I could count on your support. You kept me on track, helped me see the light at the end of the tunnel when things seemed impossible, and made me realize the important things in life. To my parents Laurel and Ian, and my sisters, Molly and Heather-Anne, you are the reason I am proud to be the person I have become. You allowed me to take risks, explore opportunities as they arose, and allowed me to achieve this incredible accomplishment. I love you all and know that I will be always be here to return the favour.

Last and certainly not least, I want to thank by beautiful girlfriend, Kathleen Higgins. You have always supported me, even when that meant putting things on hold in your life. I love you and I look forward to our future together.

Chapter 1

Introduction

1.1 Motivation

"Adaptive Optics is a prime example of how progress in observational astronomy can be driven by technological developments." [1]

Ground-based telescopes suffer from blurring effects introduced by the incident light having to pass through the Earth's atmosphere. To help mitigate this effect and improve image quality, astronomers rely on AO to compensate for the wavefront distortions. The role of AO in ground-based astronomy is to enable comparable resolution to space-based instruments in the presence of the Earth's atmosphere. Light passing through the atmosphere will be distorted by turbulence, which acts like a series of small lenses introducing spatial and temporal variations in the refractive index along the line of sight. AO attempts to correct for these distortions by sensing the incoming wavefront and determining an appropriate correction. This method uses a wavefront sensor (WFS) to observe a bright reference star that is close to the object of interest from which a set of commands can be derived and applied to a DM. The net result is a much sharper image than would otherwise be possible.

AO technology has been successfully implemented on 8-10-meter class telescopes, enabling astronomers to achieve sharp diffraction-limited images. However, expanding science questions are driving the development of the next generation of large diameter telescopes, called Extremely Large Telescopes (ELTs), with primary mirror sizes greater than 20-meters. To exploit the potential gains in spatial resolution inherent to larger diameter telescopes, scientists and engineers need to develop new technologies. One of the key development areas is in DM technology, and solutions using MEMS are proving to be very promising.

MEMS offer many desirable properties, such as reduced manufacturing costs, high actuator count, and compactness. When used in parallel with a low-order, large

---

[1] Robert K. Tyson. *Principles of Adaptive Optics.* 2015

stroke DM acting as a "woofer" stage, MEMS DM technologies offer a sufficiently large actuator stroke and reduced voltage driving requirements. One of the most significant drawbacks, which is common to all technologies, is that with increased actuator count, comes an increase in the number of control signal wires. Thus, scaling of this technology to high actuator count arrays requires research and development into compatible drive electronics.

Current MEMS DMs use piezoelectric materials to achieve actuation and require high-voltage drive electronics that occupy a large amount of space. These electronics not only add to the overall complexity of the system but draw a significant amount of power. Scaling to higher-order DM systems has prompted research into low-voltage (and low-current) actuation approaches that require dedicated electronics to complement emerging MEMS DM technologies.

The availability of AO systems on 8-10 meter class telescopes provides astronomers with the unique ability to study distant objects with high spatial resolution. Of particular interest to this work is the ability to directly detect and characterize the quasar or quasi-stellar object (QSO), host galaxies. QSOs have long been ideal targets to study the evolution of structure in the universe due to their high, sustained luminosity across the spectrum. They are also excellent targets for AO studies because of their point-source-like nature and the ability to use the quasar as a bright natural guide star (NGS). Today, most scientists believe that a supermassive black hole (SMBH) at the galactic centre acts as the "engine" that powers these quasars. When the light generated by accretion of mass into the SMBH outshines the host galaxy, these objects are called active galactic nuclei (AGN). The SMBH at the centre of the galaxy is called a quasar, which is one type of AGN. A study by Harris et al. (2016) suggests there is evidence, at all redshifts (z), for a deep connection between star formation in galaxies, and the presence and properties of AGN in their centres (Harris et al., 2016). The former is quantified using the star formation rate (SFR), while the latter is quantified using the luminosity of the AGN. Since the same cold gas supply fuels both processes, one would expect, to first order, a connection between the two processes. Although rare in our local volume of space, the density of luminous AGN rises sharply going back in time to a redshift between 2<z<3 (e.g. Richards et al. 2002; Delvecchio et al. 2014). The cosmological evolution of star formation in galaxies

shares an approximately coeval peak in activity of around z=2 (Madau & Dickinson, 2014). Observations often find luminous star formation and AGN in the same galaxies at significantly higher rates than expected, suggesting that this is not by chance (e.g. Wang et al. 2013; Farrah et al. 2013; Casey et al. 2014; Pitchford et al. 2016). Studies have also shown that the mass of the black hole is proportional to the velocity dispersion of the stars (Magorrian et al., 1998), which suggests a link between the growth of the black hole and the stellar mass of the galaxy. As a result, observing a quasar results in observing its host galaxy at a critical period in its evolution.

The work presented in this thesis addresses (i) the need for efficient drive electronics, including prototype application-specific integrated circuit (ASIC) design and fabrication using a complimentary metal-oxide semiconductor (CMOS) process. Packaging options will also be explored, as this is a key element to making MEMS DM/ASIC technology a feasible solution (ii) the link between star-formation and AGN in QSO host galaxies at the epoch of maximum activity.

1.2   Thesis Structure

This thesis is comprised of 6 chapters, including the conclusion (Chapter 6). Chapter 2 introduces AO in the context of astronomical applications, beginning with an overview of classical implementations, the limitations of these systems, and then proceeds to discuss the unique challenges of developing complex AO architectures for ELTs. Chapter 3 discusses the design, fabrication, and testing of dedicated drive electronics that will enable high actuator count, low-voltage micro electro-mechanical systems (MEMS) to improve the performance of DMs. The work presented in this chapter represents a significant technology contribution to the development of next-generation AO instruments with applications for both ground-based and space-based telescopes. Previous efforts in this field have been focused on high-voltage implementations, while this work builds the foundation for a fully integrated and packaged, low-voltage MEMS DM with dedicated IC driver electronics. In addition to its application in the field of astronomy, the IC driver presented in this work represents a niche contribution to the field of micro-electronics, developing a high-voltage CMOS architecture with multi-level, bipolar supplies. Chapter 4 shifts the focus of the thesis to the science behind submillimetre studies of QSOs and their host galaxies. These types

of studies are critical to understanding the link between star-formation and AGN in QSO host galaxies at the epoch of maximum activity since QSOs are sufficiently bright to be detected at large distances. Chapter 5 presents an analysis of the submillimetre properties of 15 hyper-luminous quasi-stellar objects (HLQSOs) that were previously detected in a unique spectroscopic survey of the distant universe. Sensitive submillimetre observations are used to probe the dust properties of the galaxies that host the rare QSOs to explore the relationship between star-formation and AGN activity. The sample of sources targeted in this study represent an ideal candidate population for performing AO follow-up observations to resolve star-formation dynamics in the host-galaxy. The core technology and science chapters are based on two separate publications and contain conclusions at the end of the respective chapters. Finally, Chapter 6 will conclude the thesis and summarize the next steps for future research.

Chapter 2

Adaptive Optics and Astronomy

2.1 Introduction

Tyson defines adaptive optics as a subset of the much broader field of active optics, which deals with the control of light in a real-time closed-loop fashion (Tyson, 2015). This definition has held true since Babcock (1953) first proposed the use of a deformable optical element using feedback from a wavefront sensor to compensate for atmospheric turbulence in 1953 (Babcock, 1953). The field has since come a long way and follows closely with advances in technology. Combining expertise from both science and engineering disciplines, AO has enabled astronomers to observe distant and faint objects in much greater detail than previously thought possible with ground-based telescopes. More recently, the focus of AO has been on its application to large diameter telescopes (>20 meters) to exploit potential gains in collecting area and spatial resolution. To accommodate the larger field-of-view inherent to this new class of telescopes, the definition AO has since evolved to include open-loop approaches.

The role of AO in ground-based astronomy is to enable comparable resolution to space-based instruments in the presence of the Earth's atmosphere. Light passing through the atmosphere will be distorted by turbulence, which acts like a series of small lenses introducing spatial and temporal variations in the refractive index along the line of sight. AO attempts to correct for these distortions by sensing the incoming wavefront and determining an appropriate correction. The process begins by using a wavefront sensor to observe a bright reference star close to the object of interest from which a subsequent set of commands can be derived and applied to a deformable mirror. The net result is a much sharper image than would otherwise be possible.

2.2   Telescope Resolution

When designing a telescope, the goal is to achieve the highest possible spatial resolution, which has an upper limit imposed by the wave nature of light, causing diffraction. This limit, known as the diffraction limit, is defined as the angular distance from the centre of an image to the first zero of its diffraction pattern when viewing a point source. For space-based instruments, it is imperfections in the telescope's optics that ultimately limit the resolution of the telescope. By machining optical components to high tolerances, the impact of non-deal optics becomes minimized. Unfortunately for ground-based instruments, it is not as simple, since it is the highly dynamic atmosphere that limits the performance of the optical system.

When a telescope focuses a point source (e.g., a distant star), the response can be characterized by the point spread function (PSF). Diffraction causes the observed PSF to be a two-dimensional distribution of light at the focal plane, which depends on the size and shape of the telescope's aperture and the observed wavelength. The PSF of an imaging system with perfect optics, a circular aperture, and no atmosphere, will produce a response due to diffraction known as the Airy pattern. This pattern, shown in figure 2.1, has a bright central peak, followed by a series of maxima and minima. The angular resolution of a telescope was defined by Lord Rayleigh as the distance to the first minima, yielding the following expression:

$$\theta = 1.22 \frac{\lambda}{D} \tag{2.1}$$

This quantity gives the minimum angular separation between two points sources that a telescope can observe as two separate images (Rayleigh criterion). In the absence of AO, increasing the diameter of a ground-based telescope will only increase the sensitivity (i.e., the light-collecting power). To increase the resolving power of a telescope in the presence of the turbulent atmosphere and fully realize the gains of a large-diameter primary mirror, astronomers must rely on AO.

(a)

(b)
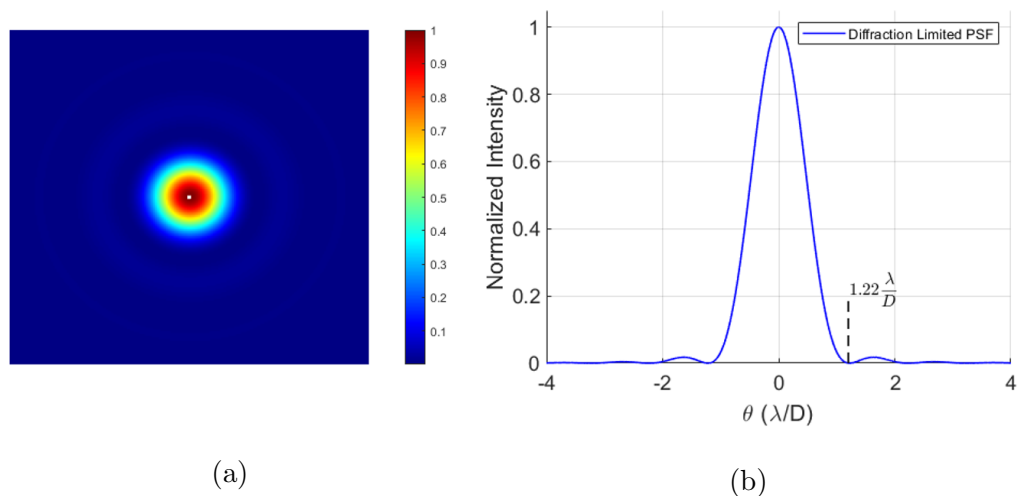
Figure 2.1: Diffraction-limited telescope resolution and point spread function. Left: Airy Pattern for an idea circular aperture. Right: Cross-sectional profile of the Airy disk through the origin, showing the diffraction-limited PSF.

(a)

(b)
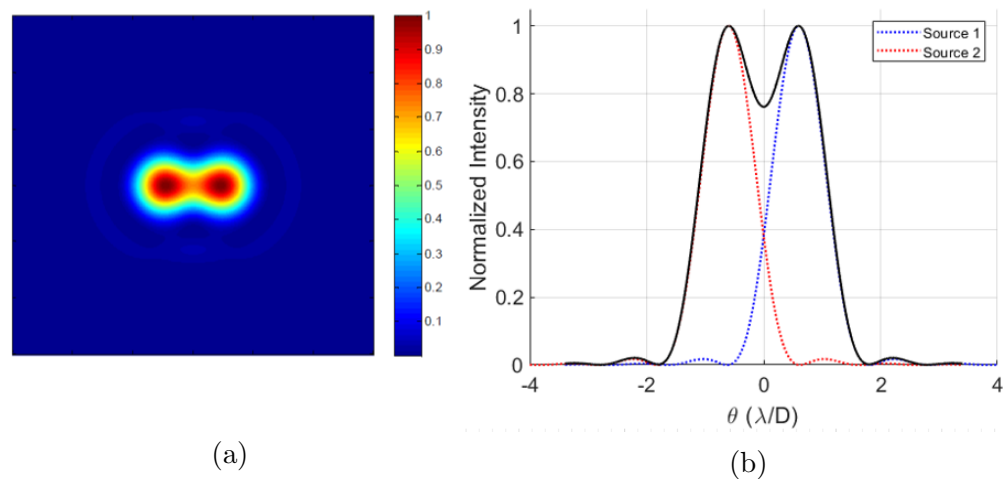
Figure 2.2: Rayleigh resolution criterion for two point sources. Right: Left: Summed intensity profile (black curve) of two distant point sources (blue and red dotted curves) with a distance according to the Rayleigh criterion.

2.3 Atmospheric Turbulence

Atmospheric turbulence is the result of multiple atmospheric processes working together to mix air parcels of different temperatures, and therefore density. These processes include convection, wind shear, and mechanical mixing. Convection is driven by solar heating of the Earth's surface, causing parcels to become more buoyant and rise, forcing parcels with colder temperatures to descend. This process has a diurnal variation and is dominant in the first few hundred meters of the atmosphere (Max, Max). If there is a strong enough vertical gradient in the horizontal wind velocity, then wind shear can also drive energy transfer between adjacent layers in the atmosphere, thereby creating turbulent mixing. Finally, the presence of an observatory or other structures can induce mechanical mixing of the air by disturbing the flow. Studies have shown that most turbulence resides within the first 15 km of the atmosphere (Max, Max).

Turbulence impacts the optical performance of a telescope by blurring the image of a point source. This effect, called atmospheric seeing, is typically characterized by the full width at half maximum (FWHM) of the observed PSF. The PSF will be altered from the ideal case by slight changes in atmospheric density that lead to variations in the index of refraction. The effect of turbulence, illustrated in figure 2.3, is a degradation in image quality. Turbulence causes incident light waves to encounter variable optical paths as they travel through a series of density-induced lenses. In adaptive optics, the seeing limit is:

$$R = \lambda/r_0 \tag{2.2}$$

where R is the telescope spatial resolution in the presence of turbulence. The Fried parameter (r_0), or commonly, the coherence length, is used as a descriptor to quantify the turbulence strength. Following from the atmospheric coherence length and knowledge of the wind velocity to define the timescale over which turbulence changes. The turbulence time constant for the atmosphere, τ_0, can be estimated using the following formula:
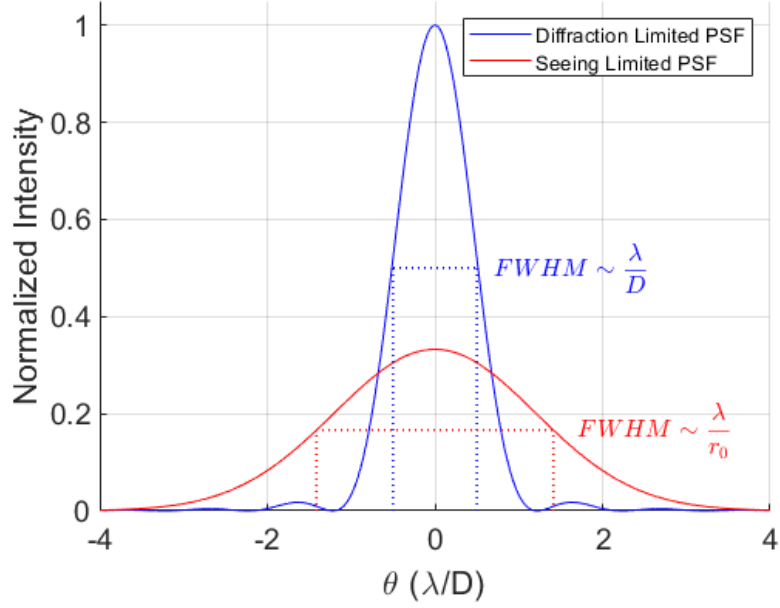
Figure 2.3: Illustration showing the impact of imaging through the Earth's atmosphere. The diffraction-limited PSF (blue) and the 'seeing limited' PSF as observed through the atmosphere.

$$\tau_0 = 0.31 \frac{r_0}{\bar{V}} \tag{2.3}$$

where $\bar{V}$ is the velocity of the wind averaged over a particular altitude. The atmospheric time constant is important because it defines how fast an AO system must respond to compensate for the turbulence.

One common observation is variable brightness (called scintillation) when viewing a star, and is the result of interference between the incident waves propagating through different atmospheric paths. Another observation is speckling, which arises from the temporal behaviour of the atmosphere, causing the apparent position of a point source on the sky to vary. By placing telescopes on high mountain tops where atmospheric contributions play a minimal role, astronomers can partially mitigate these effects.

2.4 Adaptive Optics Systems

Even the best ground-based observing sites suffer from image blurring due to the Earth's atmosphere. As light from a distant star (i.e., a point source) enters the atmosphere, the planar wavefront is subject to index of refraction variations that result from small scale temperature fluctuations in the air. The effect of this turbulence is to introduce phase distortions in the wavefront, called aberrations. When the light finally reaches the telescope, it has been refracted many times and cannot be focused to a point since the rays are no longer parallel. The result is a degradation in image quality due to the blurring of the PSF beyond the desired diffraction limit. In the absence of AO, ground-based telescopes are limited to the resolution of one with an approximately 20-cm diameter primary mirror. The role of AO is to sense the changes introduced by the atmosphere and correct for it before imaging, allowing larger diameter telescopes to realize both increases in sensitivity and resolution.

2.4.1 Introduction to Classical Adaptive Optics

Classical adaptive optics refers to the closed-loop implementation traditionally used for correcting over a small field of view. The key components are a WFS, wavefront corrector (typically a DM), and a control system that converts WFS data into a set of commands to apply to the DM. AO systems rely on bright reference targets (i.e., guide stars) that are close to the source to characterize the distortions in a wavefront. The availability of suitable bright guide stars imposes a strict set of limits on the useable sky coverage. In an ideal world, there would be plenty of bright astronomical targets (called natural guide stars (NGSs)). Unfortunately, only a small portion of the sky (approx. 10%) contains bright enough stars (R_{mag} ~15) to be suitable for correction. To overcome this issue, modern AO makes use of high-powered lasers to create artificial guide stars (called laser guide stars (LGSs)).

LGS function by either measuring Rayleigh back-scatter from laser light focused to an altitude of approximately 20 km in dense regions of the atmosphere, or by exciting specific sodium lines in the atmosphere at an altitude of 90 km. These approaches help increase the total usable sky coverage but come with drawbacks that are explored in section 4.5.
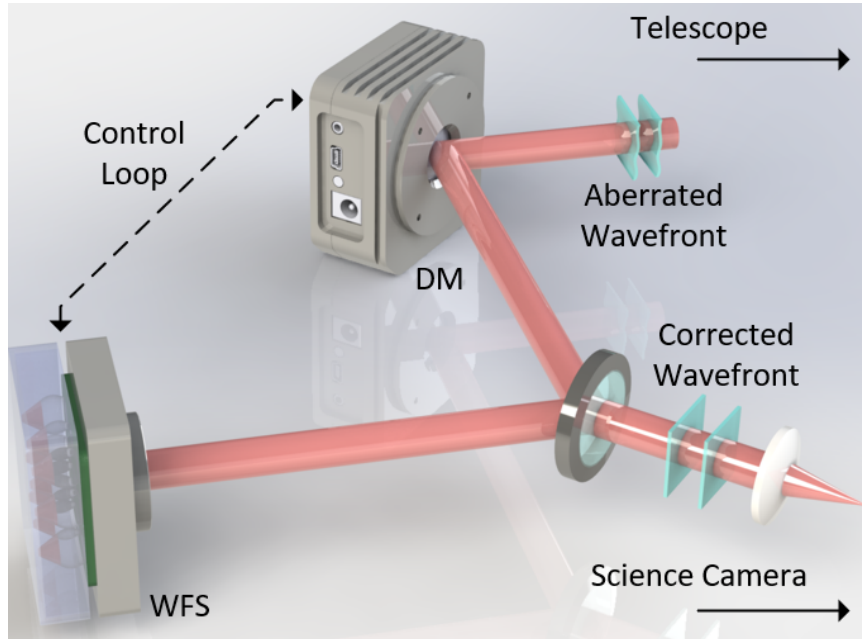
Figure 2.4: Block diagram of an AO system used for ground-based telescopes. Components include a deformable mirror, wavefront sensor and a science imaging camera. Image drawn by author using Dassault Systèmes SOLIDWORKS.

A block diagram showing a generic AO system is presented Fig 1. The distorted wavefront is focused from the telescope's primary mirror to the DM, which is continually updating the shape of its surface such that it attempts to null the influence of atmospheric turbulence. The next optical element is a beam splitter that sends part of the light to the wavefront sensor for measuring the residual wavefront and updating the DM commands, and part of the light to the science camera for final imaging.

2.4.2 Wavefront Sensing

Most WFS's do not measure the wavefront phase directly. Instead, the intensity distribution on a charge-coupled device (CCD) detector is measured, and the wavefront phase is reconstructed. A standard WFS consists of three core components: (i) An optical device that transforms the wavefront aberrations into intensity variations in the incoming light. (ii) A detector (typically a CCD) that converts the light intensity distribution into an electrical signal that a computer can interpret. (iii) An external real-time computer, which performs wavefront phase reconstruction.

In general, all WFS's work by converting light intensity differences in sub-regions
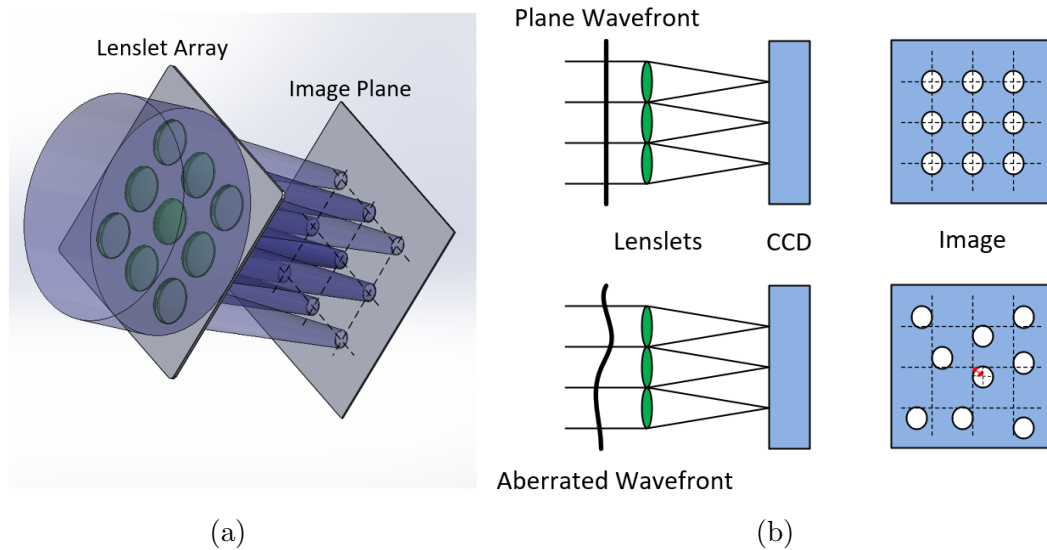
Figure 2.5: Shack–Hartmann wavefront sensor operation principle. An array of lenslets focuses incoming light into a series of spots on a CCD camera. The displacement of the centroid (red arrow) is used to calculate the slope of the incoming wavefront. Right: 3D rendering of lenslet array. Left: Top- Uniform spot distribution created from a plane wavefront. Bottom- Displaced spot distribution due to turbulence. Image inspired by Andrei Tokovinin's AO Tutorial[1].

of the telescope's aperture into phase differences across the full telescope aperture. Several types of WFS architectures exist for recovering the wavefront phase, the most common of which is the Shack Hartmann Wavefront Sensor (SHWFS). A SHWFS uses an array of small lenses (called lenslets) to subdivide the telescope aperture into smaller regions (called SH spots). These spots are then projected onto a common CCD detector to form an array of images. A plane wavefront will produce an image geometry with SH spots sitting on an equally spaced grid. However, as atmospheric turbulence distorts the incoming wavefront, the image centroids are displaced from their normal grid location. Total spot displacement is proportional to the gradient (or slope) in the wavefront in that sub-region. The slopes are calculated in each sub-region and then combined to define the phase of the wavefront over the whole telescope aperture.

Curvature sensors are another type of WFS that functions similarly to the SHWFS. Instead of measuring the position of the SH spots to determine the slope of the wavefront, it measures the intensity of light on two imaging planes (before and after the

---

[1] http://www.ctio.noao.edu/~atokovin/tutorial/part3/wfs.html.
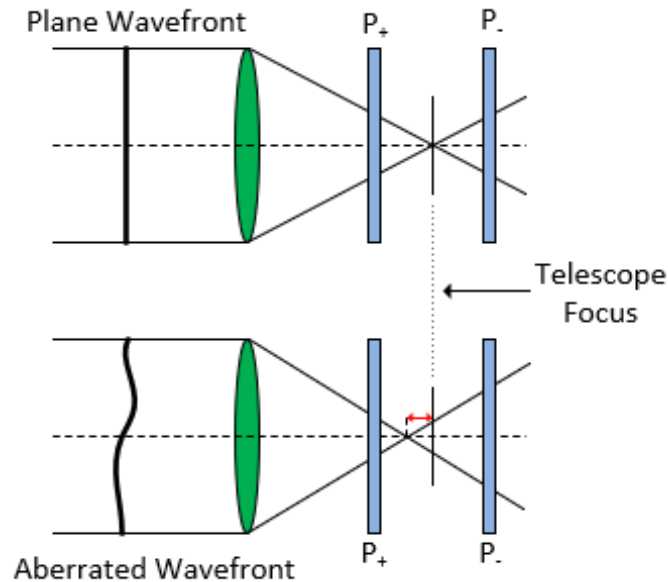
Figure 2.6: Curvature wavefront sensor operation principle. The intensity distribution is measured at planes (P_+ and P_-) on either side of the telescope's nominal focus. Top: A wavefront with no curvature will produce identical distributions at both planes. An aberrated wavefront will cause relative changes in the intensities measured at the two planes as the focal spot moves along the optical axis. Image inspired by Andrei Tokovinin's AO Tutorial.

standard telescope focus) to measure the curvature. Turbulence causes opposing intensity changes in the two planes as the telescope focus shifts along the optical axis. The relative intensity measured in the two imaging planes is then used to determine the phase of the wavefront.

The last type of commonly used WFS is the pyramid WFS, which uses an optical pyramid to subdivide the telescope aperture into four sub-regions and project the images onto a CCD camera. For a plane wavefront, all four image regions experience an identical flux of light. However, when turbulence comes into play, the sub-regions exhibit different intensities relative to one another that are proportional to the slope of the wavefront.

2.4.3 Wavefront Correction

Wavefront correction is achieved using an optomechanical device called a deformable mirror. The DM is an integral part of any AO system, enabling phase distortions to be corrected or nulled. The device functions by actively changing the shape of
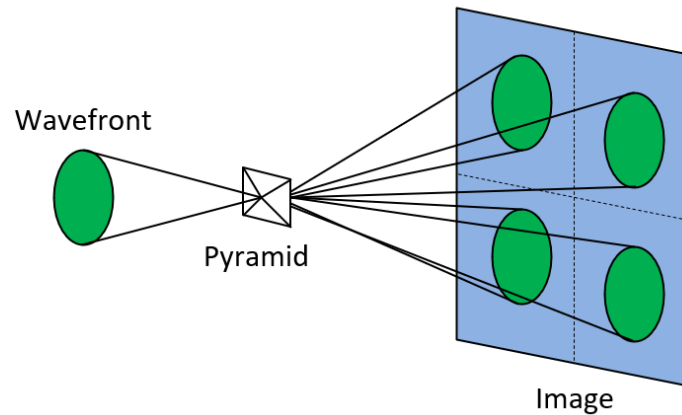
Figure 2.7: Pyramid wavefront sensor operation principle. An optical pyramid is placed in the focal plane to produce four copies of the telescope pupil on the same CCD. A plane wavefront will produce four sub-apertures with identical intensities. An aberrated wavefront will cause the four sub-apertures to have varying intensities. Image inspired by Andrei Tokovinin's AO Tutorial.

its reflective surface according to output from a WFS. The mirror surface can be either segmented or continuous, and many different technologies exist for achieving actuation.

The following is a list of common DM types:

- Adaptive or deformable secondary mirrors:

    - Used to replace the static secondary mirror on the telescope

    - Use thin optical shell paired with an array of voice coil actuators

    - Large actuator stroke (can correct for low order aberrations)

    - Complex and consume a lot of power

- Piezo stacked array DM:

    - Stack layers of piezoelectric or electroresistive material

    - Variable stroke depending on the application

    - Require large driving voltages

- MEMS DM:

    - Electrostatic and magnetic field-driven actuation

Aberrated Wavefront   Corrected Wavefront

Mirror
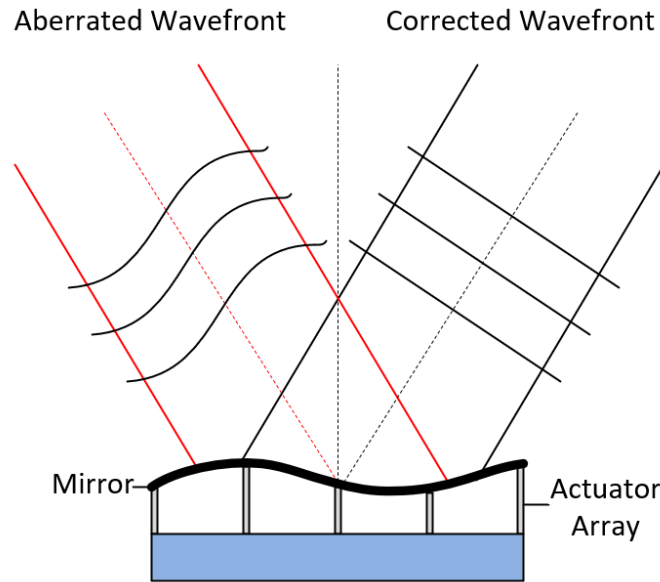
Actuator
Array

Figure 2.8: Illustration of a deformable mirror correcting an aberrated wavefront. An array of actuators behind a mirror membrane enables accurate control over the surface shape.

- Enables high actuator count (scalable)

- Reduced cost

- Limited stroke

The most critical design parameters for a DM is the number of actuators, the distance between adjacent actuators (pitch), the dynamic range of operation (stroke), and the temporal response time of the mirror to a control signal. Actuator stroke, along with the total number of actuators, will determine the degree to which the mirror surface can be deformed. This parameter scales with the aperture size of the telescope. It is important to note that as the number of actuators increases, so does the number of control wires and the size of the driver electronics. The projection of the actuator pitch onto the aperture of the telescope and the response time is designed to meet the requirements set by the atmospheric turbulence length and time scales.

2.4.4   Estimating Performance

There are several different metrics available for estimating the performance of an optical system. The most commonly used in AO is the Strehl ratio (SR). This statistical

quantity is used to quantify the degree of correction an AO system can achieve by measuring the intensity of the central peak in the observed PSF and comparing it with that of a perfectly diffraction-limited system, as shown in figure 2.9. The Strehl ratio is defined as the ratio of the peak intensity to that of a perfect optical system:

$$SR \sim I_S/I_D \tag{2.4}$$

Typical values for an 8-10-meter telescope can range from a few percent or less for ground-based telescopes experiencing poor atmospheric seeing conditions, to greater than 80% in H band (1.6μm) under excellent conditions (Esposito et al., 2011).
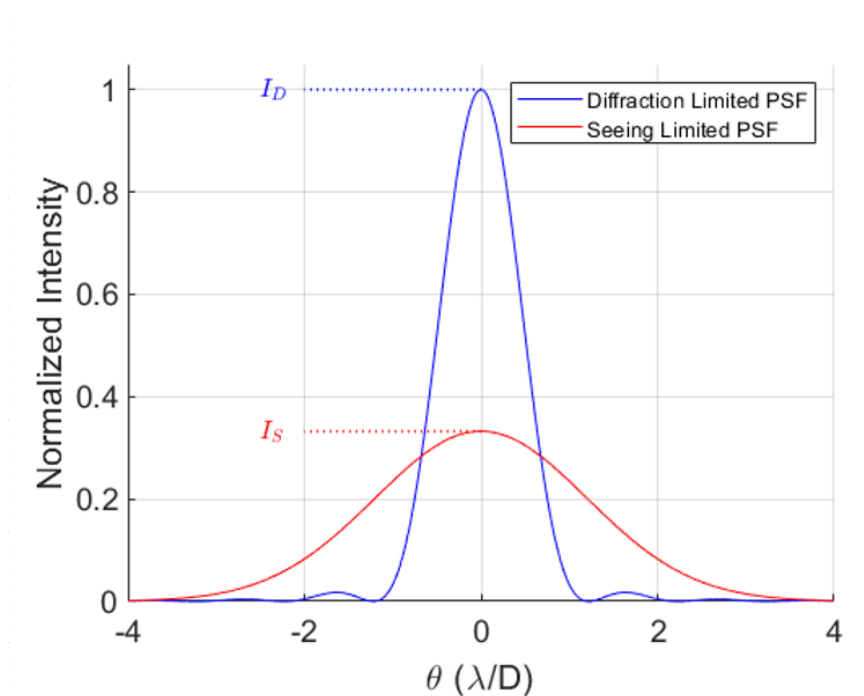
Figure 2.9: The point spread function of a point source for a perfect diffraction-limited telescope in space (blue) and the point spread function for the same telescope when observing through the atmosphere. The Strehl ratio is the ratio between the peak intensity of the observed PSF and the diffraction-limited PSF.

2.4.5   Limitations of Classical Adaptive Optics

The main limitation of classical AO systems that use a single DM is the limited field of view (FoV) over which the correction remains accurate. Section 2.4.1 introduced the concept of using a bright reference source near the science target to characterize

the wavefront aberrations. The issue with both NGS and LGS is that the light from the reference source and the science target travel through different optical paths in the turbulent atmosphere, as shown in figure 2.10. Therefore, the wavefront being measured by the WFS will be slightly different than the one from the science target. The effect of not measuring the same wavefront due to the angular separation between the two objects is referred to as anisoplanatism. As the angle between the guide star and the science target increases, the performance of the AO system decreases. This limits classical AO systems to small off-axis deviations from the science target over which the turbulence does not change significantly. This angle is called the isoplanatic angle. LGSs suffer from an additional problem called focal anisoplanatism or the "cone effect," which results from the laser being focused to a finite altitude in the atmosphere. Unlike a distant point source, the laser produces a conical wavefront instead of a collimated beam, leaving sections of the atmosphere that are not sampled. The benefit of using a LGS is that they can be placed anywhere within the FoV of the telescope, and more than one can be used. Using multiple guide stars leads to the concept of "wide-field AO," which allows for correction over a larger FoV.

2.5 Adaptive Optics Architectures for Extremely Large Telescopes

As we enter the era of extremely large telescopes, AO systems have become a fundamental component in these ground-based observatories. The limited FoV inherent to classical AO implementations is no longer enough to shed light on many of the outstanding questions in astronomy. To extend the useful FoV of an AO system requires a more complex architecture, using multiple WFS's and DM's to probe a larger volume of the turbulent atmosphere.

2.5.1 Introduction to Wide Field Adaptive Optics

Classical AO, also referred to as single conjugate adaptive optics (SCAO), is limited by anisoplanatism since only a single DM that is optically conjugated to the telescope pupil is used. Correcting over a larger FoV requires the system to measure the turbulence at multiple locations in the observed field. More advanced AO architectures use several WFS's and DM's to increase the isoplanatic patch over which high-resolution
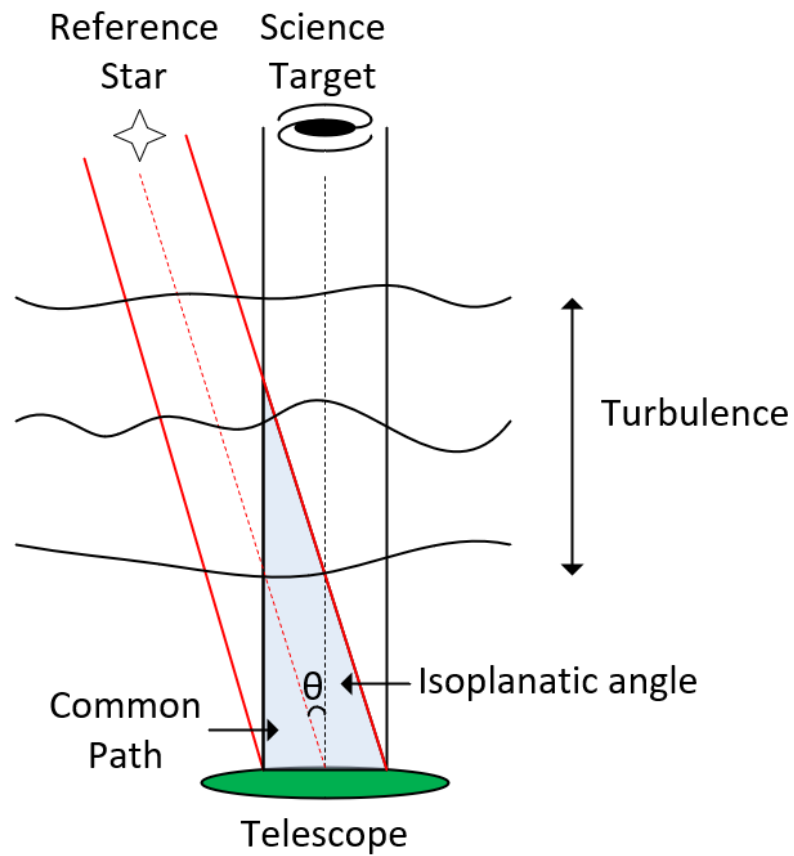
Figure 2.10: Illustration of angular anisoplanatism. The turbulent volume of atmosphere measured by the WFS is not identical to the turbulent volume influencing the science target light.

corrections are possible. Multiple guide stars, not necessarily located in the isoplanatic area of each object, are used to map a turbulent volume of the atmosphere, effectively developing a tomographic probe of the turbulence. The following sections will introduce the main configurations for these types of AO systems.

2.5.2 Multi Conjugate Adaptive Optics

Multi-conjugate adaptive optics (MCAO) observes multiple reference stars (either LGS or NGS) at different locations in the field, using individual WFS's to sample a larger turbulence volume common to all lines of sight. Commands are then supplied to several DM's, each optically conjugated to different altitudes, allowing for the strongest layers of atmospheric turbulence to be corrected. Using multiple WFS's and DM's to reconstruct and correct the turbulence profile over several layers is often referred to as atmospheric tomography. This type of approach is closed-loop, ensuring DM effects are included in the correction, and an average is applied to correct over the full FoV. The most straightforward configuration of MCAO uses a single DM optically conjugated to a layer of the atmosphere close to the observatory ground. Ground layer adaptive optics (GLAO) works on the principle that most of the turbulence is assumed to be generated close to the ground. This type of configuration uses multiple WFS to measure the distortions, and a single DM conjugated at the ground layer to provide correction. GLAO is often used in combination with other architectures to produce a woofer-tweeter configuration.

2.5.3 Multi Object Adaptive Optics

Multi-object adaptive optics (MOAO) adopts an approach similar to MCAO, but instead, the DMs are placed in a parallel configuration to exploit the fact that there are only so many scientifically interesting objects located in the FoV. In this type of arrangement, light from the individual science targets is coupled to a deployable probe that patrols the telescopes FoV, and corrects for aberrations using a dedicated DM. The result is that multiple corrections can be applied simultaneously by decomposing the large telescopes FoV into separate narrow fields. This type of approach lends itself nicely to applications that do not require the full FoV to be corrected, such

---

[2]https://www.eso.org/sci/facilities/develop/ao/ao_modes/.html.
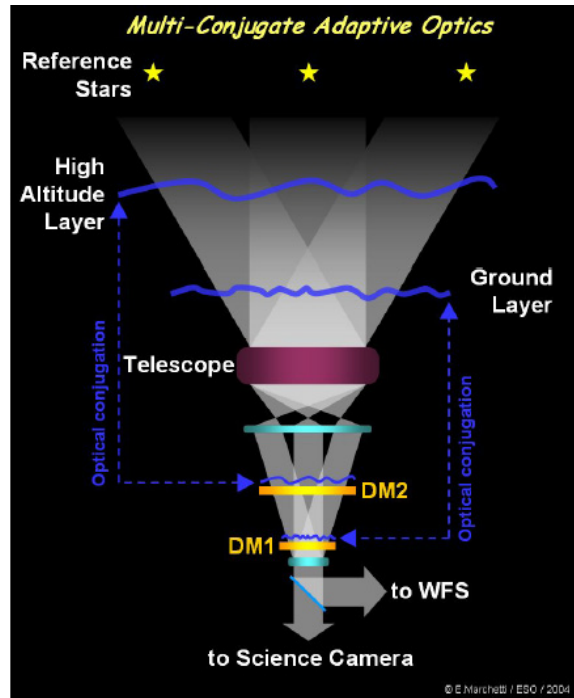
Figure 2.11: Illustration of MCAO principles. Multiple reference stars are observed in the telescope's field of view, using individual WFS's to sample a larger turbulence volume. Image courtesy of ESO.[2]

as multi-object spectroscopy (MOS), where only a small sub-region is desired. The caveat, when doing MOAO, is that the system must be run in an open-loop (i.e., the WFSs are no longer in the optical path of the DM). This means that the WFS's see the uncorrected wavefront that has been subject to the full effect of the atmospheric turbulence.

2.5.4 Implications of Open-Loop Operation

When an AO system is operated in an open-loop configuration, the WFS measures the turbulent wavefront before the DM has applied any corrections. This type of approach is necessary for MOAO since the DM and WFS are optically separate. In classical closed-loop operation, the WFS can measure the effect of the DM, which means residual errors will be fed back into the system and subsequently corrected. Since this is not possible in open-loop control systems, the DM performance must be predictable and repeatable since errors will register as distortions in the wavefront. Unlike closed-loop approaches where the shape of the DM is directly controlled by the WFS data,
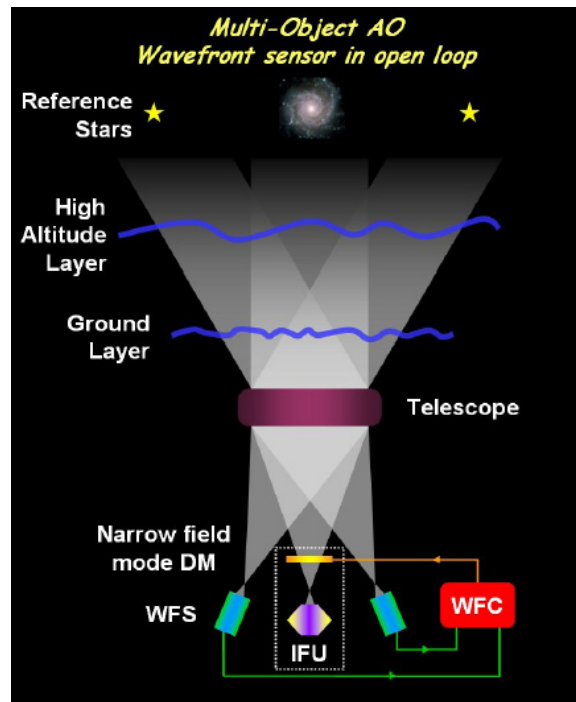
Figure 2.12: Illustration of MOAO principles. Multiple smaller areas are corrected for instead of correcting the entire field of view. Image courtesy of ESO.

a process called tomographic reconstruction is required. Tomography in AO refers to the use of a mathematical formulation to estimate (or reconstruct) the turbulent volume through which light from a science object travels based on measurements from guide stars located in different positions throughout the telescopes FoV. Calibrating these systems becomes increasingly challenging since the connection between the DM and WFS is not directly evident. In closed-loop systems, it is common to poke individual actuators in the DM and look at the change in wavefront as measured by the WFS. This process leads to an "interaction matrix" and allows for optical defects that have originated from the AO system itself to be compensated. Other challenges include larger non-common path errors (i.e., different optical paths taken by light), and a WFS with a higher dynamical range.

2.5.5 Deformable Mirror Requirements: How does the number of actuators scale with telescope diameter?

Correcting for the effect of atmospheric turbulence on the wavefront phase requires us to adopt a mathematical basis for modelling the phase surface over the telescope
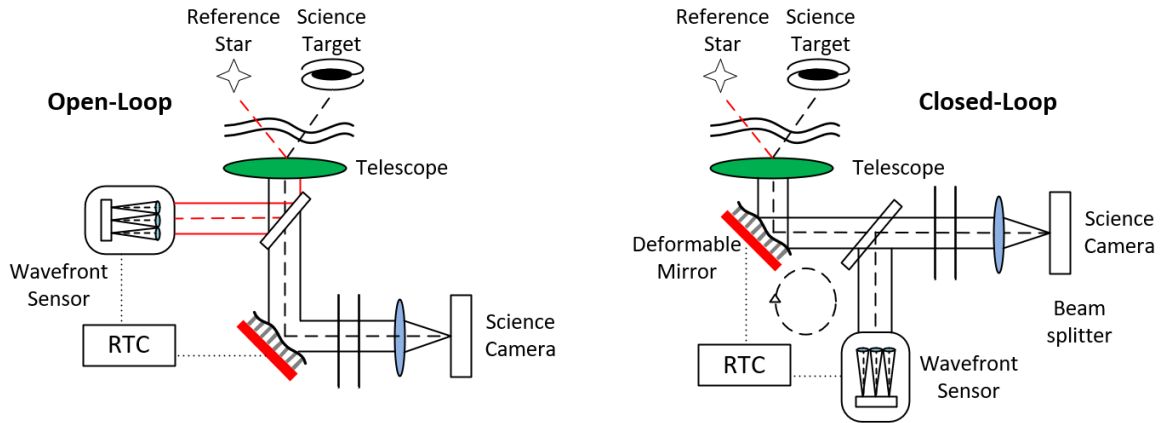
Figure 2.13: Illustration of closed-loop and open-loop operation in AO. Left: Open-loop system. The optical path of the WFS (red) is independent of the DM (black). Right: Closed-loop system with respect to the WFS and DM (dashed line).

aperture. Similar to the way Fourier series are used in waveform analysis, Zernike polynomials are used in optical systems to decompose the complex shape into individual components. Since most optical systems, including telescopes, have a circular pupil, it is useful to adopt a mathematical description of aberrations that uses a complete set of basis functions that are orthogonal over the unit circle. Zernike polynomials are convenient since the low-order terms represent common types of aberrations observed in optical systems (e.g., coma, astigmatism, and spherical aberration). These polynomials were first introduced by Frits Zernike in 1934 to describe common optical aberrations and later tailored by Fried to describe the statistical strength of aberrations introduced in a wavefront by atmospheric turbulence (Fried, 1965). It was not until 1976 that Noll extended Fried's work to develop a modified set of Zernike polynomials to represent the Kolmogoroff spectrum of turbulence commonly adopted in AO theory today. Specifically, Noll introduced a normalization term that provided a convenient basis for statistical analysis of the atmospheric turbulence (Noll, 1976).

The modified set of Zernike polynomials described by Noll are orthogonal over the unit circle and are defined in polar coordinates with radial distance ρ and azimuthal angle θ as:

$$Z_n^m(\rho, \theta) = N_n^m R_n^m(\rho) A^m(\theta) \qquad (2.5)$$

From this, we can see that the polynomials are given by the product of radial polynomials $(R_n^m(\rho))$ and angular functions $(A^m(\theta))$, normalized by a factor N_n^m.

The radial polynomials are defined as:

$$R_n^m(r) = \sum_{s=0}^{\frac{n-m}{2}} \frac{(-1)^s(n-s)!}{s!(\frac{n+m}{2}-s)!(\frac{n-m}{2}-s)!} r^{n-2s} \qquad (2.6)$$

The angular functions are defined as:

$$A^m(\theta) = \left\{ \begin{array}{ll} \cos(m\theta) & \text{for } m \geq 0 \\ \sin(m\theta) & \text{for } m < 0 \end{array} \right\}$$

And the normalization term, which ensures the RMS value of each polynomial over the circle has a value of 1, is defined by Noll as:

$$N_n^m = \sqrt{\frac{2(n+1)}{1+\delta_{m,0}}} \qquad (2.7)$$

where $\delta_{m,0} = 1$ for $m = 0$ and $\delta_{m,0} = 0$ for $m \neq 0$

Combining these terms, we arrive at the even and odd polynomials used to describe the impact of aberrations caused by atmospheric turbulence:

$$Z_{i,even} = \sqrt{n+1} R_n^m(r)\sqrt{2}\cos(m\theta) \qquad \text{for } m \neq 0 \qquad (2.8)$$
$$Z_{i,odd} = \sqrt{n+1} R_n^m(r)\sqrt{2}\sin(m\theta) \qquad \text{for } m \neq 0 \qquad (2.9)$$
$$Z_i = \sqrt{n+1} R_n^0(r)\sqrt{2} \qquad \text{for } m = 0 \qquad (2.10)$$

In this set of equations, the indices n and m are the radial degree and the azimuthal frequency, respectively, and i is a mode ordering number. The values of n

and m are always integers and satisfy $m \leq n$, $n - m$ must be even Noll (1976). The relationship amongst these indices for the first nine polynomials and their corresponding aberration are listed in Table 1.

n	m=0	m=1	m=2	m=3
0	$Z_1 = 1$ (Piston)			
1		$Z_2 = 2r\cos{(\theta)}$ $Z_3 = 2r\sin{(\theta)}$ (Tip and Tilt)		
2	$Z_4 = \sqrt{3}(2r^2 - 1)$ (Focus)		$Z_5 = \sqrt{6}r^2\sin{(2\theta)}$ $Z_6 = \sqrt{6}r^2\cos{(2\theta)}$ (Astigmatism)	
3		$Z_7 = \sqrt{8}(3r^2 - 2r)\sin{(\theta)}$ $Z_8 = \sqrt{8}(3r^2 - 2r)\cos{(\theta)}$ (Coma)		$Z_9 = \sqrt{8}r^3\sin{(3\theta)}$ $Z_{10} = \sqrt{8}r^3\cos{(3\theta)}$ (Trifoil)

Table 2.1: Zernike Polynomials. The modes, Z_1, are ordered such that even i corresponds to the symmetric modes defined by $\cos(m\theta)$, while odd i corresponds to the antisymmetric modes given by $\sin(m\theta)$ (Noll, 1976).

From figure 2.14, we can see that the lower order modes have the largest impact on wavefront aberration, containing most of the turbulent energy. As the order of the mode increases, the total power contributed from that mode decreases.
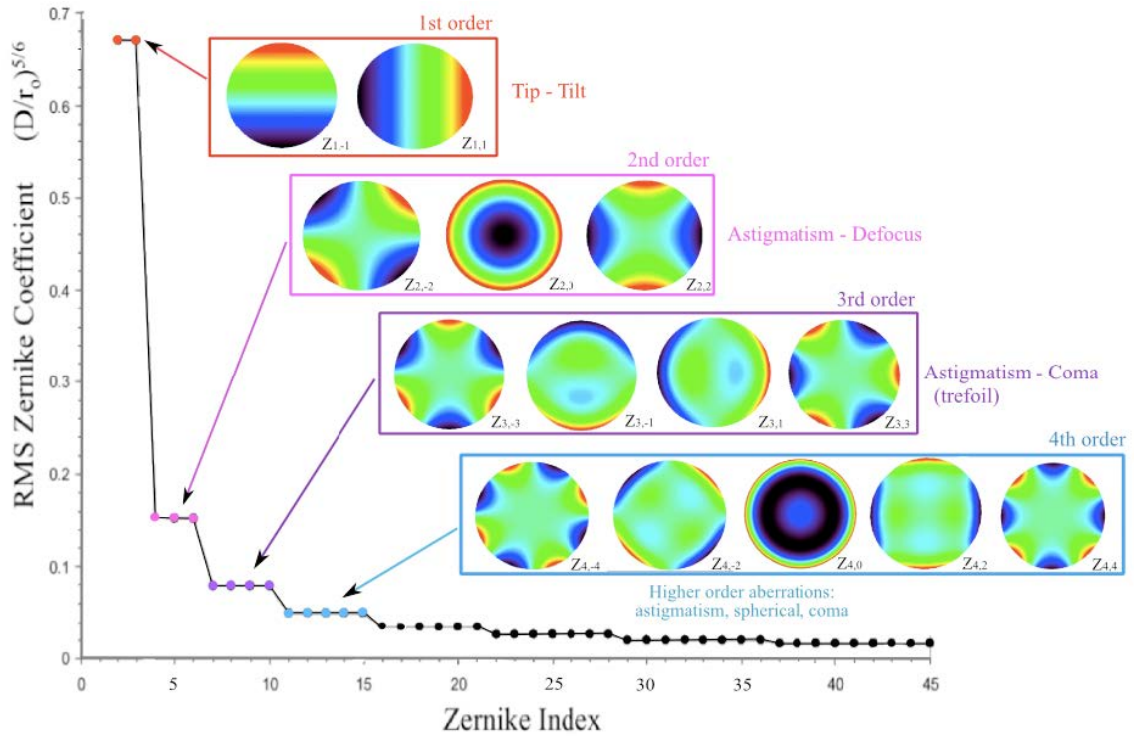
Figure 2.14: Representation of the wavefront shape for the first four orders Zernike polynomials and a plot of the RMS Zernike coefficient (the strength for atmospheric turbulence following Kolmogorov statistics) of the first 45 Zernikes. Image courtesy of Blain (2012).

The wavefront error (i.e., the deviation from a flat wavefront) measured by the WFS can be expressed using a weighted sum of the Zernike polynomials:

$$\phi_{turb}(r,\theta) = \sum_{i=1}^{\infty} a_i Z_i(r,\theta) \tag{2.11}$$

where a_i are the expansion coefficients of the Zernike polynomials.

From the wavefront error, a set of commands can be determined to reproduce the shape needed to minimize or 'null' the surface of the wavefront. A common approach is to measure the residual error in the wavefront after correction to assess how well the AO system is performing. By removing an increasing number of Zernike modes from the disturbed wavefront using a DM, it is possible to reduce the residual error. However, this becomes increasingly challenging since the finite spacing of active actuators in the telescope pupil places an upper limit on the degrees of freedom

with which the DM surface shape can be controlled. Since the DM cannot precisely replicate the shape of the turbulence, a spatial fitting error arises.

Let us consider the aberration resulting from the first J Zernike polynomials:

$$\phi_J(r, \theta) = \sum_{i=1}^{J} a_i Z_i(r, \theta) \tag{2.12}$$

After correcting for these aberrations, the mean square (i.e., variance) of the remaining aberrations can be expressed as:

$$\sigma_{fitting}^2 \approx 0.2944 N_{Zern}^{-\sqrt{3}/2} (D/r_0)^{5/3} \quad [\text{rad}]^2 \tag{2.13}$$

where N_{Zern} is the number of completely corrected Zernike modes, D is the aperture diameter, and r_0 is the Fried parameter.

This relationship, initially proposed by Noll for $N_{Zern} > 10$, represents the fitting error if our DM was able to produce the Zernike modes perfectly.

It is more common to relate the fitting error to a DM parameter that can be controlled during this design phase (i.e., the actuator pitch or inter-actuator spacing):

$$\sigma_{fitting}^2 = \kappa \left(\frac{d}{r_0} \right)^{\frac{5}{3}} \tag{2.14}$$

where the fitting coefficient κ depends on the DM influence function and actuator geometry. This value is approximately 0.3 for continuous phase sheet DMs (Madec, 2012).

From equation 2.14 we see that the variance of the wavefront fitting error decreases as the 5/3rd power of the actuator spacing.

If the total number of active actuators in the telescope pupil is given by:

$$N_{Act} = \left(\frac{D}{d} \right)^2 \tag{2.15}$$

equation 2.14 can be written as:

$$\sigma^2_{fitting} = \kappa \left(\frac{D}{r_0} \right)^{\frac{5}{3}} N_{Act}^{-\frac{5}{6}}$$

(2.16)

Note that the power term for N_{Act} (i.e. -5/6) varies slightly from the $\sqrt{3}/2$ in the ideal case.

Solving for N_{act} gives:

$$N_{act} = \left[\kappa \left(\frac{D}{r_0} \right)^{\frac{5}{3}} \left(\frac{1}{\sigma^2_{fitting}} \right) \right]^{\frac{6}{5}}$$

(2.17)

From this, we find the number of actuators can be approximated as:

$$N_{act} \sim \left(\frac{D}{r_0} \right)^2$$

(2.18)
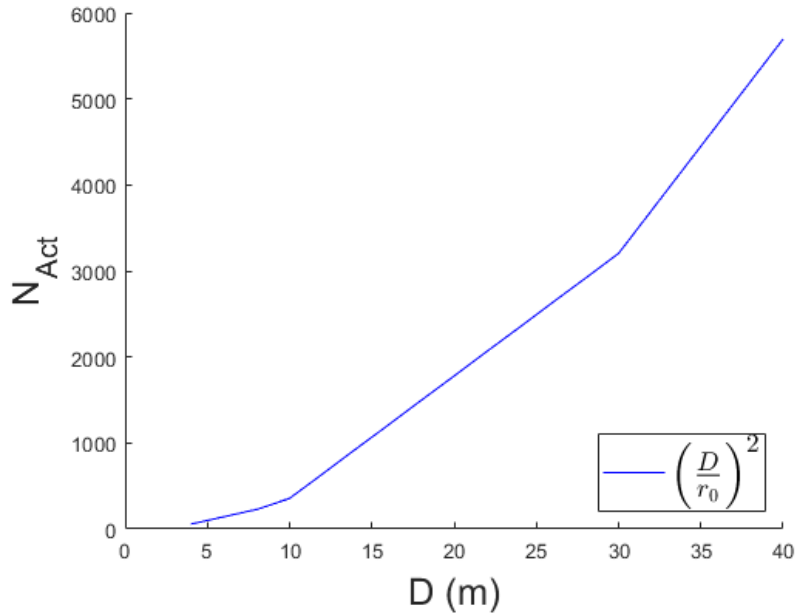
Figure 2.15: Approximate scaling of the useful number of DM actuators in the telescope aperture with the primary mirror diameter.

From figure 2.15, it is evident that for a simple SCAO system on an 8-meter class telescope, there are approximately 230 useful actuators in the telescope pupil. This corresponds to a 16×16 actuator DM. As we move to a 30-meter class telescope,

there will be 3200 useful actuators in the telescope pupil, corresponding to a 60×60 actuator DM. Implementing a high actuator count is challenging since each actuator requires a set of control wires. Adopting a highly compatible and scalable solution, like MEMS/IC technology, will be critical for ELTs and space-based systems.

Chapter 3

ASIC Driver Development

3.1 Introduction

In this chapter, I demonstrate the feasibility of an integrated driver electronics solution for low-voltage and low-current MEMS DM technology that will be suitable for high-order wavefront correction. The system, shown in figure 3.1, comprises a Lorentz force MEMS actuator array coupled to a polymer mirror membrane, and a dedicated driver IC suitable for driving the MEMS elements in a "push-pull" mode. The system provides astronomers with the ability to achieve the level of wavefront correction necessary to take advantage of the resolution and sensitivity gains offered by large diameter ground-based telescopes.

A Lorentz MEMS actuator array is chosen as a transducer driving mirror since it offers many advantages over conventional technologies, including bi-directional motion, low voltage operation without magnetic hysteresis and compact size (Park et al., 2018, 2017). Bi-directional motion provides out-of-plane push and pulling motion that affords the ability to manipulate mirror surface morphology as well as the correction of surface flatness. It also satisfies the latest industry trends, such as low power consumption and minimal spacial occupancy. These benefits, along with fast response and reasonable power consumption, make them ideal for large stroke applications such as Earth-based telescopy, free-space optical communication, and optical microscopy.

While the system operates at significantly lower voltages than existing DM technologies, it still requires a high-voltage (HV) CMOS process foundry to meet the MEMS driving requirements. To achieve the desired deformation of the mirror surface, the driver is required to produce a bipolar $\pm$ 15 V square wave. The IC was shown to provide $\pm$ 20 μm of stroke using a $\pm$ 5 mA current in a 0.1 T magnetic field. The IC implementation and preliminary experimental measurements from a chip that was designed and fabricated in Austriamicrosystems (AMS) 0.35 μm CMOS HV process technology are discussed in the following sections. The authors also explore chip
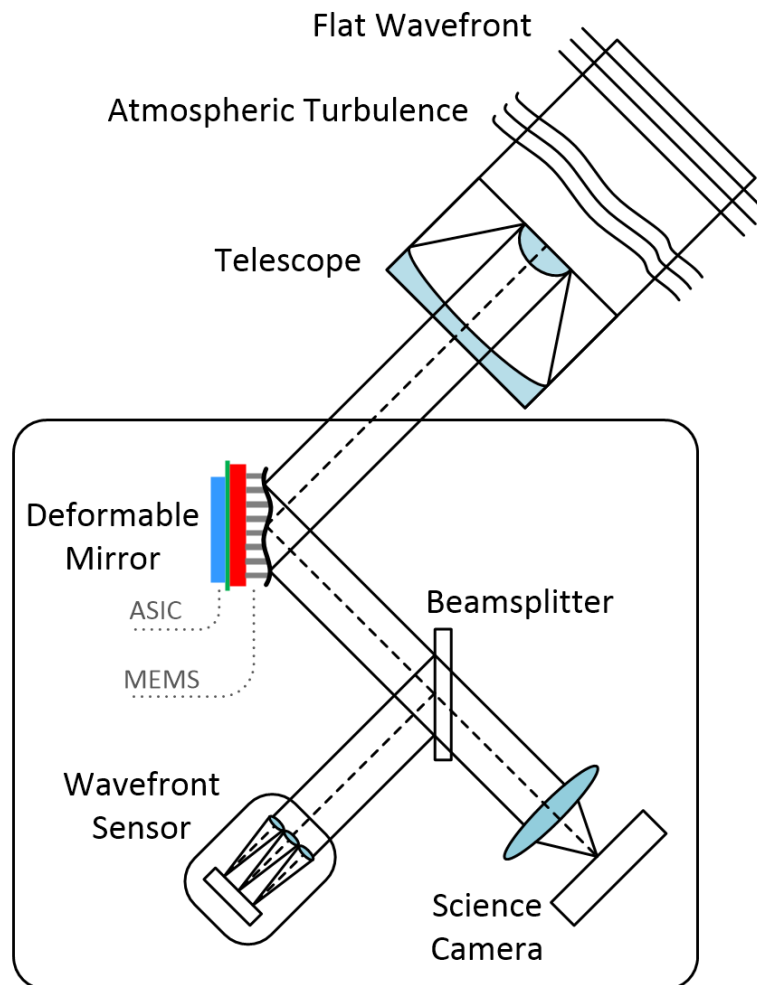
Figure 3.1: Conceptual drawing of a conventional adaptive optics system. Incoming light is distorted by turbulence in Earths atmosphere before entering the focal plane of the telescope. A wavefront sensor is used to sample the incoming wavefront and determine a set of commands to a send to the deformable mirror. The shape of the deformable mirror is subsequently adjusted to that of the wavefront to compensate for distortions.

level integration between the DM and ASIC.

3.2 Overview of Low-Voltage MEMS Deformable Mirror System

Figure 3.2 shows the block diagram of the proposed device. It consists of a mixed-signal CMOS driver module and an array of 25 Lorentz force MEMS actuators. Each of the actuator electrodes is driven between - 15V and + 15V to deflect the mirror

in the vicinity of the actuator. The combined effect of all actuators is to impose a well-defined, repeatable contour shape on the mirror surface.

The driver chip contains individual drivers for each actuator, and is designed to interpret information from the WFS through a serial peripheral interface (SPI) and encode the signal into pulses using a pulse-width modulation (PWM) technique. Each actuator is charged or discharged by the driver with the equivalent of an 8-bit digital control signal. All of the digital logic operations for the modulation are performed in the low-voltage domain before being converted to a high-voltage analog signal at the output.
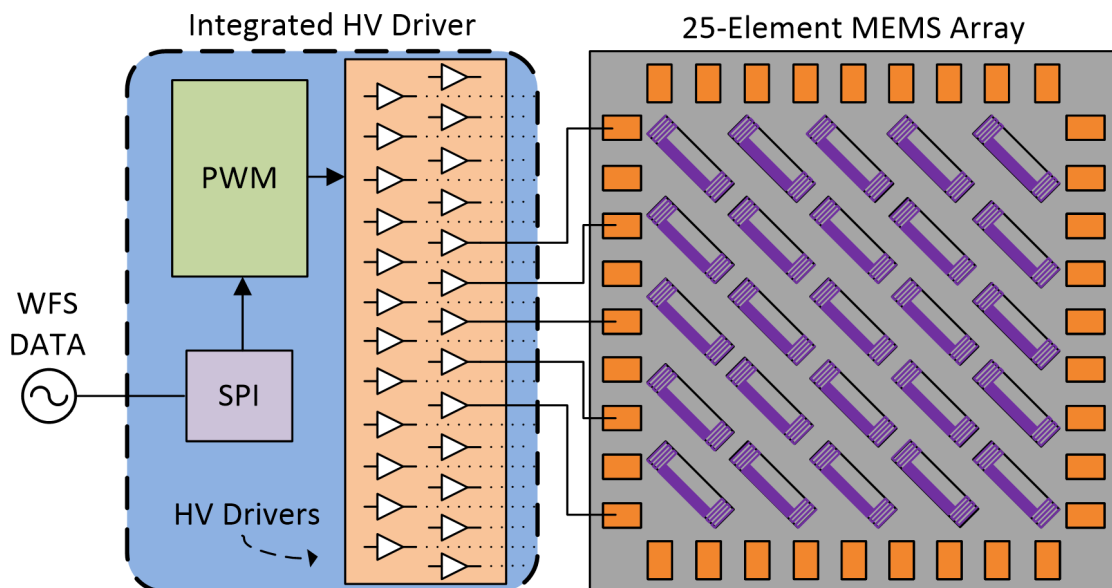
Figure 3.2: Block diagram of the proposed MEMS deformable mirror system. All functional blocks of a complete array driver, which include the PWM modulation, SPI digital interface, and high-voltage drivers are combined on a single chip.

3.3 Integrated High-Voltage Driver

The basic architecture of the driver is that of an open-loop class-D power amplifier commonly used in audio applications (e.g.Bloechl, Bataineh & Harrell 2004; Guanziroli, Bassoli, Crippa, Devecchi & Nicollini 2012; Lin, Wu, Zhao & Zhao 2012; Lam, Tan, Cox & Yeo 2012), as shown in figure 3.3. The input signal is converted to a high frequency switching signal using a PWM technique common in modern digital

signal processing (DSP) applications.

The PWM signal is used to perform digital to analog conversion by producing duty cycle variations that linearly track the amplitude of the input signal. Low pass filtering the driver output to remove the high frequency components yields dc values that are proportional to the duty cycle of the PWM.

The signal can be treated as the summation of a dc component and a zero-average square wave. Analysis of a symmetric PWM square wave can be performed using the standard Fourier series representation of an even periodic function, given by the relationship written in Eq. 3.1.

$$f(t) = A_0 + \sum_{n=1}^{\infty} \left[A_n \cos \frac{2n\pi t}{T} + B_n \sin \frac{2n\pi t}{T} \right] \tag{3.1}$$

where A_0 represents the dc component, T is the period of the square wave, and A_n and B_n are the Fourier coefficients. The value of this dc component can be found by taking the integral of the square wave over the period in Eq. 3.2.

$$A_0 = \frac{1}{2T} \int_{-T}^{T} f(t) dt \tag{3.2}$$

Performing this integral yields the relationship in Eq. 3.3, where the dc component (A_0) is directly proportional to the signal f(t) amplitude (K) and duty cycle (D) of the PWM signal.

$$A_0 = K \times D \tag{3.3}$$

From this equation we can see that by tuning the duty cycle to achieve different dc levels, we can control the signal driving the MEMS. The implementation adopted in this paper uses an offset such that 50% duty cycle corresponds to an output of 0 V.

The modulated signal is used to control the ON/OFF status of the power transistors that supply current to the low-pass filter and load. This type of architecture is desirable for stable and highly efficient low-power operation. Applying pulses ensures the power transistors are operating in either the linear or cut-off regions, and power loss only occurs when the transistor is changing states.
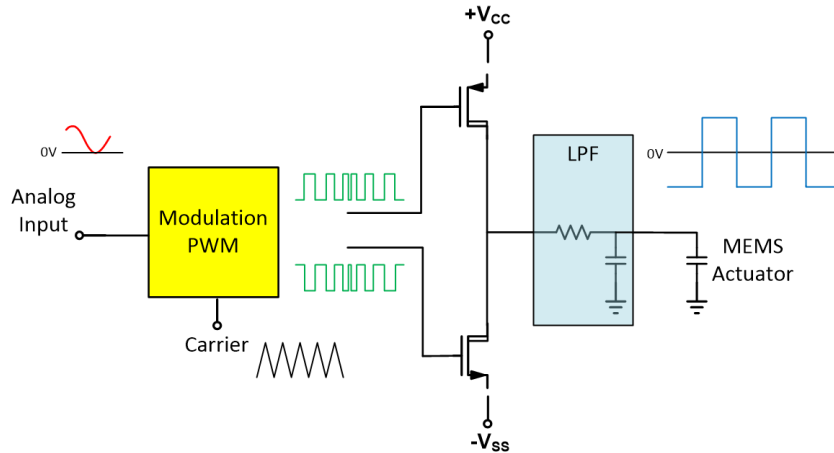
Figure 3.3: Open-loop class-D amplifier system design.

The schematic of the proposed HV driver circuit is shown in figure 3.4. Several design avenues were explored before converging on this architecture. In the straightforward analog design case, the MEMS actuators would be driven by a continuously varying time signal dictated by the correction sensed by a WFS, and implemented as a series of operational amplifiers functioning in a feed-back configuration. This approach requires the use of many HV transistors, which raises the issue that each of the transistors will require protection from the potential of a HV being applied across the gate. HV components suffer from large area requirements and the need to design appropriate HV digital-to-analog converters (DACs). Although this type of design is possible, similar results can be achieved using a mixed signal approach that is becoming increasingly popular in integrated circuit design. Instead of using a fully analog system, we propose to combine the desirable properties of a continuous-time (analog) circuit with those of a switching mode (digital) design. This type of design approach, coupled with the use of a CMOS fabrication process, enable the driver to scale with the large number of actuators being demanded by next generation astronomy applications.

This type of approach reduces power consumption by directly applying the DSP signal to the driver without the need for a HV DAC and HV power amplifier, both of which may have high static power consumption. In addition, it provides a system architecture with efficient programmability. Instead of having to replace analog blocks to meet a new set of requirements, the driver can be reconfigured in the DSP blocks.
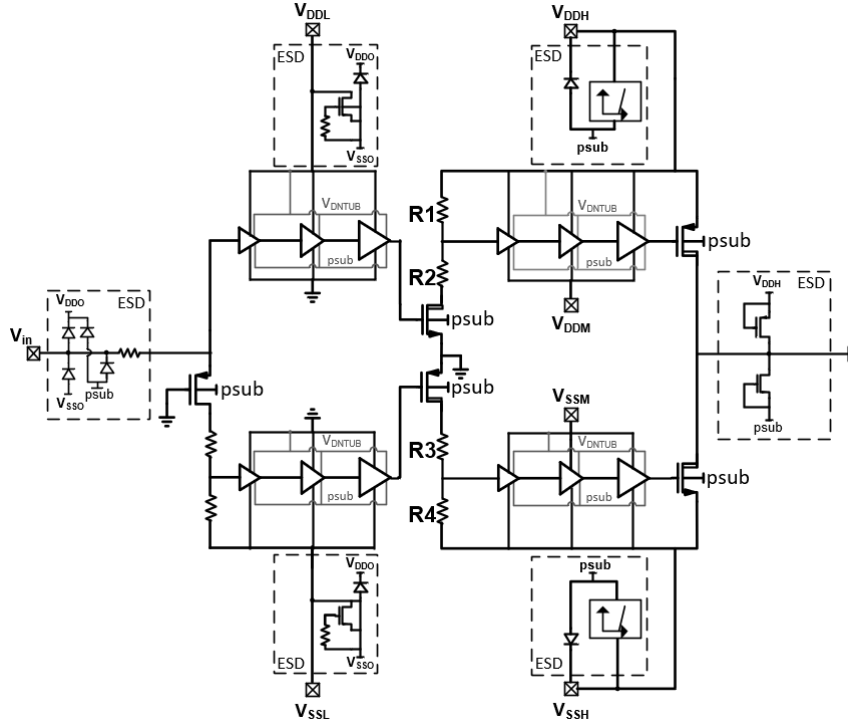
Figure 3.4: Circuit schematic of the proposed High-Voltage IC driver. A low-voltage PWM signal is passed through a series of increasing size buffers to drive the HV output transistors and produce a bipolar output signal. I/O and power supply ESD protection cells are also included.

The output stage of the proposed circuit uses a similar architecture as the output driving stage of an open-loop class-D audio power amplifier. While it is common to implement closed-loop feedback in audio amplifier applications, the first generation of the HV driver uses the global feedback in the AO system to enable sufficient resolution. A complementary pair of HV transistors with their drains connected at the output are fed by series-connected inverters that buffer the p-type metal-oxide semiconductor (PMOS) and n-type metal-oxide semiconductor (NMOS) control signals to maximize the load driving capability. The fact that the chip is being supplied with positive and negative as well as high and low voltages presents a challenge when considering device layout. When implementing this type of multi-level bipolar voltage supply design, it is crucial to isolate sensitive components and/or regions of the IC and select the appropriate biasing. Incorrect biasing can result in internal junctions being turned on and circuit failure. In this design, the core drivers are surrounded by an I/O ring that forms the required electrostatic discharge (ESD) structures (i.e. ESD-rails)

and power supply buses. The ESD-rails and the power supply for the periphery-ring, V_{DDO} and V_{SSO} (shown in figure 3.4) are connected to +3 V and -3 V, respectively. At the core of the circuit, individual components are isolated by placing them in a deep n-well (DNTUB). The appropriate bias is then chosen based on the type and operational region of the component. For NMOS devices, the DNTUB is inherently tied to the drain of the transistor and for PMOS deivces, DNTUB is tied to the bulk of the transistor. In all cases, the substrate (psub) is connected to the global minimum (i.e. -15 V).
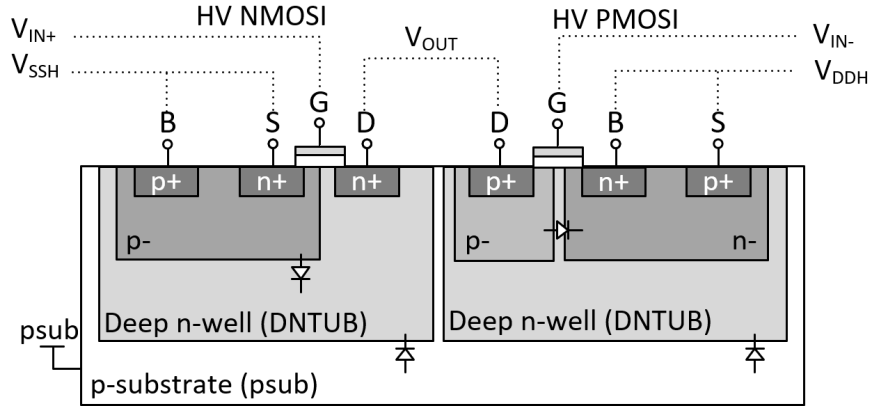
Figure 3.5: Cross section of isolated HV output transistors with connections.

Figure 3.6 shows a cross section of the inverter common to both the LV and HV regions of the chip. If we consider the inverters in the upper branch of the HV region (i.e. those driving the HV PMOS transistor at the output), the DNTUB would be tied to $V_{DD} = +15$ V and V_{SS} would be placed at +11.7 V to keep the peak-to-peak of $V_{IN} < 3.3$ V.

Careful consideration is placed on the level-shifter implementation to limit the voltage at the transistor gates to be within the specified gate-to-source voltage of the process technology (i.e. 5 V). In this circuit, a resistive voltage divider based topology is used to maintain $V_{GS} = 3.3$ V and to keep pulse values independent of temperature and process variations. Both the upper and lower driver branches use polysilicon resistors coupled with NMOS and PMOS transistor, respectively. The resistor values are chosen to be sufficiently large as to minimize the dissipated power and to ensure that the drain-to-source on-state resistance R_{ON} of the HV transistors is negligible, therefore making the voltage divider ratio driving the gate independent of process
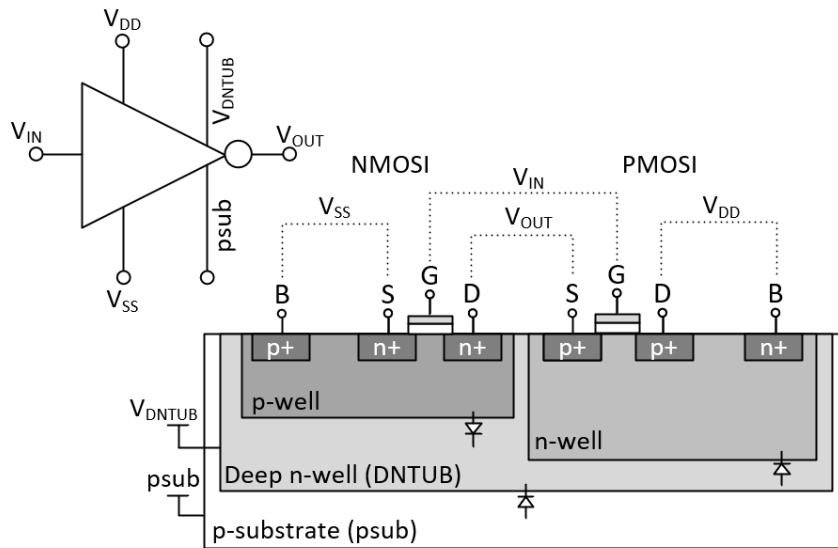
Figure 3.6: Cross section of isolated inverter implementation. The inverter symbol and connections are shown in the upper left.

variations. The ratio is defined to produce pulses between 11.7V to 15V in the upper branch, and -11.7 and -15V in the lower branch.

To ensure the large valued resistors are well-matched for the voltage divider, a serpentine layout with individual resistor finger connected in series is used. Dummy fingers are also included at the ends of the active resistor elements to match boundary conditions.

3.4 Fabrication

Chip fabrication was facilitated through CMC Microsystems, a corporation tasked with submitting designs to global leaders in IC design and manufacturing on behalf of academic institutions at a reduced rate. The IC design presented in this thesis was submitted through CMC's multi-project wafer service using Austrian Microsystems 0.35um high-voltage process technology. Three different design iterations were explored. While the core design of the driver remained the same, the IO cells and ESD protection approach were changed to overcome different challenges. CMC was also responsible for device packaging and wirebonding for each design.

3.4.1 Design and Fabrication Foundry

Several different foundries and processes were identified as being capable of meeting the required specifications for the developing the HV driver. When choosing an appropriate process technology, it was critical to find one that could maintain a high gate-to-source voltage.

Austriamicrosystems (ams)[1]**:** The 0.35μm CMOS technology has become an industry standard for high-voltage, analog and mixed-sginal design. The technology offers four metal layers (including one thick layer) for signal and supply routing, two resistive poly layers, 3.3V/5V digital standard cells, and ESD protected IO cells. The ams "H35" process used in the driver design can operate up to 120 V, with a maximum of 20 V at the transistor gate. A library of high-voltage transistors with isolation well enables these devices to be combined into the same chip with standard, low-voltage devices.

Taiwan Semiconductor Manufacturing Company (TSMC)[2]**:** The 0.18μm HV technololgy is based on the 1.8V/5V MS technology and adds 5V, 6V, 7V, 8V, 12V, 16V, 20V, 24V, 29V, 36V, 45V, 55V, 65V and 70V devices, aiming for high-voltage power management and automotive applications.

XFAB[3]**:** The XH018 series is X-FAB's 0.35 micron Modular Mixed Signal HV CMOS Technology. The technology offers up to 4 metal layers, standard cell 3.3V/5V core modules, HV NMOS/PMOS modules, and ESD modules. Transistors can withstand operating voltages up to 100V.

Table 3.1 summarizes the key features of the different foundries.

---

[1]https://ams.com/process-technology
[2]https://www.tsmc.com/english/default.htm
[3]https://www.xfab.com/home/

Company	Name	Features	Poly Metal	Metal Layers	Core Modules	HV Modules
ams	0.35μm CMOS HV	Mixed signal design, standard cell, isolated modules, IO, bondpad	2	4	5V/3.3V	120V/50V
TSMC	0.18μm CMOS BCD	Mixed signal design, standard cells	1	6	5V/1.8V	100V
XFAB	0.18μm XH018	Mixed signal design, standard cells	1	6	5V/3.3V	6V-45V
XFAB	0.35μm XH035	Mixed signal design, standard cells	2	4	5V/3.3V	12V-100V

Table 3.1: Comparison of different HV CMOS process technologies.

Based on access to shared fabrication runs and subsidized pricing through CMC, development was done using the ams 0.35μm CMOS HV process.

Fabrication began with a single channel device in February 2017 (shown in figure 3.7) and ended with a 9-channel design in October 2018. An optical image of the multichannel HV driver prototype is shown in figure 3.8 with an active area of 1.85$\times$1.8 mm^2 (including the I/O pads). Dies were housed in a 44-pin Ceramic Quad Flat Pack (CQFP) package and the output pads were wired to the pads on the CQFP package, as shown in the bottom right of Fig. 3.8.
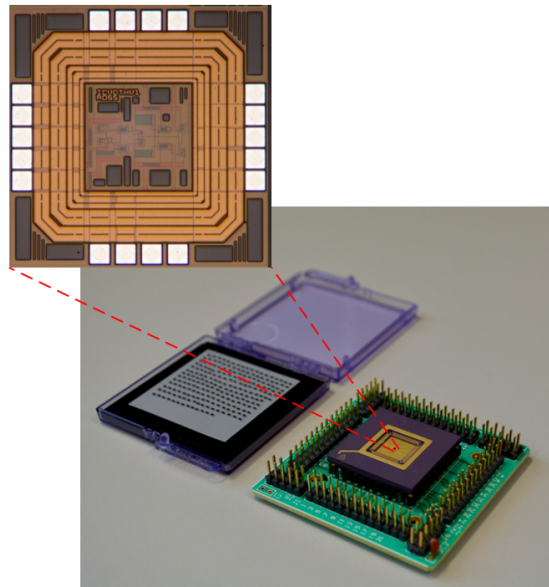
Figure 3.7: Bare die packaged in a PGA84 socket provided by CMC Microsystems. Top left: A 10x optical image of the bare die.
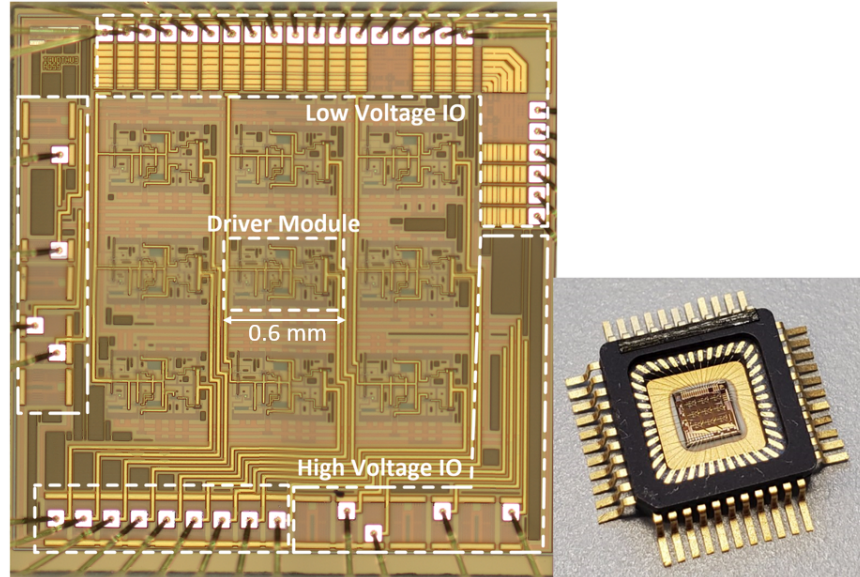
Figure 3.8: Optical microscope image of the manufactured driver IC die. A total of nine channels and the I/O cells are shown. Driver die in a 44-pin Ceramic Quad Flat Pack (CQFP) package

3.5 A Lorentz Force Actuated Continuous Deformable Polymer Mirror

The integrated HV driver is electrically coupled to the 5×5 MEMS actuator array to evaluate the driving performance of the IC. The MEMS DM is powered by the Lorentz force and was demonstrated in the Nano-Systems Fabrication Laboratory (NSFL) at the University of Manitoba by Park et al. (2017, 2018). The Lorentz MEMS actuator offers many advantages, including bi-directional motion, low voltage operation without magnetic hysteresis and compact size (Park et al., 2018, 2017). Bi-directional motion provides out-of-plane push and pull motion that affords the ability to manipulate mirror surface morphology as well as the correction of surface flatness. It also satisfies the latest industry trends, such as low power consumption and device compactness. These benefits, along with fast response and reasonable power consumption, make them ideal for large stroke applications such as Earth-based telescopy, free-space optical communication, and optical microscopy.

The actuator design and working principle of the actuator are shown in figure 3.9. Each actuator consists of a central pillar and a rigid crossbar supported by flexible serpentine springs on both sides. The crossbar is made of 2080 μm (L) × 200 μm (W)

$\times$ 26 μm (H) crystalline silicon. The high mechanical rigidity is intended to prevent the crossbar from bending by opposing force when the actuator deforms the mirror. The flexible 5 μm thick serpentine springs provide a pathway for electrical current and heat sinking to the substrate as well as a mechanical support for the crossbar. A 1.5 μm layer of aluminum sputtered on both the crossbar and serpentine spring is used as the current-carrying wire. The 300 μm thick rails dissipate heat and provide space for an electrical wire connected to an external circuit.

The Lorentz force ($\vec{F}$) in the z-axis acting on the crossbar is calculated by the cross product of a current flow ($\vec{i}$) normal to the magnetic field ($\vec{B}$). The force relationship is governed by Eq. 3.4:

$$\vec{F} = \vec{il} \times \vec{B} \tag{3.4}$$

where l is the length of conducting wire on the crossbar.
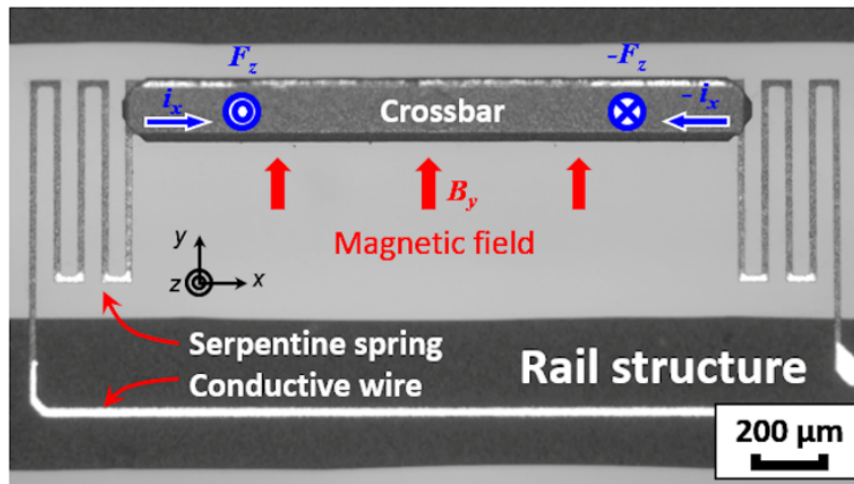
Figure 3.9: Microscope image of the fabricated Lorentz actuator and the working principle for operation. Courtesy of Park (2018).

Figure 3.10 shows the fabricated MEMS device presented in Park et al. (2017, 2018). The left image shows a fabricated 5×5 actuator array. Each actuator is connected to the outer contact pad through aluminum wires. The right image shows the Lorentz DM system after combining the mirror phase sheet and actuator substrate. The continuous polymer mirror consists of a thin SU-8 photoresist membrane (4 μm thickness) covered with 250 μm thick aluminum on both sides.
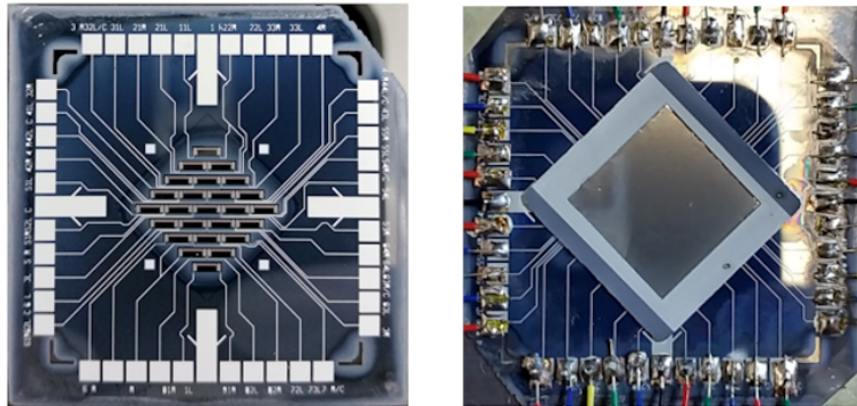
Figure 3.10: (Left) Photograph of the fabricated 5×5 Lorentz MEMS actuator array. (Right) Photograph of electrically wired and mirror coupled DM. Courtesy of Park (2018).

3.6 Device Testing Results

A custom test PCB was designed to accommodate the packaged driver and supply all of the necessary peripherals. To minimize the use of external power supplies and waveform generators, required voltages and clocks are generated on the board. The design also uses SMA connectors to optimize the connection with external equipment (e.g. oscilloscope).
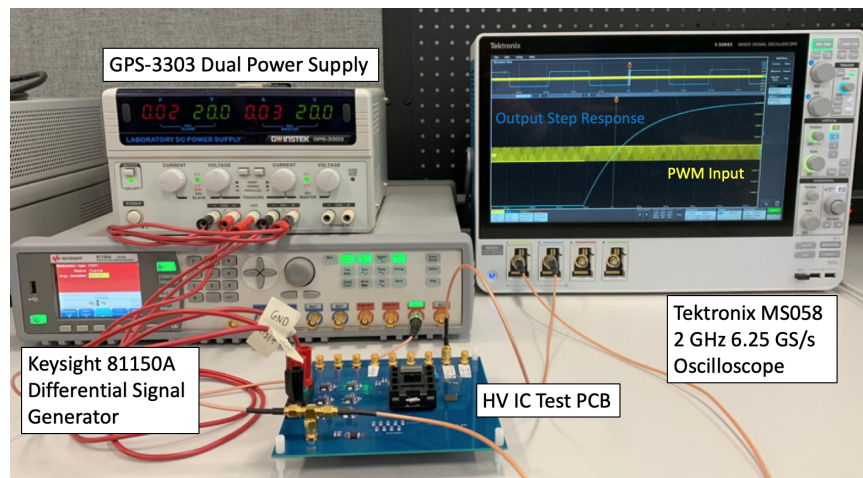
Figure 3.11: HV IC test setup using a custom-built printed circuit board showing the driver output step response to a PWM input with a 10%-90% duty cycle variation.

Device testing was performed in multiple phases, all of which used a custom test PCB designed to accommodate the packaged driver and supply all of the necessary

peripherals. The chip is supplied with external voltages of $\pm$ 3.3V, $\pm$ 11.7V, and $\pm$ 15V from linear voltage regulators on the custom test PCB, while a 1 MHz pulse width modulated signal with $V_{pp} = 3.3V$ is provided by the waveform generator. This signal was then copied and shifted in frequency by a clock IC on the test PCB to supply all nine driver channels. Figure 3.12 shows the unfiltered output of a single channel, demonstrating the circuits ability to produce the desired $\pm$ 15V output voltage.

3.6.1   Basic functional testing
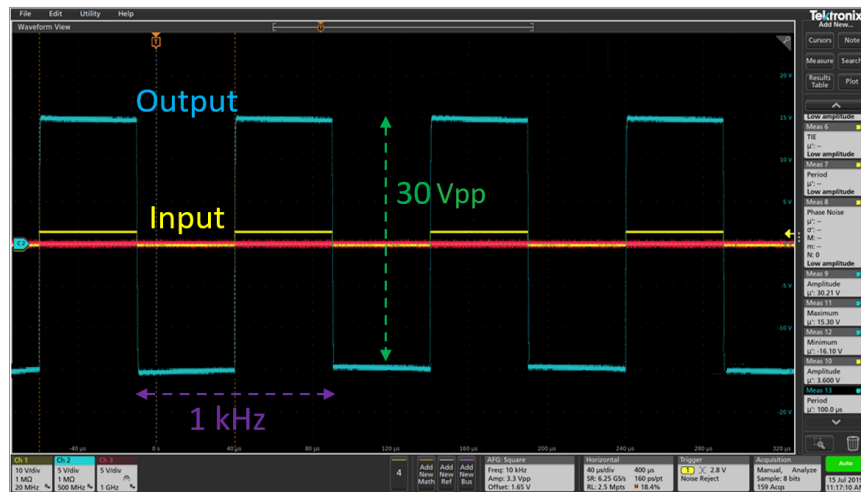
Figure 3.12: Oscilloscope capture showing the unfiltered output response of the driver (blue) for a 0 V$\rightarrow$3.3 V square wave input (yellow). The results show the driver is able to achieve the desired 30 V_{pp} output.

3.6.2   Linearity Test

To test the linearity performance of the design, the output of each channel is filtered by a low-pass filter (LPF) to retain only the dc voltage level and the response is measured for varying duty cycle. The results are plotted in Fig. 3.13 and show that the driver maintains linear operation over the useful current range of approximately $\pm$5 mA.

3.6.3   Step Response

The step response of the driver IC is measured by varying the duty cycle of the input signal from 10% $\rightarrow$ 90% and measuring the rise time of the output. Fig. 3.14 shows
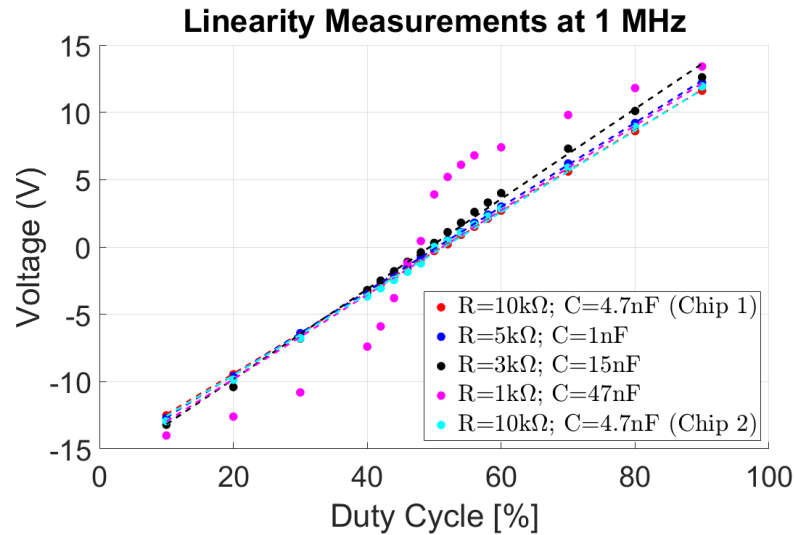
Figure 3.13: Driver output voltage versus PWM duty cycle measurements. A series of different resistor and capacitor values were used at the output to simulate the MEMS load and limit the delivered current. Dashed lines are linear fits to the data. Results show linear operation for approximately ±5 mA.

the results of this test, yielding a measured rise time of 100 μs with a ripple of 140 mV.
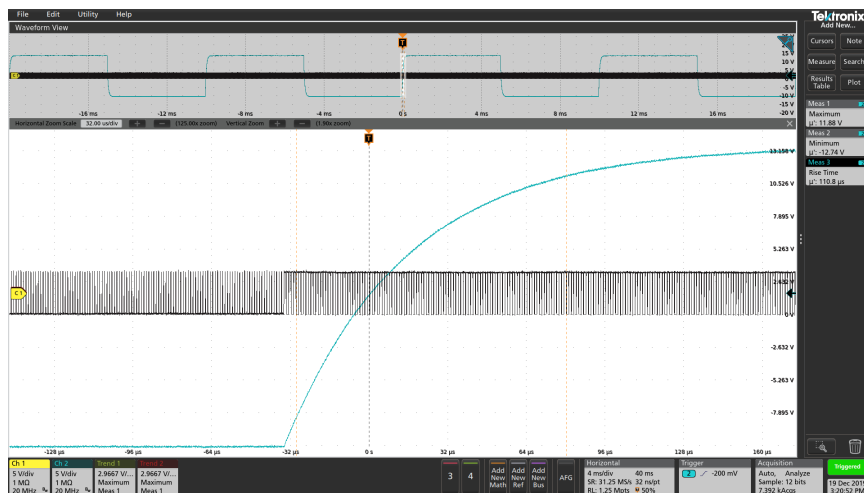
Figure 3.14: Step response test results. The duty cycle of the input signal was varied from 10% to 90% and the response time of the driver circuit was measured.

3.6.4   Power Spectral Density

The power spectral density (PSD) of the driver IC output was used to calculate the
signal-to-noise-and-distortion ratio (SINAD) and effective resolution of the device.
The SINAD is the ratio of the total signal power level (signal + noise + distortion)
to unwanted signal power (noise + distortion).

$$SINAD = \frac{P_{signal} + P_{noise} + P_{distortion}}{P_{noise} + P_{distortion}} \tag{3.5}$$

Figure 3.15 shows the PSD derived from importing the measured duty cycle versus
output voltage data into Matlab/Simulink and modelling the circuit transfer function.
The built-in sinad function, which uses a modified periodogram of the same length
as the input signal, was used to calculate the SNDR. The noise level was modelled in
Cadence to determine a more accurate representation of the noise + distortion due
to transistor switching. In the bandwidth limited case (10 Hz - 1 kHz), the SINAD
measures 47.93 dB.
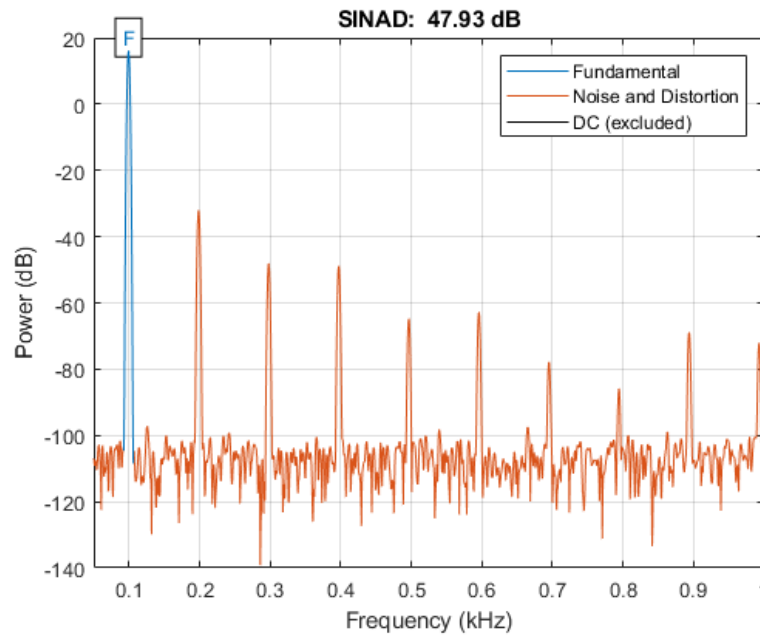
Figure 3.15: Measured power spectral density for driver IC output, yielding a SINAD
of 47.93 dB. The fundamental frequency is shown in blue, while noise and distortion
components are shown in orange.

Process	0.35 μm HV
Max Output Voltage	$\pm$15 V
Area	0.24 mm^2
Operating Frequency	1 MHz
Bandwidth	10 Hz-1 kHz
SINAD	47.93 dB
Power	150 mW (C$_L$=15 pF)

3.6.5 MEMS Driving

We validated the functionality and performance of the IC by interfacing the driver chip with the MEMS DM. Figure 3.16 shows the experimental setup used to determine the MEMS response versus applied current. We selected a test region of the 5×5 actuator array to measure the deflection of a single actuator without being bonded to the mirror membrane. The mechanical decoupling between the mirror membrane and the actuator was done to confirm the behavior of the actuator in more detail. Currents within the known linear operation range of the driver from approximately -5 mA to +5 mA were applied to a single actuator in the presence of a 0.1 Tesla magnetic field. An optical microscope was used to measure the actuator deflection with an accuracy of $\pm$ 2 μm at 50× magnification.

Figure 3.17 shows the results from this test, yielding actuator deflection values from -20 μm for -3.75 mA and +22 μm for +4 mA. Testing was repeated using an RC filter at the driver output (R=3kΩ; C=15pF) to determine the need for additional filtering, however, it was found that the MEMS provided sufficient filtering. This can be attributed to the fact that the MEMS is non-responsive mechanically to the higher frequency components.

3.7 Packaging and Integration

This section presents the design efforts underway for the integration and packaging of the ASIC voltage driver and MEMS DM technologies onto a common substrate for reduced form factor and increased electrical performance (i.e. minimal parasitic effects, lower power consumption, etc...). This is an essential step for future highly multiplexed MOAO systems (e.g. the Gemini Infrared Multi Object Spectrograph
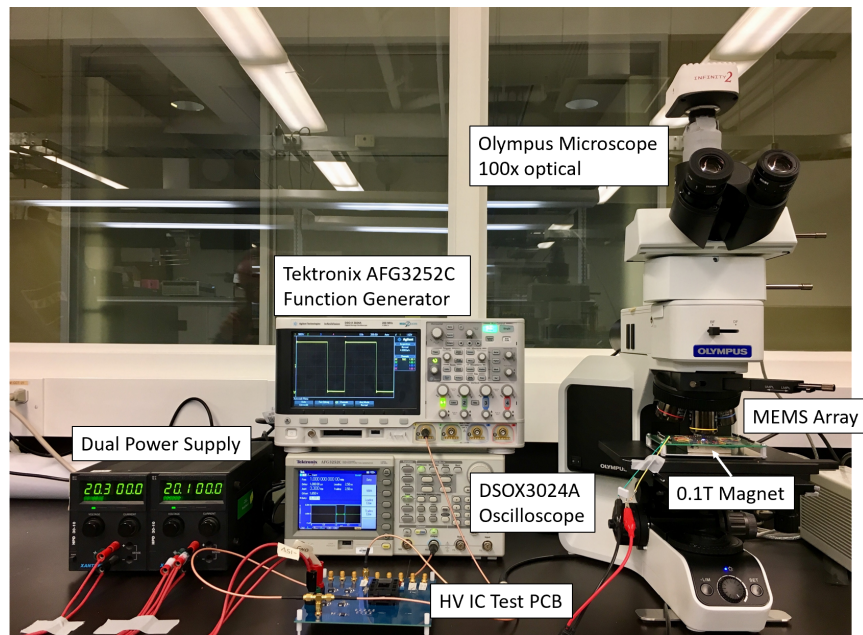
Figure 3.16: Experimental testing set-up for measuring actuator stroke. The custom IC PCB is interfaced with the MEMS actuators to drive them in the presence of a 0.1T magnetic field. Actuator stroke is measured using an optical microscope at 50× magnification.
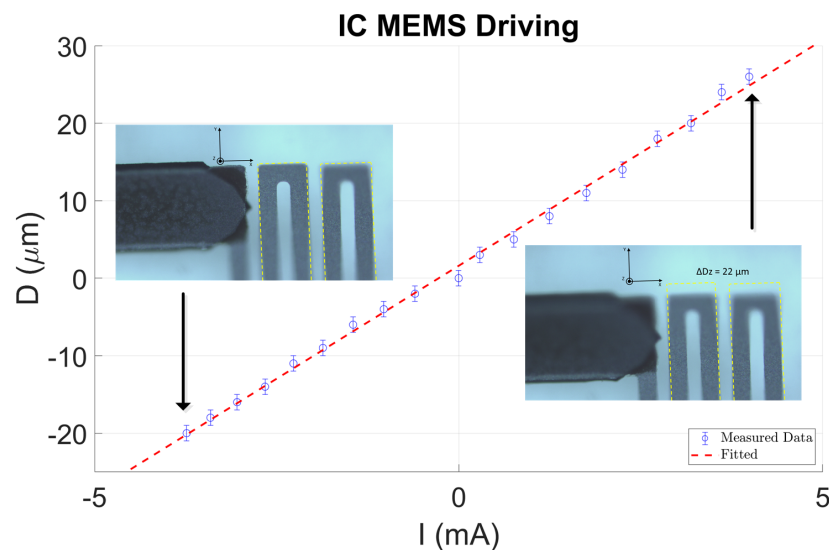
Figure 3.17: Drive current versus MEMS actuator stroke response analysis. Currents from -5 mA to +5 mA were applied to a single actuator in the presence of a 0.1 Tesla magnetic field. Optical images (50x) were taken at the two extremes to show the actuator deflection.

GIRMOS) to reduce both cost and complexity.

Currently all commercially available DM systems come with separate high-voltage drive electronics hardware that connects to the DM device via ribbon cables. To address the need for higher actuator count DM systems, we are exploring different integration and packaging approaches to provide a more compact and power-efficient solution. A task that is being facilitated using high-voltage CMOS process technologies.

Many proven integration and packaging techniques are available in two-dimensions, however, by using the vertical dimension, one can scale the number of ASIC drivers with less restriction and realize the benefits of optimal power-delivery approaches. For this reason, we choose to focus our efforts on 2.5D (in contrast to 2D integration where die are mounted in a single plane, a silicon interposer with through-silicon via (TSV) is used to enable mounting on both upper and lower surfaces) and 3D heterogeneous integration schemes.

Traditionally each chip was packaged individually and then integrated onto a PCB board, allowing for the discrete devices to be fabricated in the most applicable technology. This approach offered optimal design at the individual nodes, however, the overall package suffered from reduced performance, a larger foot-print, and higher power consumption. Since power consumption and form factor are the two dominant driving factors for our design, this type of approach was not feasible.

The idea of combining MEMS devices with ICs is not a new problem and has been addressed in the literature as an important technological advance to achieving system scaling. These devices must be combined to achieve an operational system, since the role of the MEMS is typically to sense or control certain physical quantities, while the IC provides the functionality and interface with the outside world. Our work represents one of the key efforts in providing a novel solution using MEMS/IC integration techniques to solve the issue faced in scaling the drive electronics for large-array DM technologies.

Multi-dimension integration (i.e. >2D) offers the desirable quantity that the driver ICs can be mounted on the backplane of the MEMS actuator array used for the DM, enabling the long lossy ribbon cables to be eliminated. The two main approaches for IC integration in the semiconductor industry with vertical interconnect capability are 2.5D and 3D integration. In each case, two or more levels of electrical components (typically IC die) are vertically integrated using TSVs to connect them into a single package. This type of integration also makes use of solder bumping, but on a much smaller scale to provide high-density connections.

Full 3D IC integration enables vertical stacking of many IC chips using TSVs to connect between the different layers. This type of approach offers the highest possible level of integration and therefore minimal form factor. However, several design challenges are imposed through power delivery and thermal management issues. As an intermediary step between 2D integration and full 3D integration, an approach called 2.5D integration was proposed. 2.5D integration introduces a silicon interposer (device-less silicon wafer) with TSVs drilled through it to connect metal layers called redistribution layer (RDL) that are patterned on the top and bottom sides. This enables lateral communication between different die via the RDLs and vertical communication between the top and bottom sides via TSVs.

We consider two main approaches to system packaging and integration shown in figure 3.19, one with an interposer platform and one without. The advantage of including a silicon interposer layer is that signal routing between drivers and the MEMS actuators will be more efficient in terms of preserving signal integrity and signal routing complexity. Traditional drivers require long wires to connect to the DM which introduces parasitics and presents additional loading on the system. The benefit of an integrated and packaged system is that these effects can be reduced by placing the components much closer together.

3.7.1   2.5D Integration

Our group is currently involved in a prototyping run of a new multi-technology interposer platform being offered through a partnership between Canadian Microsystems
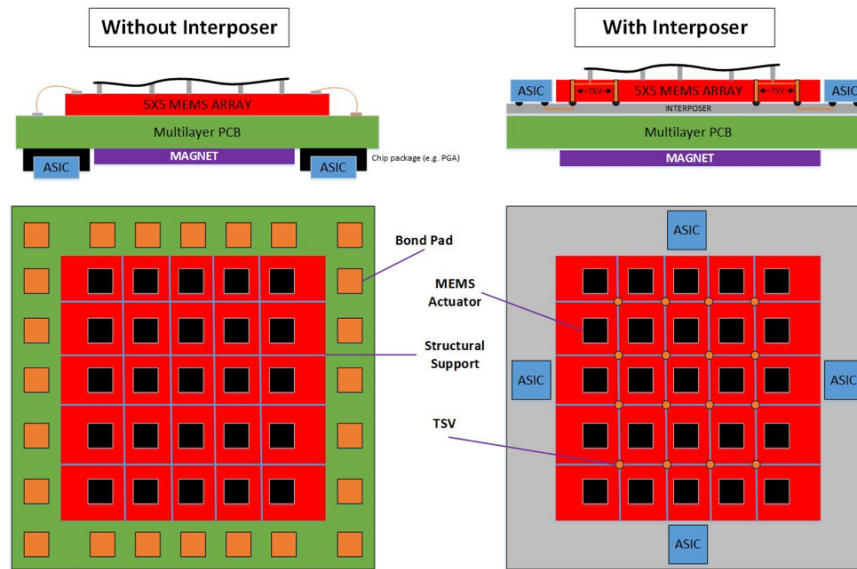
Figure 3.18: Proposed ASIC/MEMS DM packaging and integration architectures using (1) multi-layer PCB and (2) multi-layer PCB + silicon-interposer.

and Innotime Technologies that will enable 2.5D integration of heterogeneous chip technologies. This enables a low-risk/low-cost approach to testing this technology as a viable solution for integration and packaging. In our initial design, the MEMS and multiple ASIC drivers will be integrated onto a single silicon substrate, and routing of electrical signals between chips will be managed through the available RDLs and TSVs. Individual chips will be bonded to the RDLs using either wire-bonding or flip-chip technology (TBD). An example layout is shown in figure 3.20:

3.7.2   3D Integration

The 3D integration approach is currently being explored in collaboration with the Tanaka Lab at Tohoku University, who have expertise in TSV fabrication and 3D IC design. Assembly and testing is scheduled to occur in two different phases. During the first phase, two chips will be 3D stacked and packaged onto a PCB board to simplify the testing procedure. The top chip will be drilled for TSVs and a BGA bumping process will be used to attach it to the bottom chip. Finally, wirebonds will be created between the top chip and the PCB to probe the functionality and performance of the chip-stacking. In the second phase, we will introduce the 2.5D
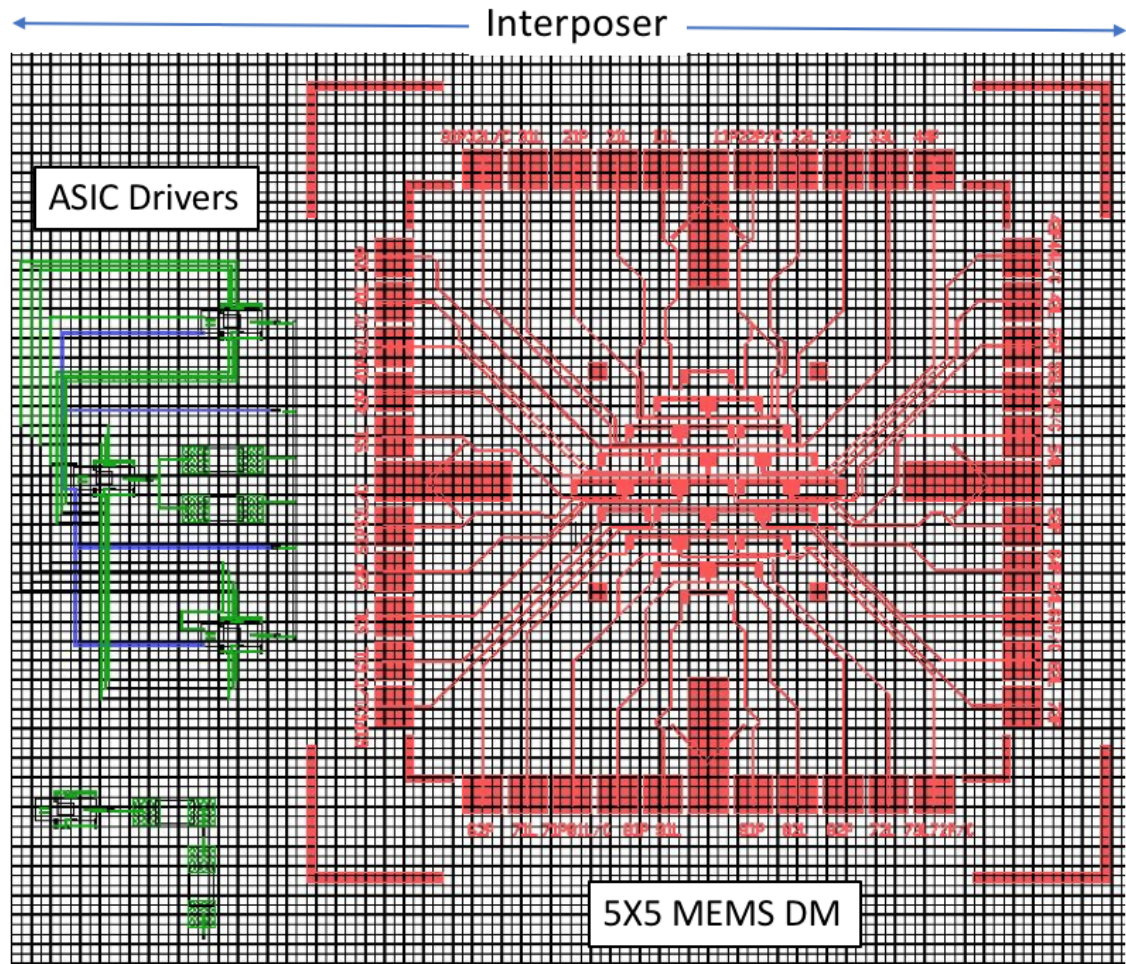
Figure 3.19: Example layout in Tanner Design Suite using the Innotime Process Design Kit (PDK) for 2.5 integration.

interposer platform to interface the 3D stacked ASICs with the MEMs device. In this configuration, the bottom chip in the stack will be drilled for TSVs and face-to-face bonding will be used to connect the upper and lower chips, as well as to the interposer.

In both phases a two tier architecture is adopted (imposed by Tanaka lab fab capabilities) with a 4×4 array of drivers per tier. This gives of total of 32 drivers per package enabling us to test the 5×5 MEMS actuator array. The power consumption per driver is 20 mW (at 1 MHz with a 15 pF load), yielding a 0.3 W total per tier. The current through voltage supply lines is at maximum 0.5 mA. We are currently

looking in to ways to reduce these numbers and preliminary research is presented in the following section.

In phase 1 the MEMS device will be paired via connections to the PCB to test the driving capabilities of the ASIC package. In phase 2, we plan to use the interposer technology to mount the MEMS on the backside of the device and route connections vis TSVs.
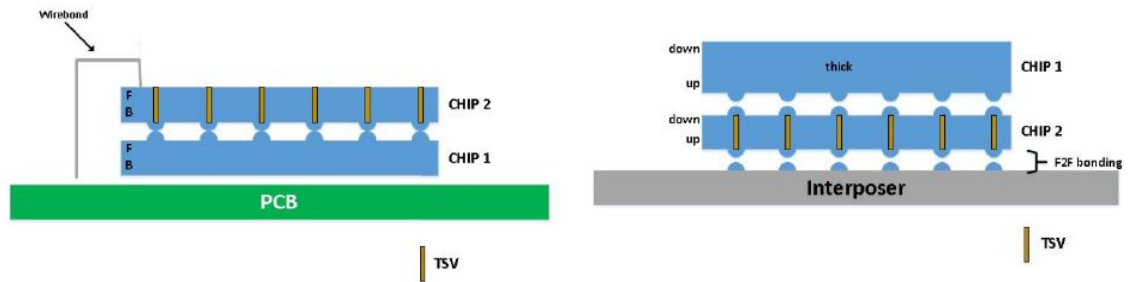
(a) Phase 1 packaging.

(b) Phase 2 packaging.

Figure 3.20: Proposed packaging schemes using 3D integration.

3.7.3 Power Savings for High Actuator Count Systems

There is a global trend towards compact, energy-efficient electronic circuit systems across many industries. As the demand for scalable electronics increases, silicon-based CMOS manufacturing techniques are becoming more widely adopted for the area and power savings inherent to this technology. Despite the growing trend towards low-voltage very large scale integration (VLSI), some applications remain fixed in the high-voltage domain.

A common approach to energy-efficient design is to implement adiabatic stepwise charging techniques, which aim to minimize energy dissipation over conventional CMOS circuits Chernichenko et al. (2012). The energy dissipated in a conventional charging event of a load capacitor C, with constant voltage ΔV, is:

$$E_R = \frac{C\Delta V^2}{2} \tag{3.6}$$

As a result, only half of the energy from the source is stored as electrostatic energy in the capacitor, and the rest is dissipated as heat due to resistance Koller & Athas (1992). Instead of charging the load capacitor directly from V_{SS} to V_{DD}, stepwise charging using N discrete voltage increments, will result in an energy reduction of:

$$E_N = \frac{C\Delta V^2}{2N} \tag{3.7}$$

The charging output waveform will approximate an ideal ramp using n-steps as shown in figure 3.21.
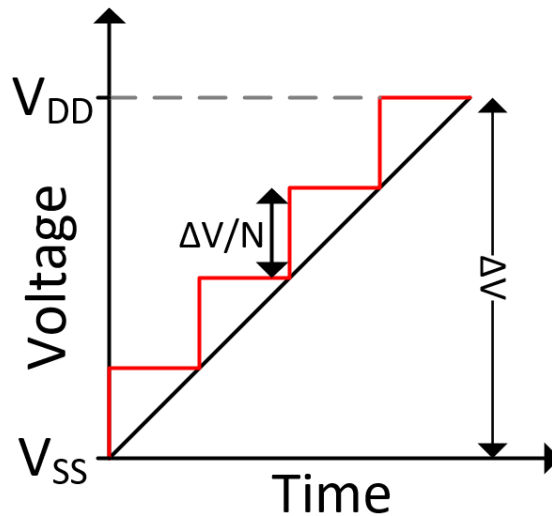
Figure 3.21: Approximation to an ideal ramp charging waveform using n-step charging approach.

The following work is particularly interesting from a microelectronics perspective given that much of the research to date has been focused on low-voltage (i.e. sub 3.3V) systems, not on high-voltage (i.e. >3.3V) drivers. Existing HV drivers in the literature only drive between GND and V_{DD} and have focused on reducing the power consumed by auxiliary circuits. This work is unique in that it focuses on reducing the power of the main driver circuit by attempting to charge the capacitive load adiabatically, like what is done in digital logic circuits. The proposed architecture represents a new approach to stepwise charging the HV driver in a reconfigurable way that will enable significant power savings.

B_0	1	1	1	1	1	0	0	0	0	0	0	0	0
B_1	1	0	0	0	0	1	1	1	1	0	0	0	0
B_2	0	1	1	0	0	1	1	0	0	1	1	0	0
B_3	0	1	0	1	0	1	0	1	0	1	0	1	0
S_1	1	1	0	1	0	1	1	0	0	0	0	0	0
S_2	0	0	0	0	0	0	0	0	0	1	0	0	1
S_3	0	0	1	0	1	0	0	1	0	0	0	0	0
S_4	0	0	0	0	0	0	0	0	1	0	1	1	0
S_5	0	0	0	0	0	1	0	0	0	0	1	0	0
S_6	0	1	1	0	0	0	0	0	0	0	0	0	0
S_7	0	0	0	0	0	0	1	1	0	0	0	1	1
S_8	1	0	0	0	0	0	0	0	0	0	0	0	0
S_9	0	0	0	1	1	0	0	0	1	1	0	0	0
V_{out}	$V_2-(-V_2)$	$V_2-(-V_1)$	$V_1-(-V_1)$	$V_2-(-V_{GND})$	$V_1-(-V_{GND})$	V_2-V_1	$V_2-(-V_2)$	V_1-V_2	$-V_1-V_{GND}$	$-V_2-V_{GND}$	$-V_1-V_1$	$-V_1-V_2$	$-V_2-V_2$

Table 3.2: Relationship between thermometer to binary converter output and multi-level converter in terms of $V_{1/2}$.

Charging Circuit

The overall architecture of the N-step adiabatic charging circuit is shown in figure 3.22. Clock control signals are generated by passing an input signal through a tunable chain of inverters to produce multiple signals with equal delays that can then be input to a thermometer to binary encoder.
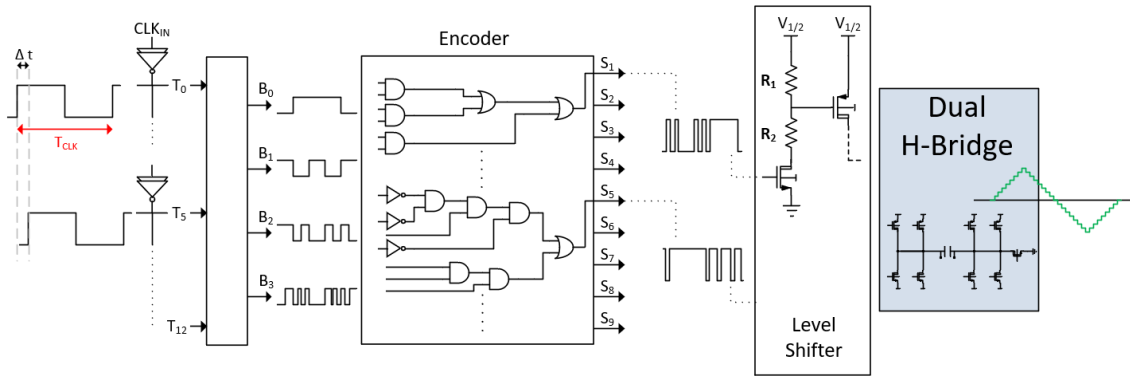
Figure 3.22: Overall N-step adiabatic charging circuit with necessary digital logic operations and level shifting architecture to supply the proposed dual H-Bridge driver. The block diagram shows the relationship between the input signal and the output to the Dual H-Bridge multilevel converter.

The thermometer to binary converter is implemented to transform the control signals to binary numeric, which is subsequently encoded in a set of parallel control signals to drive the multilevel converter.

We have adopted a dual H-bridge architecture proposed in Lin et al. (2009) for ease of implementation on chip. The design is shown in figure 3.23 and includes the necessary circuitry for level shifting the stepped voltage source. The output from the thermometer to binary converter B[0:3] is passed through an encoder stage to produce parallel control signals S[0:8]. Four variable supply voltages $\pm V_1$ and $\pm V_2$ are implemented in the system to power nine transistors in a reconfigurable architecture that allows for five, nine, and thirteen steps to be produced. The total number of steps in the charging process will be determined by the variable voltage supply level conditions. For $V_2 = V_1$, $V_2 = 2V_1$, and $V_2 = 1.5V_1$, five, nine, and thirteen steps can be achieved respectively. Table 3.2 gives a detailed relationship between the thermometer to binary converter output, control signal from the encoder, and the output voltage level of the dual H-bridge.
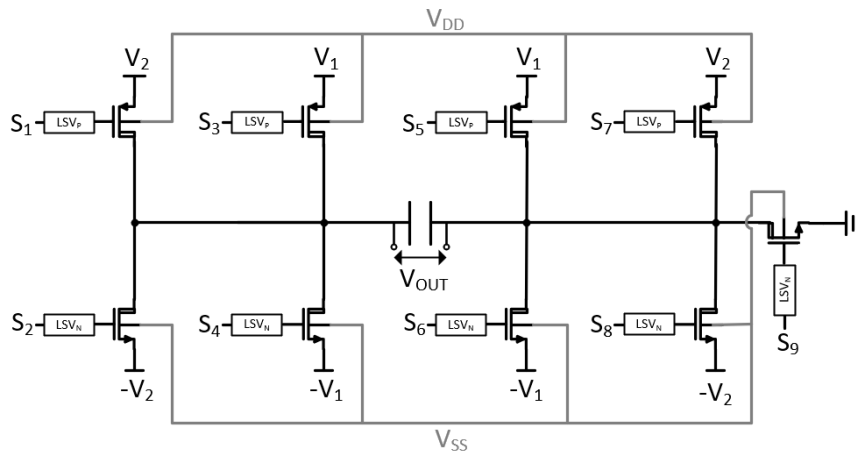
Figure 3.23: Reconfigurable dual H-bridge multilevel converter schematic diagram for stepwise charging.
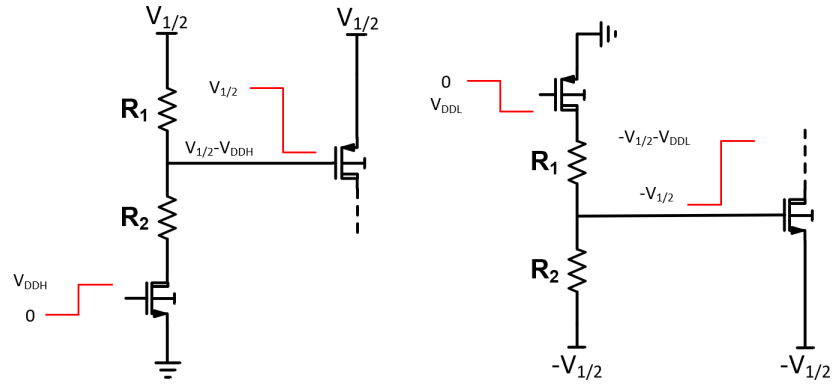
Figure 3.24: HV driver level-shifter for gate protection.

The encoder functions have been implemented using standard logic gates and derived as follows:

$$S_1 = B_0 \cdot B_1 + B_1 \cdot B_2 + B_2 \cdot B_3$$

$$S_2 = \overline{B_0} \cdot \overline{B_1} \cdot \overline{B_2} \cdot \overline{B_3} + \overline{B_0} \cdot \overline{B_1} \cdot B_2 \cdot B_3$$

$$S_3 = B_1 \cdot \overline{B_2} \cdot B_3 + B_0 \cdot \overline{B_1} \cdot B_2$$

$$S_4 = \overline{B_0} \cdot B_1 \cdot \overline{B_2} \cdot \overline{B_3} + \overline{B_0} \cdot \overline{B_1} \cdot \overline{B_2} \cdot B_3 + \overline{B_0} \cdot \overline{B_1} \cdot B_2 \cdot \overline{B_3}$$

$$S_5 = \overline{B_0} \cdot \overline{B_1} \cdot B_2 \cdot \overline{B_3} + B_0 \cdot B_1 \cdot B_2$$

$$S_6 = B_0 \cdot B_2$$

$$S_7 = \overline{B_0} \cdot \overline{B_1} \cdot \overline{B_2} + B_1 \cdot \overline{B_2} \cdot B_3 \cdot B_3 + B_1 \cdot B_2 \cdot \overline{B_3}$$

$$S_8 = B_0 \cdot B_1$$

$$S_9 = \overline{B_0} \cdot B_1 \cdot \overline{B_2} \cdot \overline{B_3} + \overline{B_0} \cdot \overline{B_1} \cdot B_2 \cdot B_3 + B_0 \cdot \overline{B_1} \cdot \overline{B_2}$$

Simulation Results

Cadence Virtuoso Analog Design Environment simulation tool was used to implement the reconfigurable H-Bridge schematic and measure the required power for 2, 5, 9, and 13 level charging architectures. The outputs for the 3 different adiabatic charging configurations are shown in figure 3.25.
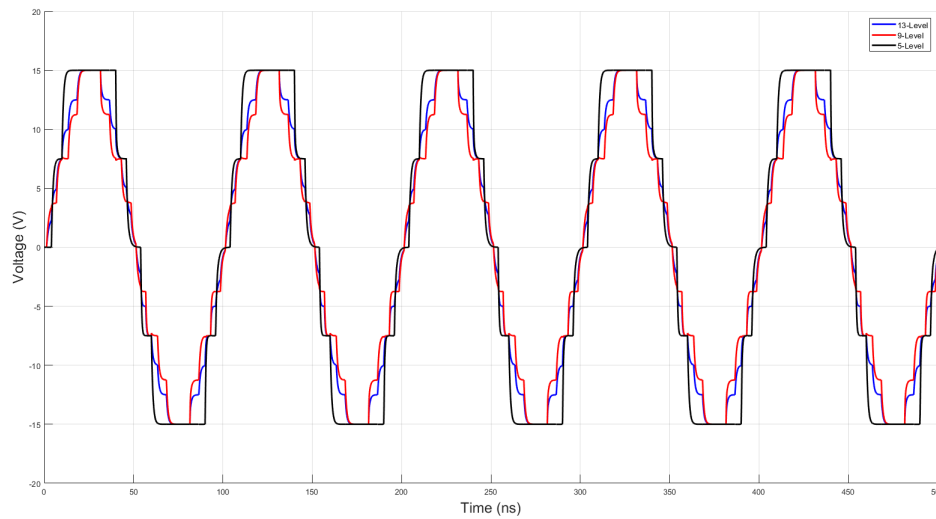
Figure 3.25: Simulation output for 5, 9, and 13 level adiabatic stepwise charging of capacitive load.

Figure 3.26 shows the simulated power savings when moving from a conventional charging event to N=13 steps. The black solid line represents the expected power savings as a function of N derived from theory (i.e. a N^{-1} dependence). This was done by integrating the energy consumed over a single charge/discharge period to yield a baseline for comparison with the simulated results, shown as blue points in the figure. Simulated power consumption was measured in Cadence Analog Design Environment by integrating the current over the rising edge of the stepped voltage curve (i.e. during a capacitor charging event). The total current was then multiplied by $V_{1/2}$ and the switching frequency to field the total power consumed. A line of best fit was then applied to the data for comparison with the expected results from theory. The results show a similar trend, suggesting that as the adiabatic charging circuit complexity increases, the overhead will begin to outweigh the potential power savings.
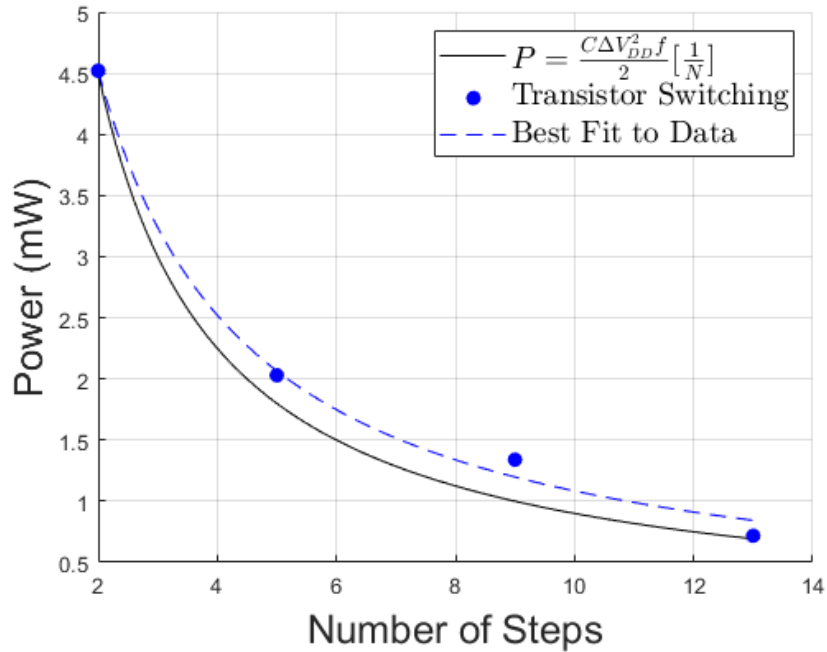
Figure 3.26: Power savings for 5, 9, and 13 level adiabatic stepwise charging.

To produce simulation results that were consistent with theory, it was necessary to implement non-overlapping clocks and optimize the transistor sizing. A parametric analysis conduced in Cadence Virtuoso yielded optimal transistor widths of 5 μm and 25 μm for the NMOS and PMOS devices, respectively. This type of power saving technique shows significant promise for high-actuator count devices and will be explored in future work.

Conclusion and Future Work

A prototype 9-channel IC driver was designed and fabricated using the ams 0.35 μm CMOS process technology. When paired with a novel Lorentz Force MEMS DM, the device demonstrated the ability to provide ± 20 μm with only ± 5 mA of current in the presence of a 0.1T magnetic field. To accommodate the increasing number of actuators required for future ELTs, a reconfigurable power savings technique that adopts adiabatic charging principles used in digital logic circuits was developed and shows a potential power savings of over 80% when compared to conventional approaches. This type of driver architecture is the first of its kind, adopting a mixed signal design with a flexible DSP front end that can be configured to suite a variety of future

project requirements. This type of solution will be critical to allowing low-voltage and low-current MEMS DM technologies to scale to the high actuator count systems being proposed for ELTs. The key differentiation between the work proposed in this thesis and those in the literature today, is that we implement a true low-voltage and low-current DM solution with advanced DSP capability. The elegance in the proposed driver design is that it maintains a relatively simple implementation, while at the same time meeting the requirements of complex, next-generation AO systems.

Future work will include implementing the proposed integration and packaging techniques explored in section 3.7, as well as realizing DSP on-chip to produce a fully integrated solution. Upon successfully achieving these two tasks, the driver will be scaled to a 25×25 architecture and paired with the second generation of Lorentz Force MEMS DM for testing. Pending the results of these tests, the device will be incorporated into an AO test bench before being deployed to a telescope for engineering test runs on-sky.

Chapter 4

Submillimeter Studies of Quasi-Stellar Objects

4.1   Introduction

Submillimetre astronomy is a unique and relatively new branch of study that is poised to answer many open questions in modern-day astronomy. Nestled between the IR and radio wavebands, submillimetre observations span the electromagnetic spectrum from 0.3mm-1mm. While this waveband does provide a unique window into the distant and evolving Universe, it comes with several limitations. Given that this spectral region bridges the gap between traditional optical and radio telescopes, submillimetre instrumentation relies on sophisticated technologies that borrow from both disciplines. From a ground-based astronomy perspective, the submillimetre waveband also suffers from limitations imposed by the Earth's atmosphere. Attenuation by atmospheric water vapour reduces the useable wavelength range to small 'windows' where the opacity allows for sensitive detections. Despite these challenges, valuable science cases continue to drive astronomers to develop the field of submillimetre astronomy.

The submillimetre waveband enables astronomers to probe important physics at all scales. From cosmic microwave background (CMB) studies to examine the early Universe to star formation in local galaxies, this region of the spectrum contains a wealth of information. Of interest to this thesis is the area between these two extremes that probes the physics of galaxy formation and evolution. At these scales, astronomers can study stellar mass assembly and SMBH growth when both processes are expected to have experienced a peak in activity. Observations of continuum emission and spectral features at submillimetre wavelengths provide insight into the cold dust and gas-rich environments inherent to star-forming galaxies at all distances. Although the bulk of the radiation produced during star formation originates in the optical/UV part of the spectrum, it is challenging to observe the radiation at these wavelengths. Significant amounts of dust obscure the process by effectively absorbing the starlight, and reradiating it in the submillimetre waveband.

Many studies support the idea that it is possible to observe star formation in the IR and submillimetre wavebands by probing the thermal continuum emission from dust that has been heated by starlight (e.g. Hughes, Robson, Dunlop & Gear 1993). However, a significant challenge is tracing the origin of the heating, which can be a combination of star formation and AGN activity. By observing bright, distant sources (e.g. high-redshift quasars) in targeted surveys, astronomers can start to understand the nature of submillimetre sources. This thesis aims to study the relationship between the evolution of the host galaxy and the central black hole, using quasars as distant beacons. By examining data taken across as much of the electromagnetic spectrum as possible, the different processes can begin to be disentangled. For example, data from the space-based Herschel observatory (e.g. Pilbratt et al., 2010) at 55671 mu can be used to place constraints on the IR emission of the host galaxies (e.g. Lutz 2014; Casey, Narayanan & Cooray 2014). Similarly, data from X-ray and/or optical observations can independently constrain the AGN power to place constraints on the amount of emission coming from star formation in the IR. Understanding the nature of the connection between AGN activity and star formation in the host galaxy is critical to understanding the mass assembly history of galaxies throughout the history of the Universe.

4.2   Galaxy Overview

4.2.1   Galaxy Formation and Growth

Galaxy formation and evolution is a rapidly developing field that deals with the physical processes and observations that explain how dense, gravitationally bound structures of stars, dust, and cold gas assembled from what appeared to be an initially uniform Universe. As these systems grew under the influence of their own gravity, they began to attract more matter to form dense structures with distinct features. Over cosmological timescales, these initial building blocks merged with other galaxies to form large disk-shaped (or spiral) galaxies (e.g. our own Milky Way) and relatively featureless elliptical galaxies. The galaxies we observe today are the product of billions of years of interactions between stars and other galaxies. Since the speed of light is finite, studying the most distant galaxies (i.e. high redshift) allows astronomers to

peek into the early Universe and inform how galaxies formed and evolved with time. A particularly interesting epoch to study occurs at z = 2, approximately 3.5 Gyr after the Big Bang, where there is a peak in the star formation activity in galaxies. Understanding the processes and composition (i.e. the dust and gas content) of galaxies during this extremely active phase is key to validating details of galaxy growth and regulation in current models.

Star formation is one of the key processes influencing galaxy evolution and it is believed to occur in two distinct modes: quiescent mode and starburst mode. Quiescent or normal star forming galaxies typically follow a power law relationship between SFR and stellar mass, defining a main sequence of star formation (Noeske et al., 2007), and exhibit more extended emission. Starburst galaxies, on the other hand, are outliers that form stars at a much higher rate, depleting the galaxy's molecular gas reservoir on a timescale believed to be shorter than the age of the galaxy. In both cases, star formation is initiated in dense regions of cold dust and gas (i.e., molecular clouds) when a critical mass is achieved. Beyond this mass, called the Jeans Mass, the cloud will collapse under its own gravity. Derivations of this critical mass typically begin by invoking the Virial Theorem (i.e., the total kinetic energy is equal to half the potential energy) as follows:

$$KE = \frac{1}{2}U \tag{4.1}$$

The gravitational potential energy, which is responsible for collapsing the cloud, is given by:

$$U = -\frac{3}{5}\left(\frac{GM^2}{R}\right) \tag{4.2}$$

And the kinetic (or thermal) energy that creates an internal pressure that opposes gravitational collapse is given by:

$$KE = \frac{3}{2}Nk_bT \tag{4.3}$$

where N represents the total number of particles in the cloud, defined as the cloud mass divided by the mass per particle $N = M/m$. The Boltzmann constant, k_b, is

equal to 1.38×10^{-23} J/K. Substituting 4.2 and 4.3 into equation 4.1, the condition for gravitational collapse to occur can be defined as:

$$3\left(\frac{M}{m}\right)k_bT < \frac{3}{5}\left(\frac{GM^2}{R}\right) \tag{4.4}$$

$$\left(\frac{M}{m}\right)k_bT < \frac{1}{5}\left(\frac{GM^2}{R}\right) \tag{4.5}$$

If a constant molecular cloud density ρ is assumed, the size of the cloud can be written as:

$$R = \left(\frac{3M}{4\pi\rho}\right)^{\frac{1}{3}} \tag{4.6}$$

Solving for the mass (M) yields the equation for Jeans Mass:

$$M_J = \left(\frac{5kT}{Gm}\right)^{\frac{3}{2}}\left(\frac{3}{4\pi\rho}\right)^{\frac{1}{2}} \tag{4.7}$$

If the cloud is perturbed such that the mass exceeds the Jeans Mass, it will collapse under it's own gravity and begin to form stars.

Several of the important observed properties of galaxies are summarized below to provide the necessary background for the work presented in Chapter 5:

Morphology

Galaxy morphology refers to the classification of galaxies based on their prominent structural properties. While many classification schemes exist, the first and most common was proposed by Edwin Hubble in 1926 (Hubble, 1926). Hubble proposed an evolutionary sequence that categorized galaxies as ellipticals, lenticulars, or spirals according to their visual appearance. Ellipticals have a spherical or ellipsoidal shape that is driven by random motions of the constituent stars, while spiral galaxies have a flattened disk that is supported by rotation. In reality, most galaxies are neither a perfect elliptical nor spiral type, but a combination of both. Since Hubble first proposed this classification method, several more complete approaches have since been explored by De Vaucouleurs (1959) and Sandage (1986). In each case, the visual appearance of a galaxy is important because it is a function of how the galaxy formed,

its interactions with the surrounding environment, star formation history and many other interesting factors. Therefore, we can tell a great deal about a galaxy based on its morphology.

Luminosity, Flux and Magnitude

Luminosity is the standard measure of radiated electromagnetic power used when characterizing an astronomical object. It is typically expressed in units of energy (joules or ergs) per second and is therefore a measure of the rate at which an object radiates energy away in the form of light. In general, the luminosity of an object is expressed in terms of our Suns luminosity ($L_\odot$), which is 3.8×10^{26} Watts. The Suns luminosity is expressed as the bolometric luminosity, which is the total rate of energy output integrated over all wavelengths. Normally the luminosity will be expressed in terms of a specific waveband defined by the filter used on the telescope. For example, the IR luminosity, which is used to measure the thermal radiation from dust, is measured in the rest frame from $8 - 1100$ μm. Galaxies in our universe span a wide range of luminosities from as low as 1000 times our Suns luminosity to as high as 10^{12} times. The luminosity of any given galaxy depends strongly on the total number stars and can therefore be used to determine the stellar mass (Kuiper, 1938).

Telescopes measure a quantity called flux (S), which is the total amount of energy reaching the detector per unit area per unit time. The relationship between observed flux and intrinsic luminosity of an object is given by the following inverse square law:

$$S = \frac{L}{4\pi r^2} \quad [\text{W/m}^2] \tag{4.8}$$

where r is the radius of a sphere surrounding an object that is radiating in all directions with luminosity, L. The flux measured by a telescope will be a small fraction of the emitted flux, and will depend on the distance between the object and the observer.

An example of how luminosity is calculated can be understood by considering the Sun, which is located 1 Astronomical Unit (AU) (i.e., approx. 1.5×10^{11}m) from Earth. The average observed solar irradiance or flux (power per unit area) at 1 AU is 1.3608 kW/m^2. The surface area of a sphere surrounding the sun out to 1 AU (i.e., the radius of Earth's orbit) is $4\pi(1.5 \times 10^{11}m)^2 = 2.83 \times 10^{23}$ m^2. It follows that the total energy flowing through this surface will be approximately 3.7×10^{26} W. This is

the intrinsic brightness or luminosity of the Sun.

The 'brightness' of an object, as it is observed on Earth, is typically defined by the objects apparent magnitude (m), which depends on the distance along the line of sight. Objects that appear bright in the sky could be so because they are close to us or because they are intrinsically bright. To ensure all objects are compared in a standard manner, the distance dependence is factored out and the absolute magnitude (M) is specified. The absolute magnitude is defined as the apparent magnitude that a star would have at a standard distance of 10 parsecs (pc) (i.e., approx. 3.09×10^{17} m) from the observer. Both absolute magnitude and luminosity are intrinsic properties of an object, and are related by the following logarithmic equation:

$$M_2 - M_1 = 2.5 \log(\frac{L_1}{L_2}) \tag{4.9}$$

Or, inversely:

$$\frac{L_1}{L_2} = 10^{-\frac{M1-M2}{2.5}} \tag{4.10}$$

Since astronomers use the Sun as a standard brightness reference, this equation becomes:

$$L = 10^{-\frac{(M1-4.77)}{2.5}} \cdot L_\odot \tag{4.11}$$

Therefore, an objects luminosity can be calculated in terms of the Sun's luminosity if the objects absolute magnitude is known.

In astronomy, the process of transforming the measurement of light made by a telescope's detector into a useful quantity, such as flux, is referred to as photometry. For transition edge sensor (TES) bolometers commonly used in submillimetre devices, the incoming photons will cause a thermally absorbing material to increase in temperature. This increase in temperature will yield an increase in the measured resistance, which can then be converted to a flux. TES bolometers are calibrated against fluctuations in atmospheric opacity (which results in thermal loading) by measuring the response of the detectors in each filter to a bright source. This data is then used to extract the astronomical signal by converting the electrical signal in the instrument to an observed flux measurement.

Colour

The colour of an astronomical object is measured by the ratio of the luminosity in two different photometric bands or by the difference in magnitude between two different bands. The observed colour of an object will depend on its surface temperature, which defines the peak wavelength of radiation. The magnitude of a star, for example, is not uniform across all wavelengths. For this reason, telescopes use a specific set of filters to measure the brightness of objects over specific spectral regions. It is common for astronomers to use observed data to produce Colour-Magnitude and Colour-Colour diagrams to gain insight into a galaxy's stellar population. By comparing the brightness (or luminosity) with the colour (or relative temperature) of the constituent stars, it is possible to determine the age and metallicity of the stellar population. If a galaxy is brighter in the red filter than the blue, this indicates the galaxy is either older or has a higher metal content.

Environment

The environment in which a galaxy resides has a significant effect of the galaxy's properties. Within a galaxy cluster, the distribution of the different galaxy morphologies in not random but obeys a density-morphology relation. Some galaxies will reside in high-density regions while others will be in lower density regions and certain galaxy morphologies tend to be preferentially found in one region versus another.

Nuclear Activity

Galaxies can be grouped into two main categories depending on their nuclear activity: active galaxies and non-active or normal galaxies. This grouping was necessary since the observed light emitted from some galaxies was not consistent with what would be expected by solely considering the stellar and gas components of the galaxy. This non-stellar component, that is evident in the galaxies spectral energy distribution (SED) (see section 4.2.3), is a result of emission due to an AGN located in the central region of the galaxy. Strong emission in this region comes from matter that is being accreted onto a SMBH.

Redshift

A combination of Doppler motions and the expansion of the Universe cause electromagnetic radiation (i.e. light) from distant galaxies to be shifted towards the red part of the spectrum as the object moves away from the observer. Since the Big Bang,

the universe has been expanding and astronomers have observed that the majority of distant galaxies are moving away from other each other (and us) and that the more distant the galaxy is, the faster it is receding. Observing the light from these distant objects allows astronomers to probe the distant Universe, resulting from the finite travel time of light through space. By measuring the position of spectral lines (i.e. emission and absorption features in the spectrum of an astronomical object), it is possible to gather information about the properties of the distant object. Redshift, z, can be defined in terms of the rest-frame (or emitted) wavelength and the observed-frame (or measured) wavelength as:

$$z = \frac{\lambda_{obs} - \lambda_{rest}}{\lambda_{rest}} \tag{4.12}$$

For reference, a redshift of z = 0 is the local, present day universe and redshifts greater than z>1 are considered high-redshift.

4.2.2 Dusty, Star-Forming Galaxies (Submillimetre Galaxies)

A detailed study by Blain et al. 2002 introduced a population of extremely luminous, high-redshift (z>1) galaxies discovered at submillimetre wavelengths. Observations of these galaxies, made possible with the advent of sensitive mm-wave detector technology, had previously been largely obscured from view in the optical and UV due to radiation extinction from the high dust content. This population of galaxies is named after the fact that the bulk of the energy output is emitted at observed frame submillimetre wavelengths. The source of the submillimetre radiation is a combination of thermal continuum emission from dust grains and line emission from atomic and molecular transitions. While the emission from the latter can be traced to specific molecules (e.g. the rotational transition of CO – used as a luminous tracer for molecular hydrogen (H_2), the fuel for star formation), the source of emission that heats the dust is often unclear. The source of energy could be any process that results in significant optical/UV radiation heating the surrounding dust cloud and re-radiating as thermal radiation in the IR. This radiation is then subsequently redshifted to the submillimetre part of the spectrum by the time it is observed. Two explanations for the origin of the optical/UV radiation is the formation of young high-mass stars that heat the surrounding cold dust clouds or an accretion disk surrounding an AGN.

A combination of cameras that detect continuum dust emission (e.g. the Submillimeter Common-User Bolometer Array 2 (SCUBA-2) on the James Clerk Maxwell Telescope (JCMT)) and interferometers that detect line emission (e.g. the Very Large Array (VLA) and the Atacama Large Millimeter/submillimeter Array (ALMA)) have been used to map the submillimetre galaxy population. Results suggest that the population has extreme far-IR luminosities, 10^{12}-10^{13} times the luminosity of the sun integrated from 8-1100 μm and a redshift distribution that peaks at z~2.5 (Chapman et al., 2005). Insight into these submillimetre galaxies is critical to our understanding of galaxy formation and evolution since it provides a unique window into early star formation environments and processes.

An open question remains as to the origin of the extreme luminosities observed in submillimetre galaxies. Studies suggest that it is elevated levels of star formation triggered by major merger events between galaxies of similar mass ($M1/M2 < 1/4$) that heat the surrounding dust, and not AGN activity (e.g. Tacconi et al. 2008; Engel et al. 2010). When two galaxies merge, their respective molecular gas clouds collide, significantly altering the properties of the individual galaxies through distorted gravitational fields and frictional forces. Since it is impossible to observe this type of phenomena on relevant timescales, complex numerical models are necessary to simulate how merger events can trigger elevated SFRs. An example output from a simulation performed by Hopkins et al. (2005) is shown in figure 4.1.

As the two galaxies merge, tidal interactions that result from perturbed gravitational field gradients cause the molecular gas to be compressed and star formation to be triggered (e.g.Barnes 2004; Saitoh et al. 2009). Near the center of the galaxy, gravitational torques cause molecular gas to fall inward towards the gravitational potential, colliding with other molecular clouds to achieve the Jeans criteria for collapsing and initiating significant star formation. Further out, molecular gas from the individual galaxies collides at different velocities becoming "shocked" as it loses energy and moves inward towards a higher gravitational potential. These perturbations are often linked with starburst events, making them a strong candidate for the intense heating of dust in submillimetre galaxies.
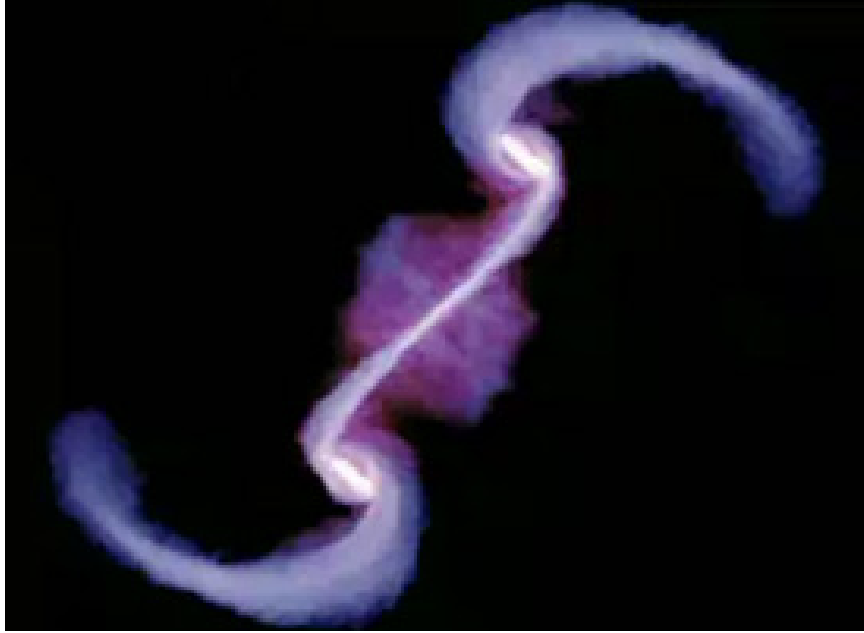
Figure 4.1: Computer simulation showing the merger of two spiral galaxies. The long arms contain gas and stars that have been influenced by tidal interactions. Image courtesy of https://skyandtelescope.org/astronomy-news/galaxy-merger-movies/.

4.2.3 The Spectral Energy Distribution

Galaxy's emit energy over many wavelengths (or frequencies). The SED is a tool astronomers' use to describe the distribution of energy flux from a galaxy at different wavelengths (or frequencies). Each population of galaxies have a uniquely shaped SED that has fundamental information encoded by the underlying physical and chemical processes. This information includes redshift, stellar and gas mass, dust temperature, and SFR. By fitting models of the different processes to the observed multi-spectral data, astronomers can develop an understanding of how the galaxy formed and evolved over time. For the purposes of this work we will break a typical SED (as shown in figure 4.2) into different spectral regions that can be linked to key underlying processes.

Immediately evident is the two prominent peaks at approximately 1 μm and 100 μm, and a series of spectral line features superimposed on the generally smooth shape. The first peak occurs in the UV/optical to near-infrared (NIR) region and is the result of stellar activity in the galaxy. A combination of young, hot, massive stars and old,
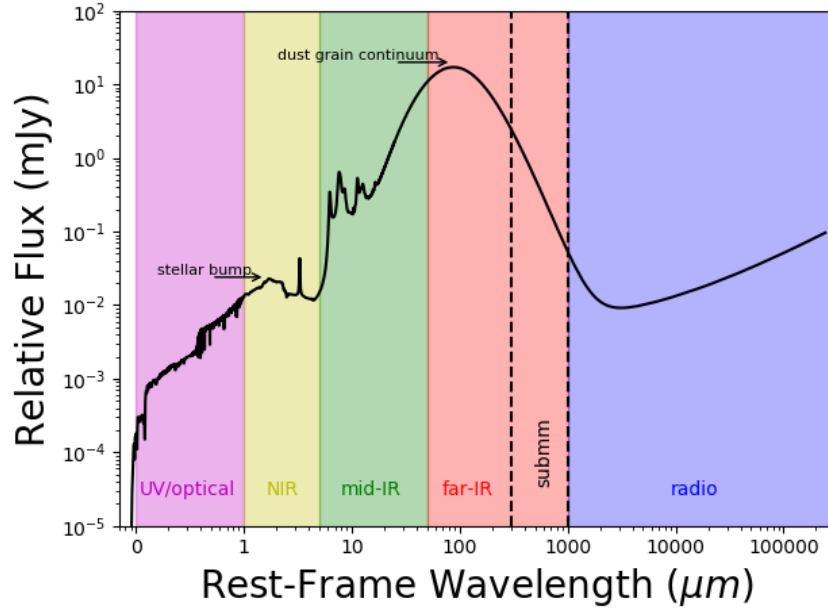
Figure 4.2: Average UV-to-radio SEDs of ALESS sub-millimetre galaxies from da Cunha et al. (2015). The plotted SED represents that of a typical AGN host galaxy that is dominated by heating of dust from young, hot stars. Note: The impact from the AGN is not present in this SED and will be explored in section 4.3.3.

cold, and less massive stars emit blackbody radiation spanning temperature ranges from approximately 3,500K to over 50,000K. In addition to the continuum emission from the total star population, stars emit ionizing radiation that heats the surrounding cloud of dust and gas, producing a series of absorption and emission lines. A unique feature is present at a rest-frame wavelength of 1.6 μm, called the 'stellar bump', and is the result of a minimum in the opacity of hydrogen ions (H-) in the atmospheres of old star populations (Sawicki, 2002). This feature is commonly used to provide an independent estimate of the galaxy's redshift. The relative flux in this region of the spectrum depends highly on star formation activity and is used to study the stellar population (e.g., metallicity and mass distribution). However, a first glance at the submillimetre SED in figure 4.2 would suggest star formation activity is low, which we know is not the case. Intrinsic to intense star forming regions is a surrounding cloud of dust that scatters and absorbs the UV radiation. While scattering can severely attenuate the radiation, absorption of the high energy photons heats the dust and causes thermal radiation in form of a series of modified blackbodies (or grey bodies – see section 4.2.4). By characterizing the peak wavelength for thermal emission

in this region, astronomers can estimate the temperature of the dust. The radio part of the spectrum is a result of both thermal and non-thermal emission processes. Thermal emission occurs as a result of free-free interactions in the interstellar gas (ionised hydrogen (HII) regions) surrounding young, high-mass stars. Non-thermal, synchrotron radiation is the result of relativistic electrons being accelerated in the presence of magnetic fields by supernovae events.

The impact of redshift (see section 4.2.1) on the SED is important to consider when comparing samples of different objects. Consider the SED shown in figure 4.2, which is plotted as a function of rest frame wavelength. Increasing the redshift will cause the SED to shift to longer wavelengths, altering the observed magnitude or flux accordingly. It is necessary for astronomers to apply a transformation, called 'k-correction', to the observed fluxes to convert them into an equivalent rest-frame flux that can be used to compare with other samples. A complete description of the k-correction process can be found in Hogg et al. (2002); Oke & Sandage (1968); Blanton & Roweis (2007).

4.2.4   Modelling Thermal Dust Radiation as a Modified Black Body

Any object with a temperature above absolute zero will emit thermal radiation. In the special case where an object absorbs incident electromagnetic radiation over all wavelengths, it is termed a blackbody. These ideal objects produce a spectrum of radiation that depends only on temperature and is characterized by Plank's law:

$$B_\nu(T) = \frac{2h\nu^3}{c^2} \left[e^{\frac{h\nu}{kT}} - 1 \right]^{-1} \tag{4.13}$$

$$T : \text{Temperature} - [K]$$

$$c : \text{Speed of light} - 2.99 \times 10^8 [ms^{-1}]$$

$$h : \text{Plank's constant} - 6.63 \times 10^{-34} [Js]$$

$$k_b : \text{Boltzmann's constant} - 1.38 \times 10^{-23} [JK^{-1}]$$

The mks units of equation 4.13 are $[W \cdot sr^{-1} \cdot m^{-2} \cdot Hz^{-1}]$.

[Blackbody spectrum according to Plank's Law for three different
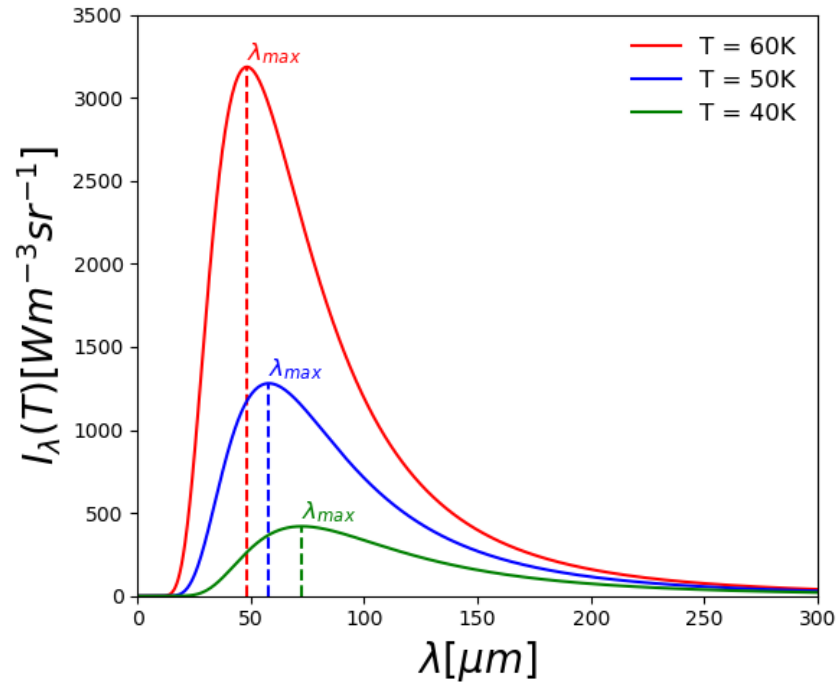
temperatures.]

Figure 4.3: Blackbody spectrum according to Plank's Law for three different temperatures. The wavelength of maximum emission λ_{max} shifts to longer wavelengths as the temperatures decreases.

The shape of the spectrum is shown in figure 4.3 for three different temperatures (i.e. 40K, 50K, and 60K). From this figure we find that the wavelength of peak emission shifts according to the object temperature, with high temperatures yielding a peak at shorter wavelengths. The wavelength of peak emission can be derived from equation 4.13 by setting the derivative with respect to wavelength equal to zero (i.e., $\frac{dB_\lambda}{d\lambda} = 0$). This relationship, given by equation 4.14, is known as Wien's Displacement Law and allows astronomers to estimate the temperature of an object by observing the peak in the radiation spectrum.

$$\lambda_{max} = \frac{2.898 \times 10^{-3} \text{ m·K}}{T} \tag{4.14}$$

The most famous example of an observed ideal blackbody is the CMB, which has a temperature of 2.73K. Most objects, however, are not perfect blackbodies, and it is necessary to account for opacity and emissivity when calculating the flux density. This modified version of blackbody radiation is called a graybody and is given by the

following equation, as presented in, e.g., Choudhuri 2010; Casey 2012; Elia & Pezzuto 2016:

$$S(\nu) \propto (1 - e^{-\tau(\nu)})B_\nu(T) = \frac{(1 - e^{-\tau(\nu)})\nu^3}{e^{\frac{h\nu}{kT}} - 1} \tag{4.15}$$

$S(\nu)$ is the flux density or spectral power per unit detector area and has mks units of $[W \cdot m^{-2} \cdot Hz^{-1}]$. It is common in astronomy to define the flux density in units of Jansky's (Jy) where $1\ Jy = 10^{-26}W \cdot m^{-2} \cdot Hz^{-1}$. $\tau(\nu)$ is the optical depth as a function of observed frequency (ν) and is dependent on the size, density, and opacity of the absorbing material. The optical depth is typically modelled as a power law with exponent β, which is the spectral emissivity index (Hildebrand, 1983):

$$\tau(\nu) = \left(\frac{\nu}{\nu_0}\right)^\beta \tag{4.16}$$

where ν_0 is taken to be the frequency at which the optical depth equals 1 (i.e., $\tau_{\nu_0} = 1$) (Draine, 2006; Casey, 2012). If the object is optically thin (i.e., $\nu \ll \nu_0$), the term $(1 - e^{-\tau(\nu)})$ reduces as follows:

$$\lim_{\nu/\nu_0 \to 0} (1 - e^{-\tau(\nu)}) = \tau(\nu) = \left(\frac{\nu}{\nu_0}\right)^\beta \tag{4.17}$$

In this case, equation 4.15 simplifies to:

$$S_{OT}(\nu) \propto \nu^\beta B_\nu(T) = \frac{\nu^{\beta+3}}{e^{\frac{h\nu}{kT}} - 1} \tag{4.18}$$

The thermal re-radation from dust clouds surrounding active star forming regions is typically modelled using this type of greybody. It is the size and optical properties of the dust, along with the temperature to which stellar radiation has heated the dust, that determines the observed energy spectrum. For dusty star forming galaxies, the spectral emissivity index values typically range from $\beta \approx 1 - 2.5$ (Hildebrand 1983; Casey 2012; Chapin et al. 2011), but a fitted average of 1.5 is often adopted (Casey, 2012). Figure 4.4 shows how the greybody spectrum varies according to different values of T and β.

Optically thin regions are often observed in the long wavelength tail of the dust emission spectrum where astronomers look to directly probe the total dust mass
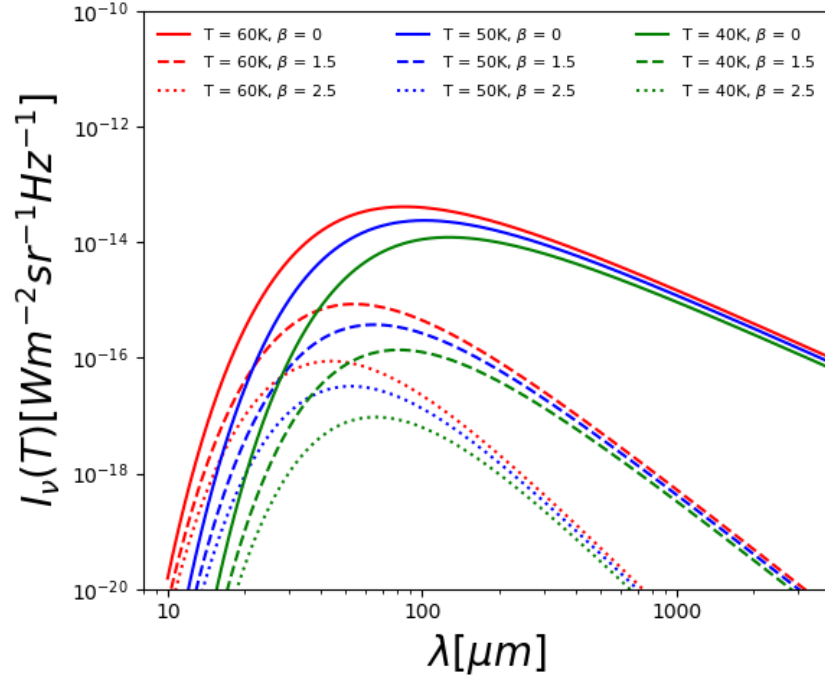
Figure 4.4: Graybody radiation spectrum according to equation 4.18 (i.e., the optically thin case) for three different temperatures: 40K (green), 50K (blue), and 60K (red). For each temperature, three different values of β are plotted: A perfect blackbody with $\beta = 0$ (solid line), $\beta = 1.5$ (dashed line) and $\beta = 2.5$ (dotted line).

(Scoville et al., 2014, 2016). In this region of the spectrum, called the Rayleigh Jeans limit, an approximation to Planks Law can be adopted for the long wavelength thermal emission.

In the limit $h\nu \ll kt$, the exponential term in Plank's Law (equation 4.13) reduces to:

$$e^{\frac{h\nu}{kT}} \approx 1 + \frac{h\nu}{kT} \tag{4.19}$$

This reduces Planck's law to a linear dependence on the dust temperature as follows:

$$B_\nu(T) = \frac{2\nu^2 kT}{c^2} \tag{4.20}$$

Substituting this approximation into 4.18 for the optically thin case gives the following relationship for long wavelength flux density:

$$S_{OT}(\nu) \propto \nu^\beta B_\nu(T) = \frac{2\nu^{2+\beta}kT}{c^2} \tag{4.21}$$

4.2.5   Dust Temperature and Mass

Dust contained within the interstellar medium (ISM) has a profound impact on galaxy evolution and stellar population growth. As a major source of thermal continuum emission in the submillimetre, understanding dust properties and how they influence star formation is critical to understanding galaxy evolution. Dust grains come in a variety of sizes and are composed primarily of silicates, carbon compounds, and ice. Additionally, the surface of dust grains acts as a formation site for H_2, the key ingredient for star formation. The role that dust plays can be understood by observing how it modifies a galaxy's SED, where signatures of absorption, scattering, and re-radiation by dust grains are found. Short wavelength stellar emission in the UV/optical regime is efficiently absorbed or scattered by surrounding dust, significantly attenuating signal strength in this part of the spectrum. This radiation is then re-radiated in the IR to submillimetre as thermal continuum emission, where dust temperatures typically range from approximately 20K-60K (Casey, 2012) depending on the underlying energy source. This process can be modelled using a modified blackbody as described in the previous section and it is common for astronomers to fit template SED's to observed data to derive important parameters that influence galaxy evolution. While the size and geometry of the dust grains do not significantly impact how dust modifies the SED, they do become important when using the multiwavelength data to estimate dust mass.

Assuming an optically thin process in the Rayleigh Jeans regime, which should be true for submillimetre emission (Blain et al., 2006), the dust mass will be directly proportional to the observed flux density:

$$M_d \propto \frac{S_\nu}{\nu^{2+\beta}T_d} \tag{4.22}$$

where it is the dust temperature (T_d) that will determine how accurately the mass can be estimated.

When using a modified black body fit to determine dust mass, it is necessary to assume a value of β. In the event there is sufficient data points, β is varied during

the fitting process, otherwise a fixed value of β is assumed (Berta et al., 2016).

4.3 Active Galactic Nucleus (AGN)

4.3.1 AGN definition and classification

Astronomers observe that many distant galaxies have extremely luminous, compact central cores that often outshine the entire host galaxy. These bright central cores emit energy over a broad range of frequencies, spanning the spectrum from radio to gamma rays, and are designated AGN. The source of energy is thought to be non-thermal since observed luminosities exceed what could be possible from star star-formation alone. Models, combined with observations, suggest it is accretion of material onto a centrally located SMBH (10^6 to 10^{10} solar masses) that fuel these extreme objects (Longair 1996). A rendering of a typical AGN is shown in figure 4.5, with the SMBH located at center.
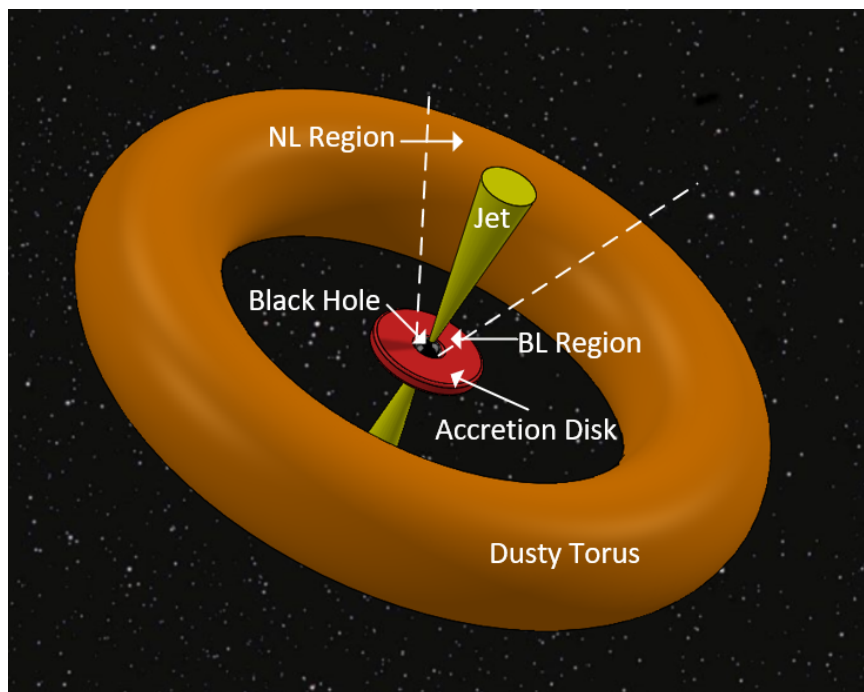
Figure 4.5: Rendering of key AGN features according to the Unified Model.

Surrounding the central black hole out to approximately 1 Pc is the accretion disk where material orbiting the SMBH experiences significant heating as gravitational and frictional forces cause it to spiral inward. As charged particles in the accretion disk

are accelerated to relativistic speeds in the presence of a magnetic field, synchrotron radiation produces highly collimated beams of radio emission or "jets" along the axis of rotation. Moving out to approximately 100 Pc, a surrounding torus of cold dust and gas provides the source of fuel for accretion onto the SMBH. Spectral observations of gas clouds surrounding AGN suggest two different emission line regions: The broad line region (BLR), which models place in close proximity to the central engine, is thought to originate from rapidly orbiting gas clouds with emission lines broadened due to the Doppler effect. The narrow line region (NLR) extends beyond the dusty torus and is thought originate from low density gas clouds with lower orbital velocities.

AGN are observed to have many different properties leading to many different classes of objects (e.g. Seyfert galaxies, radio galaxies, quasars, etc. . .). For the purposes of this thesis, two general classes will be considered: Type I and Type II AGN. Type I AGN are observed to have narrow and broad emission lines present in their optical spectra, while Type II only have narrow emission lines. According to the Unified Model proposed by Antonucci (1993) the variation in properties can be explained by the observer's line of sight to the central region of the AGN. The Unified Model assumes that all AGN are fueled by the same process and that depending on the observer's angle, the dusty torus may be blocking certain features (e.g. the broad line region in Type II AGN). Figure 4.6 illustrates the line of sight dependence on observed features according to the Unified Model of AGN.

4.3.2 Quasars

Quasars (or quasi-stellar radio sources), also known as quasi-stellar objects (QSOs), are the most luminous class of AGN with luminosities many times that of our own Milky Way galaxy. The name quasi-stellar radio source is a historical term that owes its meaning to the fact that quasars were first discovered by radio telescopes and found to have a faint, distant star-like appearance. Quasars are observed to occur over a significant range of redshifts with a peak in activity between $2 < z < 3$ (Richards et al., 2006; Delvecchio et al., 2014), corresponding to a distant epoch. This makes these luminous objects an excellent probe of the early Universe when galaxies were undergoing formation and allows astronomers to study the evolution of their host galaxies.
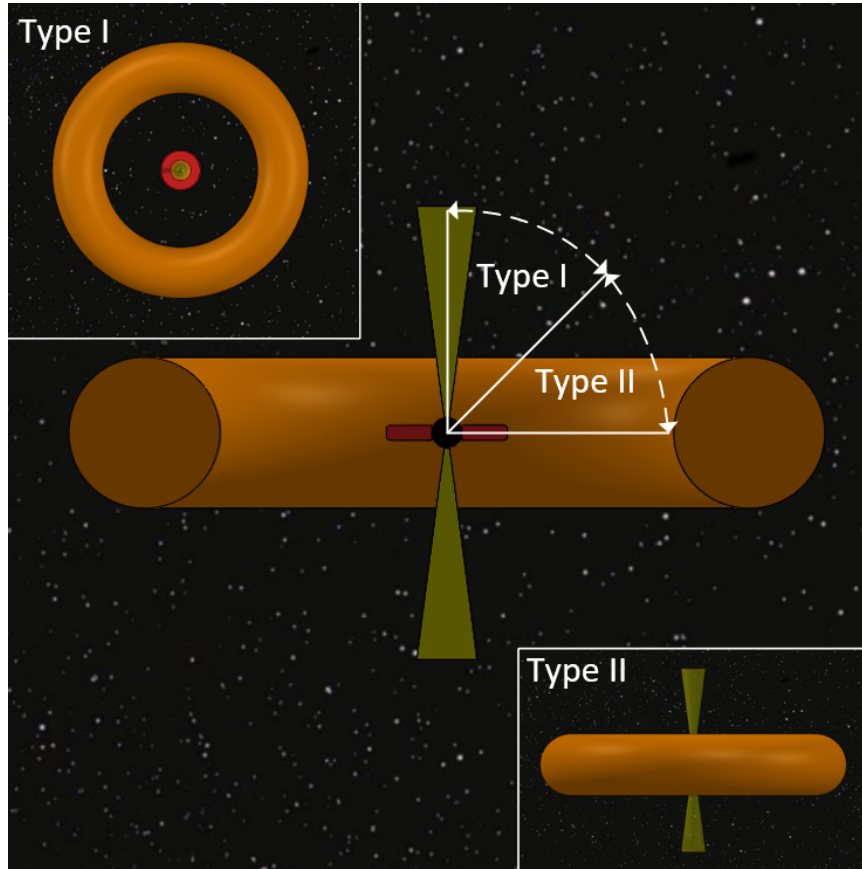
Figure 4.6: Viewing angle dependence proposed by the Unified Model of AGN.

4.3.3 Active Galactic Nuclei Energetics

Even though AGN exist on much smaller physical scales than their host galaxy (sub-parsec versus kiloparsec scales), the total amount of energy they output can often exceed the host galaxy. If this is indeed the case, it stands to reason that the AGN will have a significant impact on the host galaxy properties. Before exploring how the AGN impacts the host galaxy, it is important to understand how the AGN fuels itself and what limits these extremely luminous objects from being destroyed by radiation pressure.

Accretion of matter onto a SMBH is believed to be a highly efficient process compared to nuclear fusion in stars (10% versus 0.7%) (e.g. see Yu & Tremaine 2002). Consider a mass element (m) at a distance R from the central SMBH. The potential energy is given by:

$$E_g = \frac{GM_{BH}m}{R} \tag{4.23}$$

As the mass spirals inward, the potential energy will be converted to kinetic energy, yielding:

$$E_k = \frac{1}{2}mc^2 \tag{4.24}$$

Setting $E_g = E_k$ and solving for the distance R, we find the characteristic size of the event horizon of a SMBH, called the Schwarzschild radius, which is given by equation 4.24. Below this radius, matter will spiral rapidly inward and be consumed by the SMBH.

$$R_s = \frac{2GM}{c^2} \tag{4.25}$$

Therefore, to fuel the central SMBH, gas clouds in the host galaxy must be accreted to near the Schwarzschild radius. The minimum distance that a gas particle must reach is given by 3 times the Schwarzschild radius (i.e. the last stable orbit):

$$R_{min} = 3 \times R_s = 6\frac{2GM}{c^2} \tag{4.26}$$

The luminosity produced by accreting matter onto a SMBH is given by:

$$L_{acc} = \eta \dot{M} c^2 \tag{4.27}$$

where the mass-energy conversion efficiency, η, typically ranges from $\eta = 0.10 - 0.20$ (Yu & Tremaine, 2002) and $\dot{M}$ is the mass accretion rate.

The rate at which the SMBH can grow due to accretion has an upper limit given by the Eddington Limit. Beyond this limit, the outward force due to radiation pressure would exceed the inward force due to gravity, and the system would no longer be stable. The gravitational force is given by:

$$F_{grav} = \frac{GM_{SMBH}(m_e + m_p)}{R^2} \approx \frac{GMm_p}{r^2} \tag{4.28}$$

The radiation pressure force, which is caused by photon momentum, can be derived by beginning with the energy flux at a distance r:

$$F = \frac{L}{4\pi r^2} \tag{4.29}$$

This yields a momentum flux ($P = S/c$) of:

$$P_{rad} = \frac{L}{4\pi r^2 c} \tag{4.30}$$

Finally, the resulting radiation pressure force will be given by:

$$F_{rad} = \frac{L\sigma_e}{4\pi r^2 c} \tag{4.31}$$

where σ_e is the Thompson cross-section, which defines the minimum force due to the absorption by free electrons. Balancing the inward gravitation force and outward radiation pressure force $F_{rad} = F_{grav}$, and solving for L yields:

$$L_{Edd} = \frac{4\pi G c m_p}{\sigma_e} M \tag{4.32}$$

Equation 4.32 describes the maximum luminosity a SMBH with mass (M) can accrete gas.

Figure 4.7 shows how this process manifests itself in a typical AGN SED. Often referred to as the Big Blue Bump, accretion onto the SMBH dominates the energy output in the optical-UV region of the spectrum. The impact of the accretion disk can also be seen in many other regions of the SED. For example, in the IR region, where photons from the accretion disk heat the surrounding dusty torus, causing the energy to be re-radiated as thermal emission.

4.3.4   AGN & Host Galaxies

The significant amount of energy output from AGN not only acts as an excellent beacon for studying galaxy formation and evolution but has the potential to influence the host galaxy through mechanical and radiative processes. There is a consensus among cosmological models and observations that suggest a connection between AGN activity (i.e. SMBH growth) and galaxy evolution (i.e. through star formation), although the exact relationship is not fully understood. For the purposes of this thesis, it is the role of AGN on star formation in the host galaxy that is of interest.
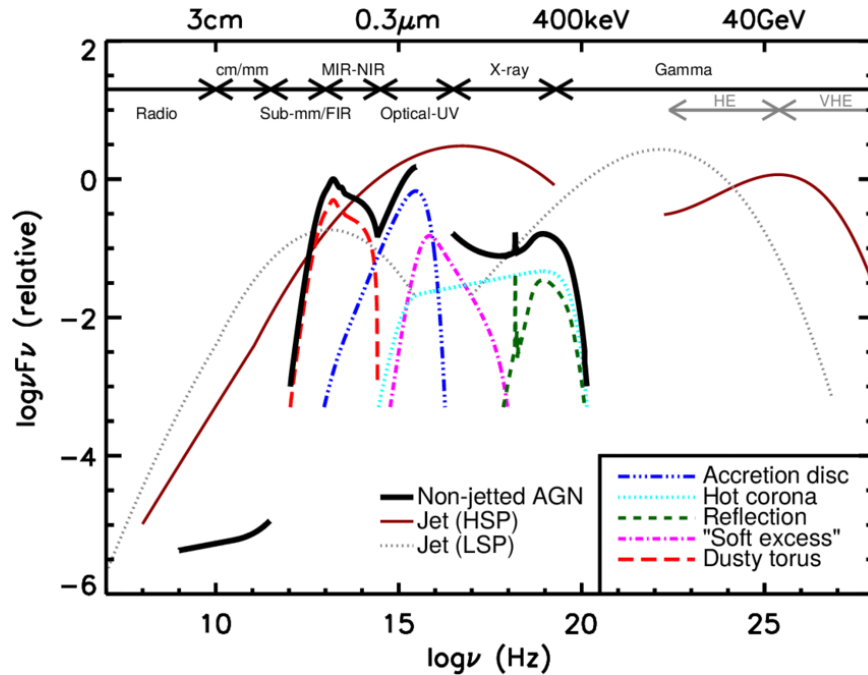
Figure 4.7: Schematic representation of a typical AGN SED from Harrison (2016). Colored lines represent individual processes and solid black line is total SED. This figure shows relative contributions on the different processes to the overall SED with a maximum from the AGN accretion disk in the UV.

Early studies by Magorrian et al. (1998); Gebhardt et al. (2000); Ferrarese & Merritt (2000); McLure & Dunlop (2002); Kormendy et al. (1993) all suggest a tight correlation between the mass of the SMBH and the velocity dispersion and mass of stars in the host galaxy's spheroid (or bulge) component. Given that both SMBH accretion and star formation derive their source of fuel from surrounding cold gas supplies, it is not a surprise that the two processes are somehow linked. The idea that the two processes are linked is further reinforced by the fact that astronomers observe a similar evolution in SFR and AGN activity, with a coeval peak in redshift at approximately z∼2 (Cattaneo & Bernardi, 2003; Madau et al., 1996; Steidel et al., 1999).

Cosmological models of galaxy evolution require a complex relationship to be invoked between star formation and AGN to bring their predictions in line with observations. Specifically, the AGN feedback must regulate the amount of star formation in the host galaxy by limiting the available cold gas supply (e.g. Genel et al., 2014; Schaye et al., 2014). Observations suggest that the feedback mechanism manifests

as an initially infrared (IR) luminous galaxy in the formation stage, but eventually the black hole grows sufficiently large that the QSO terminates or "quenches" star formation (Silk & Rees, 1998; King, 2003; Murray et al., 2005; Fabian et al., 2006). This process, known as AGN feedback, occurs when radiation pressure at the core of the SMBH drives energetic outflows that heat and/or eject the cold gas supplies used to fuel star formation. In the absence of AGN feedback, models will overestimate the size and brightness when compared with observation (Granato et al., 2004; Benson et al., 2003; Ciotti & Ostriker, 2012; Dubois et al., 2013).

4.4   Instrumentation and Data Reduction

Most of the data analyzed in Chapter 5 was collected using the SCUBA-2 camera on the JCMT. A brief introduction to this instrument is provided below. For more information, the reader is referred to Holland et al. (2013).

4.4.1   James Clerk Maxwell Telescope (JCMT) and the Submillimetre Common-User Bolometer Array 2 (SCUBA-2)

The JCMT is the world's largest single dish telescope dedicated to submillimetre studies of the distant universe. Operated by the East Asian Observatory, the telescope is located at an elevation of over 4000 metres on Mauna Kea in Hawaii to minimize the impact from atmospheric water vapor on observations. The 15-metre primary mirror is segmented into 276 aluminum panels that can be individually actuated to control the optical performance of the telescope (typical surface accuracy value of 24 μm). Figure 4.8 shows an image of the telescope at the summit of Mauna Kea.

Light collected from JCMT feeds a series of sensitive millimetre wave instruments, most notably of which is the SCUBA-2 camera. SCUBA-2 is a staple in the submillimetre astronomy community, allowing astronomers to observe the distant universe with great sensitivity. At the heart of the instrument is a 10,000-pixel bolometer array designed to perform wide field surveys of the sky at submillimetre wavelengths. Using bandpass filters tailored to atmospheric transmission windows (see figure 4.9), the camera observes simultaneously at 450-um and 850-um with a 45 arcmin^2 field of view. The imaging array is comprised of eight Molybdenum-Copper bilayer TES bolometer arrays spread evenly across the two wavelengths with 5120 pixels in each
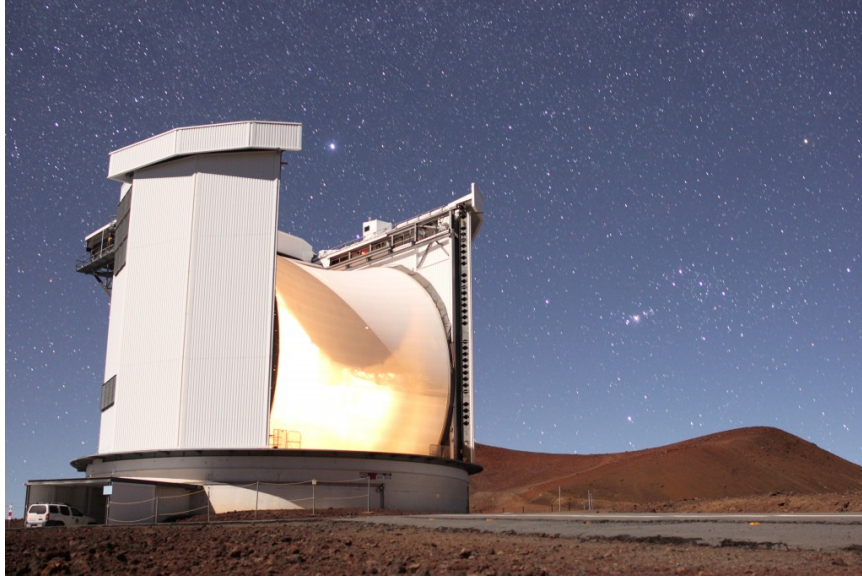
Figure 4.8: The James Clerk Maxwell Telescope (JCMT) on Mauna Kea in Hawaii. Image from https://www.eaobservatory.org/jcmt/public/jcmt/.

focal plane. These sensitive detectors are cryogenically cooled to 100mK using a combination of a pulse tube cooler and a dilution refrigerator. The TES's are slightly warmed using a voltage bias to place them in the desired operating region in the superconducting transition. As incident power from the sky causes the temperature of the absorbing material to change, sensitive amplifiers that use Superconducting Interference Devices (SQUIDs) can register changes in the current through the TESs. Since the devices are very sensitive to changes in thermal loading from the sky, each detector is coupled to a resistive heater that is used to maintain the detector at the desired bias point.

4.4.2 Observing Modes and Calibration

SCUBA-2 offers two unique observing modes (PONG and DAISY mode) which depend on the size of the region the astronomer wishes to observe and the size of the target structures. The PONG observing mode is optimized for covering large areas, while the DAISY mode is used for small, point—like or compact sources on the order of 3 arcmin or less. The data taken for this thesis uses the DAISY mode, so the focus will be on providing the reader a brief introduction to the scan pattern. A comprehensive overview can be found in Thomas & Currie (2014).
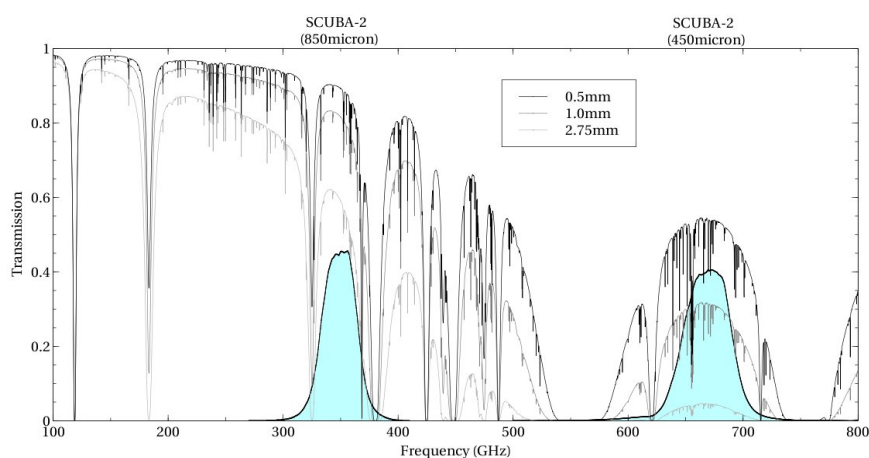
Figure 4.9: Atmospheric transmission and a function of observing frequency for three different levels of PWV. The SCUBA-2 filters are shown in blue for both channels (i.e., 450 μm and 850 μm). Image from https://www.eaobservatory.org/jcmt/instrumentation/.
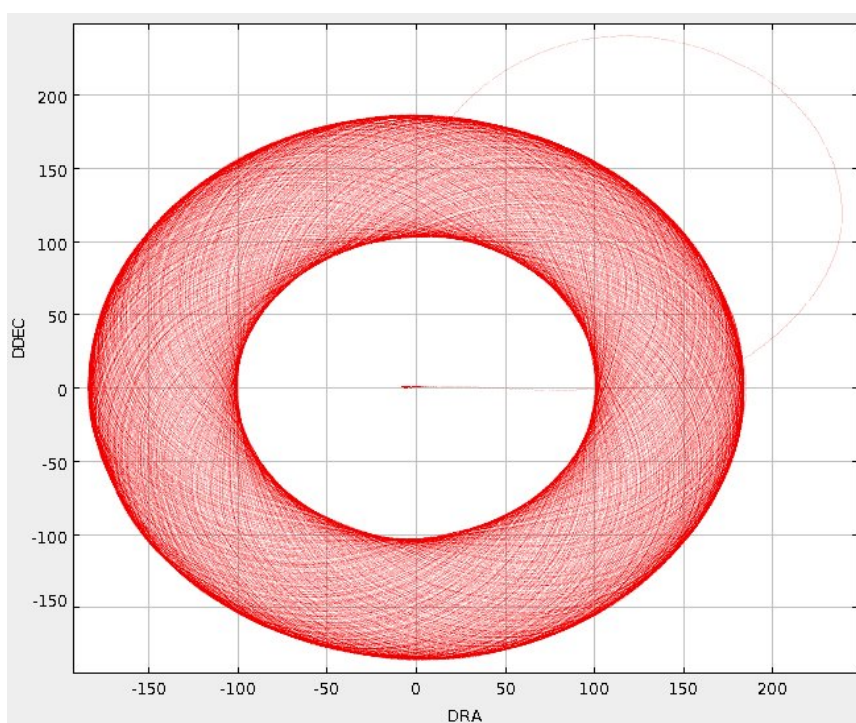
Figure 4.10: SCUBA-2 DAISY observing mode scan pattern. Image from https://www.eaobservatory.org/jcmt/instrumentation/continuum/scuba-2/observing-modes/.

The DAISY mode executes a constant velocity circular-like spirograph mapping pattern on the sky (shown in figure 4.10.) that maximizes the integration time at

the center of image on the target coordinate. This type of pattern optimizes scan velocity to ensure astronomical data is far away from the detector 1/f noise and scan geometry to disentangle source structure from sky noise.

The JCMT and SCUBA-2 require pointing and focus checks before each science observation to ensure accurate data is collected. Pointing the SCUBA-2 camera involves performing short DAISY pattern observations of bright and compact sources that can be used to determine the image centroid. The process begins by specifying the expected astronomical coordinates (RA/DEC) of the source, which are then converted into native telescope coordinates (i.e. azimuth and elevation). A model of the telescope pointing is then created that accounts for any parameter that may affect the accuracy with which the telescope can match the position of the source. Modelled parameters include mechanical misalignments, thermal distortions, atmospheric seeing, and more. Small changes in right ascension (RA) and declination (DEC) are iterated over until the source is in the center of the image. Focus checks involve moving the JCMT's secondary mirror in small increments along the z-axis (defined as the direction between the primary and secondary surfaces) until the signal strength is maximized.

4.4.3 Data Reduction

For a detailed overview of the data reduction process the reader is referred to Jenness et al. (2015).

Data reduction and processing is performed using the Sub-Millimetre User Reduction Facility (SMURF) (Chapin et al., 2013), which takes the raw SCUBA-2 data and transforms it into science images or "maps". The iterative map making process is comprised of two steps: (1) The pre-processing stage and (2) The iterative stage. Before diving into the details of data reduction, it is important to understand the time -varying signal at a bolometer and processes which affect the signal. Equation 4.33 summarizes all the key contributors:

$$b(t) = e(t) \times a(t) + n^w(t) + gn^c(t) + n^f(t) \qquad (4.33)$$

where

$$e(t) : \text{Atmospheric extinction} \tag{4.34}$$

$$a(t) : \text{Astronomical signal} \tag{4.35}$$

$$n^w(t) : \text{Uncorrelated white noise} \tag{4.36}$$

$$g : \text{Scale and offset factor} \tag{4.37}$$

$$n^c(t) : \text{Common code (or correlated) signal} \tag{4.38}$$

$$n^f(t) : \text{Low-frequency noise not included in } n^c(t) \text{noise term} \tag{4.39}$$

The process of making a map from raw data begins by modelling each of these components, removing them in order of largest to smallest contribution, and extracting the desired astronomical signal with some residual noise. One of the biggest limitations of performing ground-based astronomy in the submillimetre is that radiation in this part of the spectrum is highly influenced by the Earth's atmosphere. Even at the best observing sites, the presence of atmospheric water vapour will absorb the submillimetre radiation and attenuate the signal. To model the extinction, precipitable water vapour (PWV) measurements in the observation bands (see figure 4.9) must be collected.

During the pre-processing stage, data are down sampled to save memory and time, and cleaned to remove major spikes and noisy detectors. The process begins by combining individual bolometer timestreams in each subarray and calibrating the raw data by applying a flat field correction. Flat fielding is a standard technique used in imaging to correct for pixel-to-pixel sensitivity variations and optical path anomalies (e.g. dust and scratches on device optics). In the case of a simple CCD camera, the response of each pixel to a uniform illumination is measured and the device is calibrated such that each pixel will respond equally to the same number of photons. For TES bolometers, the process is more complex since the responsivity of the detectors will depend on additional parameters. For SCUBA-2, flat fielding begins by measuring the current through each bolometer as a function of voltage for multiple different resistive heater settings with the telescope shutter closed. The resulting I-V curves are then used to measure how the current through the TES will change in response to a change in resistance. Next, the telescope shutter is open, and the

bolometers are subject to thermal loading from the sky. To compensate for the change in temperature registered by the bolometers, the resistive heater loads are reduced to maintain a constant bias. At this point the detector is recalibrated by measuring the response of the bolometers to the change in sky power. The resistive heaters are ramped through a range of power levels around the nominal value used during the dark calibration and the change in current through the TES is measured. The flat field correction applied to the data is the inverse gradient of the measured current as a function of heater power. This allows the raw unitless data to be converted to units of picowatts (pW). The resultant time series are then down sampled based on the telescope scan speed and the required pixel size, and a series of cleaning routines are run. A quality assurance process flags high noise bolometers and other obvious sources of noise to be removed. Once this process is complete, the iterative stage begins. Each of the components listed above is modelled and removed from the cleaned time series data. This process is repeated until the map converges to an accurate depiction of the science or astronomical observations. The final step is to convert the map from units of pW to astronomical flux (i.e. Jansky's) by applying a flux conversion factor (FCF) that depends on the optical throughput of the telescope and camera. The FCF is measured by observing bright objects with well known fluxes, such as Jupiter, Uranus, or any other calibrator source.

Chapter 5

Submillimeter Study of Hyper-Luminous Quasi-Stellar Object Properties

The work described in this chapter was performed as part of the SCUBA-2 Web survey (PI: S. Chapman), which resulted in three publications: (i) The SCUBA-2 Web Survey: I. Observations of CO(3–2) in hyper-luminous QSO fields (Hill et al., 2019), (ii) The SCUBA-2 Web Survey: II. Sub-mm detections of Hyper-Luminous QSOs (*Ross et al., in preparation*), and (iii) Two sub-millimetre bright protoclusters bounding the epoch of peak star-formation activity (Lacaille et al., 2019). The survey was designed to study the cosmic web, which is the vast network of galaxies throughout the Universe that are connected by gas filaments and separated by large voids. Specifically, this work looks to provide insight into a population of rare, extremely bright QSOs, called hyper-luminous quasi-stellar objects (HQSOs), and their host galaxy environments. For the purposes of this study, a HQSO is defined as any QSO having an AGN luminosity $L_{AGN} > 10^{14}$ solar luminosities ($L_\odot$). The study uses submillimetre data that were collected using SCUBA-2 on the JCMT to observe 15 fields known to contain some of the brightest QSOs ever observed. The fields were selected based on optical data previously made available through a spectroscopic survey of the distant universe called the Keck Baryonic Structure Survey (KBSS) (Rudie et al., 2012). Given that these fields had already been well characterized at other wavelengths, they represent ideal candidates for follow-up studies to provide a more complete understanding of these rapidly star forming environments. The work by Hill et al. (2019) was aimed at characterizing the QSO host galaxies by performing spectroscopic measurements of the cold and dense molecular gas environments, using an interferometer to probe CO transition lines. These transition lines are produced when gas is heated by optical/UV emission from stars, providing insight into star formation activity and physical conditions of the gas (Da Cunha et al., 2008). As a compliment to the study of gas properties presented in Hill et al.

(2019), this work probes the modified blackbody emission (i.e. continuum emission) from galactic dust, which is typically heated by stars. A key question that this work hopes to inform is the relationship between AGN activity from the HQSOs and star formation in the host galaxy at a time of peak activity in the Universe for both star formation and accretion activity in AGN. The HQSOs studied in this work lie within a redshift range ($z = 2.57$ and $z = 2.86$) known to contain a peak in star formation and AGN activity. One of the most interesting results presented in this work, is that all 15 of the HQSOs have statistically significant (i.e. $> 3\sigma$) fluxes detected at 850 μm (3 mJy$<S_{850}<$9 mJy). However, only 6 of the sources are detected at 450 μm, due to the poor atmospheric transmission profile (see section 4.4.1). The 100 percent submillimetre detection rate contrasts starkly with all previous attempts to measure the IR output of HQSOs with single dish telescopes, which is typically 10-30 percent, and at best achieved 50 percent in a sample of QSOs studied by Page et al. (2000).

The HQSO's are all observed to have UV luminosities of $\nu L_\nu = 0.4$ –1.6×10^{14} $L_\odot$, making them some of the brightest sources in the sky. At the same time, they are found to have comparable 850 μm flux densities to typical submillimetre galaxies from SCUBA-2 surveys (Geach et al., 2017). This implies that activity in the host galaxies appears to accompany the most luminous phases or largest black hole masses of QSOs. To place the HQSO's in a more general context, this study uses other less luminous HQSOs lying in the same fields, along with literature HQSO surveys as control samples. Initial results suggest that the copious IR luminosity (i.e., star formation rate) observed from the host galaxies does not simply scale with the UV luminosity (i.e., AGN activity).

This chapter explores the link between IR luminosity (L_{IR}) and the very high L_{UV}, to probe the relationship between star formation and AGN properties in a population of rare, hyper-luminous QSOs. The IR luminosities referenced in this work are measured in the Rayleigh Jeans part of the spectrum where UV emission from star formation is known to efficiently heat dust grains and dominate AGN activity. A study by Kennicutt Jr (1998a) suggests that under these conditions, the IR luminosity can act a tracer of the galaxy's SFR. In section 5.3.3, modelled SED's are fit to the SCUBA-2 data to estimate the temperature of the dust. In the cases where 450 μm emission is detected, it is found that the QSOs are hotter than typical submillimetre

galaxies as shown in Chapman et al. (2005) and Swinbank et al. (2014). This implies that some of the emission in the IR could potentially be coming from dust that has been heated by AGN activity. However, in all cases it is clear that the UV emission is coming from the hot accretion disk around the central blackhole. The L_{AGN} values presented in this work use a scaling factor from L_{UV} that characterizes the typical total AGN luminosity in quasars. A conversion factor of 5.6 is adopted to remain consistent with the results presented in Hill et al. (2019). This study finds that several of the detections by SCUBA-2 at 850 μm show sizeable offsets from the QSO position derived from the optical data. In some cases, the offset is significant enough that at least part of the 850 μm luminosity may not represent emission from the QSO host, but rather a companion SMG. The impact of offset is considered in section 5.3 and is essential to ensuring that it's the host galaxy of the QSO itself that is rapidly forming stars, and not a companion galaxy.

5.1   Introduction

As was introduced in Chapter 4, the relationship between star formation in galaxies and the presence of a central SMBH is a critical issue being addressed in modern-day astronomy (Croom et al., 2004). In particular, it is important to understand the formation and evolution of massive galaxies and how the governing processes interact with each other. These galaxies are understood to form their stellar-mass structure through an initial period of star formation, followed by a period during which mass accretes onto the SMBH, known as an active galactic nucleus (AGN) phase. Feedback mechanisms then act to heat the host galaxy's molecular gas, driving powerful outflows in the form of winds or jets. Direct observations of this process are limited by dust obscuration in these environments. Instead, astronomers seek to observe the galaxies in the infrared/submillimetre region, where a significant fraction of the luminous energy is re-radiated after being absorbed by the dust. To understand the way star formation and AGN activity affect each other, it is necessary to make observations over a redshift range where these processes are dominant. Although they occur on vastly different spatial scales, both processes are observed to have similar evolutionary peaks in the $2 < z < 3$ range (e.g. Wall, Pope & Scott 2008) and therefore objects spanning this redshift range are good targets for disentangling the

underlying processes.

Two different star formation modes (e.g. Elbaz et al. 2011) and the idea that both these modes are potentially regulated by AGN outflows was introduced in 4.3.4. The most commonly observed type of star formation occurs in a "quiescent" mode, with gas conversion time scales on the order of 1 Gyr. The less common mode, and the one that is expected to precede the luminous QSO phase, occurs on a much faster timescale (around of 10^7 to 10^8 yr) in the form of star-bursts. In both cases there appears to be an upper limit on the amount of star formation imposed by the presence of an AGN in the host galaxy. This limitation is believed to be a result of energetic outflows that eject gas from the interstellar medium (ISM), therefore inhibiting star formation on timescales that are much shorter than the gas depletion timescales. The idea of "AGN quenching" is supported on both a theoretical (i.e., in models) and observational basis (Noeske et al., 2007).

This chapter explores the relationship between star formation and AGN properties in a population of rare QSOs, hyper-luminous in the ultra-violet. The sample is characterized by probing their far-IR luminosities and dust masses, using SCUBA-2 observations of the HQSOs. The sensitive submillimetre observations undertaken in this work effectively probe the dusty ISM in the host galaxies of the 15 hyper-luminous QSOs, all with bolometric luminosities exceeding 10^{14} L$_\odot$ (and directly measured UV luminosities of νL_ν=(0.4 − 1.6)×10^{14} L$_\odot$. This approach to studying the host galaxies of HQSOs complements and extends previous submillimetre observations of UV-luminous QSOs (Page et al. 2001; Omont et al. 2003; Priddey et al. 2003; Stevens et al. 2005; Schulze et al. 2019) to higher AGN luminosities, which will be introduced in subsequent sections.

5.2   Observations and Analysis

5.2.1   Sample selection

As part of the SCUBA-2 Web Survey, several proposals were submitted to the JCMT Time Allocation Committee (TAC) to observe the 15 KBSS fields in the submillimetre using the JCMT and its SCUBA-2 camera (Holland et al., 2013). The SCUBA-2 Web Survey uses data previously collected from the KBSS; Trainor & Steidel 2012, 2013),

which is a spectroscopic survey of the distant universe targeted at probing galaxies and their environments at a unique redshift range representative of peak star formation (Reddy et al., 2008) and SMBH growth (Richards et al., 2006). The survey, which comprises 15 individual fields each centered on bright QSOs, was designed to perform spectroscopic measurements of the background QSOs and high-redshift star forming galaxies that lie in the foreground. These KBSS fields were selected based on the configurations of the bright HQSOs at $z= 2.5 - 3.0$ and the fact that a large range of environments exist throughout the target redshift space. All 15 fields have been previously studied at other wavelengths, allowing this study to draw on existing high signal-to-noise UV (rest frame) and optical (rest frame) spectra of the HQSOs. The names and properties of the 15 QSOs are listed in 5.1.

The KBSS QSOs are all measured to have $L_{AGN}>10^{14}L_{\odot}$, with the exception of Q0142 which is subject to gravitational lensing. Gravitational lensing is caused when the light from a distant object is distorted by the gravitational field of intervening structure between the source and observer. The influence of gravitational lensing on a source is dependent on many factors, but ultimately results in the observed flux being boosted by some factor. In the case of Q0142, the QSO is gravitationally lensed by a factor 3.2 with some degree of uncertainty in the lensing model (Sluse et al., 2012), and its intrinsic $L_{AGN} = 6.3x10^{13}L_{\odot}$ is significantly lower than the next most luminous QSO in the sample. For sample uniformity, the analysis in this chapter omits Q0142, however, its submillimetre properties are tabulated for completeness. To place these KBSS QSOs in context with recent all sky surveys for distant luminous QSOs, the sources presented in this thesis are compared with a population of quasars from the Wide-field Infrared Survey Explorer (*WISE*) survey (Tsai et al., 2015) that have been selected based on their far-IR luminosities (the sample includes the KBSS QSOs). The WISE survey performed sensitive infrared mapping of the sky with bands centered at 3.4, 4.6, 12 and 22 μm using a 40-cm space based telescope. This study uses a subset of the *WISE* sample data, limited to sources with $L_{AGN}>10^{14}L_{\odot}$, and a redshift range $2.57 < z < 2.86$ to compare with KBSS redshifts. Figure 5.1 shows the mid-IR colour-colour diagram using 3.4, 4.6, and 12.0 μm data, and the bolometric luminosity distribution as a function of infrared colour. This comparison reveals that the KBSS QSOs (all having $L_{AGN}>10^{14}L_{\odot}$, also derived from observed
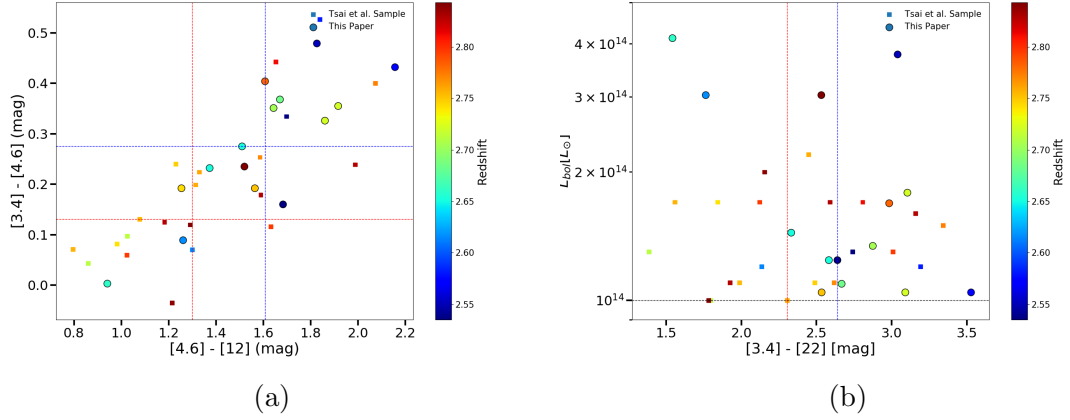
Figure 5.1: Sample selection: (a) Mid-IR colours of the hyperluminous ($L_{\mathrm{bol}}{>}10^{14}\mathrm{L}_{\odot}$) quasars detected by the *WISE* satellite (filled squares – Tsai et al. 2015), along with the KBSS QSO sample used in this work (filled circles). (b) The bolometric luminosity, L_{bol} versus mid-IR colour of the *WISE*-selected quasars and the KBSS sample. The dashed line shows the bolometric luminosity limit of $L_{\mathrm{bol}}{>}10^{14}\mathrm{L}_{\odot}$. This comparison reveals that the KBSS QSOs span a similar colour range as the Tsai et al. (2015) sources. Tsai et al. (2015) sample mean colours are shown as dashed red lines and the sources in this work are shown as dashed blue lines. Comparing the two samples reveals that the sources in this study are on average slighty redder than those presented in Tsai et al. (2015).

optical to mid-IR bands) span a similar colour range to these $L_{\mathrm{AGN}}{>}10^{14}\mathrm{L}_{\odot}$ QSOs from Tsai et al. (2015). From the sample means plotted in figure 5.1, it is evident that the sources in this work are only slightly more reddened than the field *parent* sample at all colours. For the sample in this thesis, the average [3.4]-[4.6], [4.6]-[12], and [3.4]-[22] colours are found to be 0.27 ± 0.13, 1.61 ± 0.30, and 2.64 ± 0.52 respectively. In comparison, the Tsai et al. (2015) samples yields average [3.4]-[4.6], [4.6]-[12], and [3.4]-[22] colours over a comparable redshift range of 0.13 ± 0.14, 1.29 ± 0.36, and 2.31 ± 0.56 respectively. This comparison also reveals that the KBSS QSOs include four of the five most luminous QSOs in the Tsai et al. (2015) sample, but otherwise are representative of the luminosity distribution of $L_{\mathrm{AGN}}{>}10^{14}\mathrm{L}_{\odot}$ QSOs.

In general, the KBSS fields should be relatively unbiased as extragalactic survey fields, outside the volume around the QSO redshift itself. Nonetheless, it is important to acknowledge any potential biases that may be present. In three of the fields, spectroscopic survey data reveals a strong overdensity in galaxies at certain redshifts, evident of massive structures that could evolve into massive galaxy clusters at the

present epoch. In the HS1700 field, the $z = 2.7$ QSO is known to lie behind a $z = 2.3$ structure (Steidel et al., 2005; Chapman et al., 2015a) and should be unaffected by the presence of the galaxy cluster. A study by Chapman et al. (2015b) revealed the HS1700 QSO to be in a small group of galaxies at z∼2.7, as is typical for massive QSOs (Trainor & Steidel, 2013). In HS1549 and HS1603, the $z = 2.84$ and $z = 2.65$ QSO's are known to lie within the structure (Steidel et al., 2011), making them something of biased fields. In addition to these 3 fields, Q0821 and Q2343 are found to be highly overdense in 850 μm sources (Chapman et al. in prep), despite not showing strong overdensities at these redshifts in the spectra obtained during the KBSS survey.

5.2.2   SCUBA-2 850 and 450 μm Imaging

Data were collected at 450 μm and 850 μm using the SCUBA-2 camera on the JCMT in several periods from December 2011 to March 2019, utilizing 151 hours of SCUBA-2 time. The SCUBA-2 camera was used in the standard DAISY observing mode (e.g. Dempsey et al. 2013 - see section 4.4.2 for a summary), allowing a subset of the array to always stay on the target field. In two cases (HS1549 and Q2343) it was necessary to expand the field coverage by offsetting the telescope pointing from the source and stitching multiple images together. Observations occurred in approximately 30-min blocks, using a nearby blazar (i.e. an AGN oriented such that the observer has a clear line of sight to the central region) for pointing checks and focus checks as required. Atmospheric conditions were monitored by taking precipitable water vapour measurements with both the JCMT and adjacent CSO radiometers. These data were cross-checked with a series of measurements taken by the telescope at different elevations (called skydips) about twice per night. The flux density calibration process introduced in section 4.4.2 was carried out using Uranus as the primary calibration source (Sandell, 1994; Jenness et al., 2002). Uncertainties in the calibration measurements were estimated to be about 10 percent at 850 m and 15 percent 450 m. The target for the observations was to achieve a uniform noise level of ∼ 0.7 mJy at 850 μm to ease subsequent statistical analysis of the submillimetre data. All of the data were collected in Band 1 (better than 82% transmission at 850 μm and 28% at 450 μm) to Band 2 (better than 77% transmission at 850 μm

Table 5.1: Observed properties and far-infrared luminosities estimated from the data presented. The UV luminosity of the QSO is also listed (see text for details).

Source	RA/Dec	$\Delta RA/\Delta Dec$	$z_{\rm QSO}$	t_{int}^i	S_{850}	S_{450}	$\log(L_{UV})^a$	$\log(L_{\rm IR})^{b,c}$	$T_{\rm d}^d$	$M_{\rm d}^e$
	[J2000]	[arcsec]		[hr]	[mJy]	[mJy]	[$L_\odot$]	[$L_\odot$]	K	$\times 10^8$ M$_\odot$
Q0100+130	01:03:11.265 +13:16:17.79	(3,0)	2.721	3.5	6.0±1.2	<35	13.81	12.78 ± 0.12	<77	5.2±1.0
HS0105+1619	01:08:06.407 +16:35:50.20	(1,1)	2.652	7.5	3.8±0.6	<24	13.65	12.58 ± 0.16	<90	3.3±0.5
Q0142-100	01:45:16.605 -09:45:17.05	(5,2)	2.743	8.0	7.0±1.3^f	<38	13.30^g	11.86 ± 0.07^g	<66	6.2±1.0
Q0207-003	02:09:50.717 -00:05:06.29	(2,1)	2.782	15.0	5.5±0.8	28.5±7.7	13.79	12.74 ± 0.14 (2.1)	62 $^{+23}_{-14}$	6.1±0.7
Q0449-1645	04:52:14.243 -16:40:16.23	(3,3)	2.684	7.5	4.7±0.9	<46	13.60	12.67 ± 0.19	...	4.1±0.8
Q0821+3107	08:21:07.623 +31:07:51.31	(3,5)	2.616	8.5	3.9±0.6	<23	13.61	12.85 ± 0.15	<92	3.4±0.5
Q1009+29	10:11:55.599 +29:41:41.81	(2,3)	2.652	6.0	8.8±1.1	<38	14.04	12.95 ± 0.13^h	<46	7.7±0.9
SBS1217+499	12:19:30.780 +49:40:52.45	(2,1)	2.704	6.5	4.9±1.1	45.1±11.0	13.71	12.69 ± 0.23	175 $^{+50}_{-25}$	9.8±0.9
Q1442+2931	14:44:53.541 +29:19:05.57	(1,1)	2.660	3.5	2.8±1.0	<42	13.69	12.45 ± 0.36	...	2.4 ±0.9
HS1549+1919	15:51:52.458 +19:11:04.14	(1,1)	2.843	16.0	8.0±1.2	33.6±4.6	14.17	12.90 ± 0.06 (1.5)	47 $^{+8}_{-6}$	7.6±1.0
HS1603+3820	16:04:55.377 +38:12:01.57	(2,1)	2.551	6.0	7.7±1.2	33.4±10.8	14.04	12.89 ± 0.04 (1.6)	45 $^{+35}_{-15}$	7.5±1.0
Q1623-KP77	16:25:48.799 +26:46:58.50	(0,0)	2.535	14.0	4.6±1.7	<21	13.51	12.32 ± 0.38	...	4.0 ±1.5
HS1700+64	17:01:00.652 +64:12:09.02	(1,1)	2.751	20.0	2.3±0.6	15.3±4.1	14.13	12.36 ± 0.25 (5.7)	102 $^{+28}_{-17}$	6.2±0.5
Q2206-199	22:08:52.076 -19:43:59.87	(2,3)	2.721	8.5	7.0±1.3	<43	13.65	12.85 ± 0.19	<92	6.1±1.1
Q2343+125	23:46:28.258 +12:48:57.87	(0,1)	2.573	19.5	6.2±1.1	38.8±9.0	13.58	12.79 ± 0.02 (2.8)	81 $^{+69}_{-26}$	8.9±0.9

^{a} The $L_{\rm UV}$ uncertainty is less than 0.01 in $\log$(L$_\odot$), and is not included in the table.

^{b} When T$_d$ is measured through 450um detection, the $L_{\rm IR}$ value is estimated for this hotter temperature, but otherwise it assumes the 35K SED of Swinbank et al. (2014).

^{c} Quote the L$_{\rm IR}$ from a direct conversion from S$_{850}$, with the scaling factor in brackets when a 450 μm detection allows for a measurement of the T$_d$ and the associated higher L$_{\rm IR}$.

^{d} If the 450 μm measurement limit constrains T$_d$ to less than 125 K (the hottest detected source in the sample), the value is explicitly indicated. Otherwise it is indicated with a '...', since the $T_{\rm d}$ value is not constrained to <200 K in any of the other sources.

^{e} Dust mass is calculated assuming the measured dust temperature, or using 40 K if only an upper limit on temperature is constrained from the lack of a 450 μm detection.

^{f} Q0142-100 has a companion source presented in (Hill et al., 2019). The 850 μm flux is composed of both the QSO and the companion with a flux ratio of 1:10.

^{g} Q0142-100 is gravitationally lensed by a factor of 3.2 (Sluse et al., 2012); the $L_{\rm IR}$ and $L_{\rm UV}$ have been corrected for magnification effects by dividing by 3.2.

^{h} Hill et al. (2019) identify a companion source contributing an approximately equal amount of flux based on CO(3-2) measurements, effectively boosting the S$_{850}$ measurement by a factor of 2.1. The companion contribution to L$_{\rm IR}$ is corrected for by dividing the 450 μm and 850 μm flux densities by 2.1.

^{i} Integration times listed in this table sum to 98% of the total observing time, accounting for failed scans.

and 19% at 450 μm) weather conditions at the JCMT, which are considered the driest of observing conditions for high sensitivity observations. In both bands, this is equivalent to less than 1.58mm of PWM. [1]

Data were reduced with the STARLINK SMURF package as described in section 4.4.3 and presented in Chapin et al. (2013). The data pipeline parameters were optimized for deep blank fields, as described in Geach et al. (2017), by filtering the data to reject power at frequencies outside of the desired angular scales. The submillimetre photometry of the HQSOs and another 20 QSOs lying in the same fields is measured as described in section 5.3, and the final photometry results are listed in Table 5.1. All of the HQSOs are detected at 850 μm at $> 3\sigma$, while six are also detected in the 450 μm band at $> 3\sigma$. Figure 5.2 shows the 850 μm and 450 μm data from SCUBA-2 for all of the 15 HQSOs as contours overlaid on Infrared Array Camera (IRAC) channel-4 (8-μm) images from the Spitzer Space Telescope. Some of the SCUBA-2 detections appear offset (within the SCUBA-2 beam) from the IRAC position of the HQSOs, prompting an analysis in section 5.3 aimed at estimating whether these offsets are consistent with statistical and pointing errors.

5.2.3   Flux density measurements of submillimetre sources

Flux densities were measured at 850 μm for the QSOs by searching SCUBA-2 images that had been convolved with the telescope beam to increases the SNR of point sources, and suppress structure on larger spatial scales. Data were loaded into the Graphical Astronomy and Image Analysis Tool (GAIA) for each of the 15 fields to search for the brightest peak within a 15″ diameter circle, centred on the respective central QSO target coordinates. For point sources these peaks provide a good estimate of both flux density and astrometric position. The uncertainty in the flux density is taken to be the rms at the position of the source, derived from the variance map that is produced by the *SMURF* pipeline. This is slightly better than the spatial rms found in the neighbouring regions of the map itself, as expected since the data is approaching the confusion limit at 850 μm for JCMT. The confusion limit is the sensitivity limit of the telescope, defined as the level of fluctuations in the background sky below

---

[1] https://www.eaobservatory.org/jcmt/instrumentation/continuum/scuba-2/time-and-sensitivity/#Atmospheric_transmission
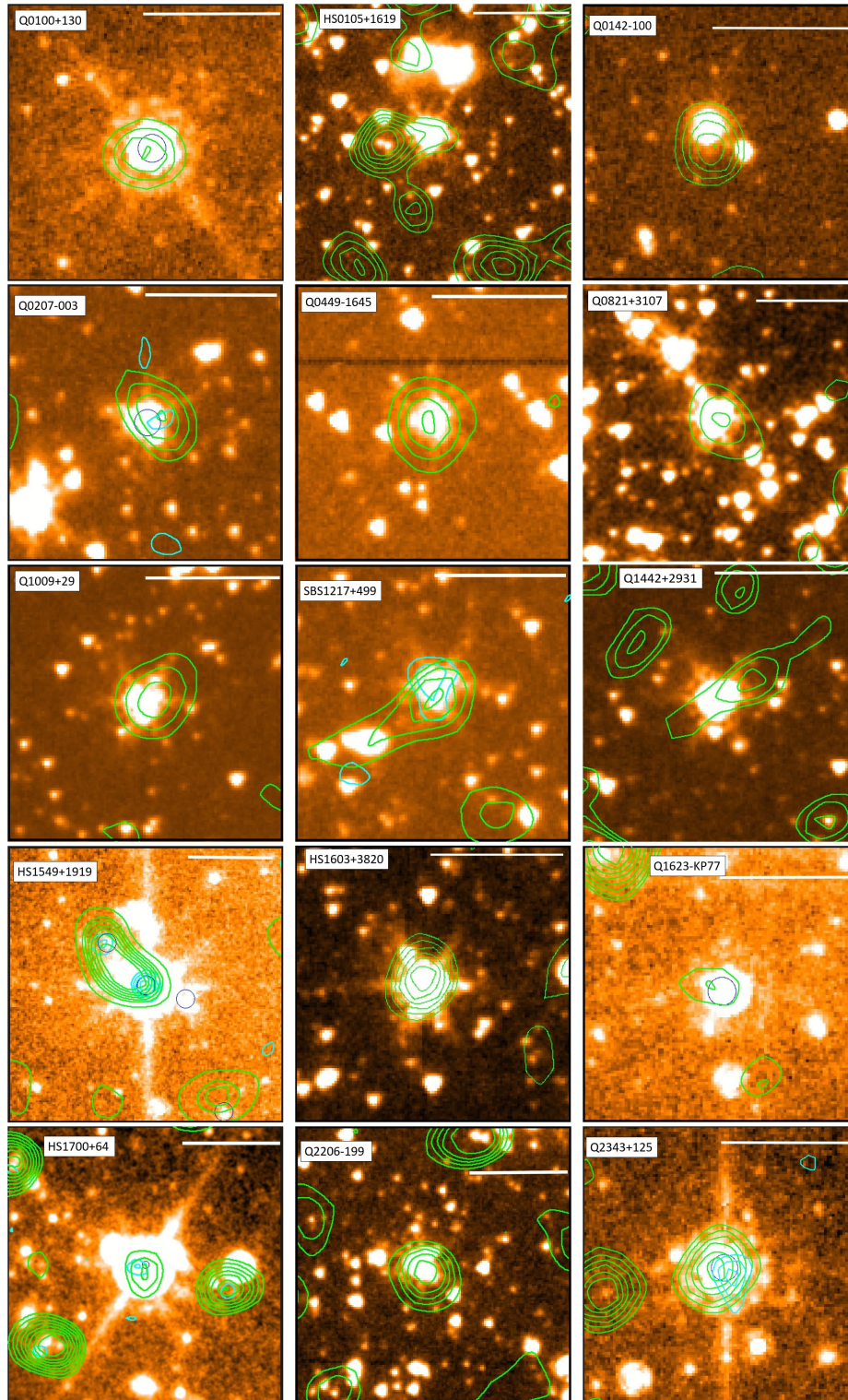
Figure 5.2: IRAC channel-1 cutout images (between 1 arcmin and 3 arcmin on a side) around each HQSO, depending on the presence of a known proto-cluster of galaxies in the field. The bar shows a 30 arcsec scale in each panel. SCUBA-2 observations are shown as contours starting at 3σ for 850 μm in green and 450 μm in cyan. Blue circles show the HQSO (centred), as well as other known QSOs in the field. Larger areas are shown for dense fields that have nearby, well-detected 850 μm sources for astrometric reference.

which individual sources can no longer be detected. Once the telescope reaches the confusion limit, further integration will not improve sensitivity since the Airy-disks of individual discrete objects will begin being superimposed on one another.

The rms of the JCMT pointing limits the accuracy of the SCUBA-2 positioning to about 1 arcsec (Geach et al., 2017), where many repeat visits to the same field beat down the typical 2-3" rms pointing accuracy of the telescope, leaving only lower-level systematics.

Figure 5.2 shows that the SCUBA-2 detections are not always exactly centred on the HQSOs as defined by the IRAC optical data, although the QSOs are always well within the SCUBA-2 beam. If the offsets are real, they may be indicative of submillimetre-luminous companions to the QSOs (e.g. Ivison et al. 1999, Ohyama et al. 2004, Trakhtenbrot et al. 2017). Figure 5.3 shows the radial offsets from the QSO position (defined by centroiding the IRAC 4.5 μm image) to the SCUBA-2 850 μm position. Overlaid are the $1''$ pointing uncertainty of JCMT, the typical statistical uncertainty associated with the beam size and S/N of the SCUBA-2 detections, and the combination of the two. The results suggest that the observed distribution in radial offsets is consistent with what is to be expected given the statistical uncertainties in the measurements. This issue is explored further in section 5.4, drawing on the results of Hill et al. (2019).

In Hill et al. (2019), the molecular gas in the host galaxies is directly identified through the ^{12}CO(3-2) emission line. It is important note that some of the SCUBA2-detected QSOs have close SCUBA2 detected companions (lying $\geq$ 1 beam away). In two cases, HS0105 and HS1549, the companion lies within the field of the Hill et al. (2019) interferometer observations, where they are detected and verified spectroscopically to lie at the QSO redshift. In two other cases a close companion galaxy within the SCUBA2 beam is resolved by Hill et al. (2019). Q0142-100 is part of a lensed system as discussed above. For Q1009+29, 50% of the flux is adopted for the QSO in the subsequent analysis based on the 3mm flux ratio and CO flux ratio presented in Hill et al. (2019). Q0821+3107 and Q1623-KP77, which are not observed by Hill et al. (2019), are statistically consistent with not having a companion. In contrast, Q0142-100 is dominated by a bright companion that clearly offsets the SCUBA-2 data from the QSO position. Therefore only one (i.e. Q1009+29) of the
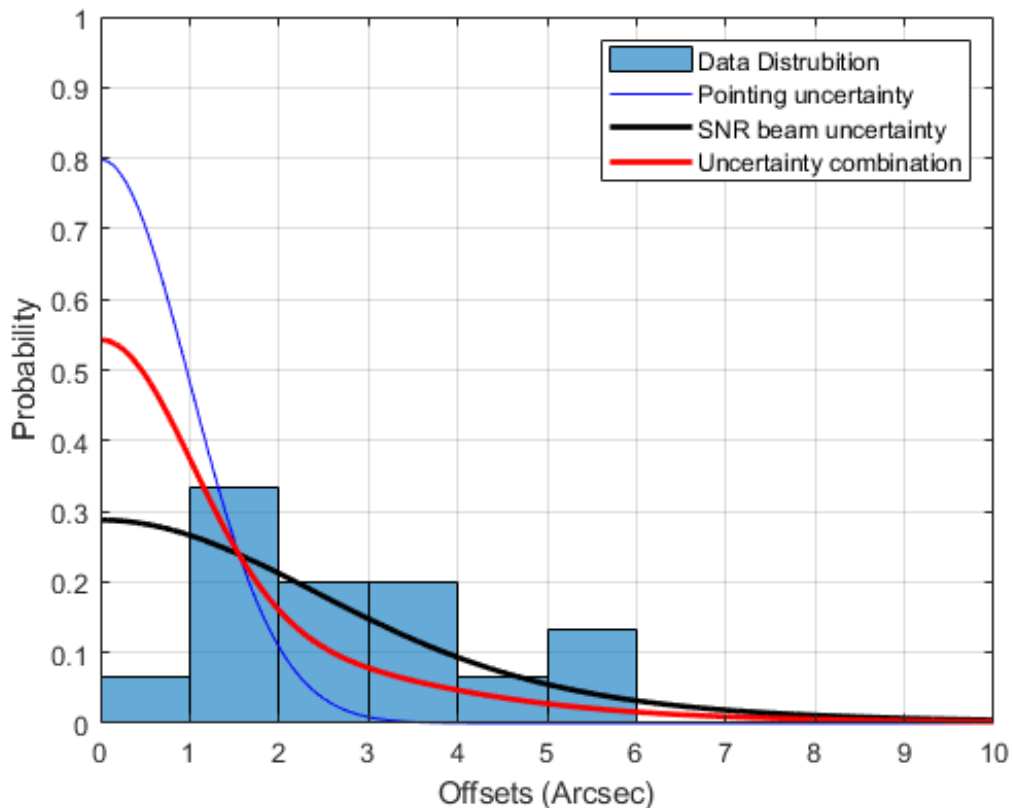
Figure 5.3: Radial offsets from the QSO position (defined by centroiding the IRAC 4.5 μm image) to the SCUBA-2 850 μm position. Overlaid are the $1''$ pointing uncertainty of JCMT (blue), the typical statistical uncertainty associated to the beam size and SNR of the SCUBA-2 detections (black), and the combination of the two (red). The figure shows that the data distribution is consistent with the expected statistical uncertainty in the measurements.

14 (excluding Q0142-100 due to lensing) may be affected by a companion.

5.3 Results

5.3.1 Detection statistics and comparison with other samples

To explore the relationship between star formation and AGN properties, this study compares the HQSO sample with similar $z \simeq 2$ QSO samples in Priddey et al. (2003), Stevens et al. (2005) and Omont et al. (2003). These studies probe the 850 μm (or 1200μm) properties of a population of optically-luminous QSOs over similar redshifts

ranges to the HQSOs in this work, and represent the most relevant comparison samples. To further this study, recent work by Harris et al. (2016) is used to assess whether the statistical relationship between QSO luminosity in the submillimetre and L_{UV} scales to the most extreme for HQSOs. The fitted model presented in Harris et al. (2016) uses Herschel Space Observatory data collected with the Spectral and Photometric Imaging Receiver (SPIRE) at 250μm to 500μm to derive an average relation between star-formation rate and QSO luminosity in the restframe UV. The sample of QSOs presented in this thesis has an unprecedented 850 μm detection rate when compared with other published samples. All 15 of the QSOs are detected at 850 μm and six of them have significant 450 μm counterparts. The studies by Priddey et al. (2003), Stevens et al. (2005) and Omont et al. (2003) have significantly lower submillimetre detection rates, detecting only nine out of 57, six out of 19, and 43 out of 138 sources, respectively at greater than 3σ (or 16–31%). Even after selecting for X–ray absorbed QSOs (Page, Mittaz & Carrera, 2001), only a 50% detection rate was achieved (four out of eight). For a matched sample of X–ray *un*-absorbed QSOs, only one out of 20 was detected significantly at 850 μm to similar depths to the *S2-Web* survey (Page et al., 2006).

An important question becomes why this work detects all 15 of the sources at 850 μm when comparable submillimetre studies of QSOs typically do not find such high detection rates. The 15 HQSOs have a median $L_{UV} \simeq 10^{14} L_{\odot}$, significantly higher than the other QSO samples (e.g., Priddey et al. 2003 – $L_{UV} \sim 7 \times 10^{12} L_{\odot}$ and Stevens et al. 2005 – $L_{UV} \sim 8 \times 10^{12} L_{\odot}$, derived from the source magnitudes using the relationship introduced in section 4.2.1). The high detection success rate in this study may be partially attributed to the higher L_{UV} of these sources, since far-IR luminosity of QSOs appears to scale with L_{UV} to some degree (e.g. Harris et al. 2016).

In addition, for at least two of the sources, the greater submillimetre depth (i.e. integration time) over previous studies allows this work to probe down to the median expected submillimetre luminosity from Harris et al. (2016) (Figure 5.4).

Figure 5.4 shows that the older QSO studies using the predecessor to SCUBA-2 (i.e. SCUBA - Holland et al. 1999) are consistent with recent *Herschel*-SPIRE follow-up of QSOs. The stacked SPIRE detections of QSOs (Harris et al., 2016), suggest that
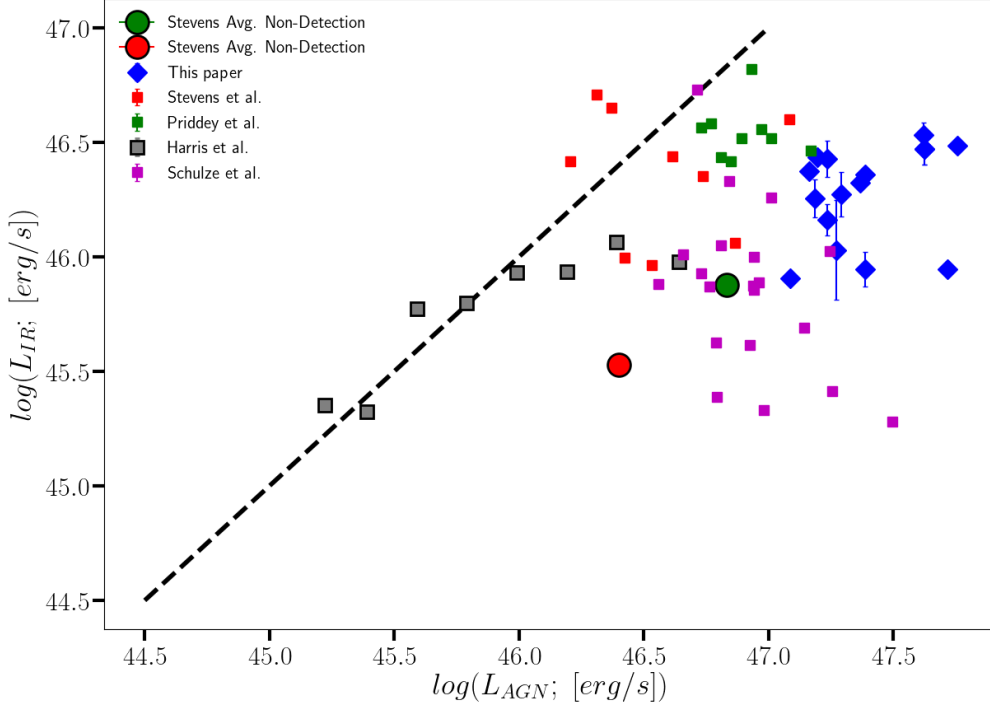
Figure 5.4: L_{IR} as a function of L_{AGN} for the QSO sample, compared with several other studies (Priddey et al. 2003; $1.0 < z < 2.8$, Stevens et al. 2005; $1.5 < z < 2.7$, Harris et al. 2016; $2.2 < z < 3.5$, and Schulze et al. 2019; $0.2 < z < 2.5$) The dashed line is a 1:1 reference for showing the comparison between L_{IR} and L_{AGN} values. The L_{AGN} values are adopted from Hill et al. (2019). This figure shows that the older SCUBA-QSO results are consistent with recent *Herchel*-SPIRE follow-up of the QSOs.

lower $L_{\rm UV}$ QSOs followed up previously with SCUBA would not typically be detected at 850 μm. The average of the Priddey et al. (2003) and Stevens et al. (2005) samples (both detections and non-detections) lie well within the model envelope proposed by Harris et al. (2016). However, at higher $L_{\rm UV}$, this relationship falls well below the HQSO detections in this work. This suggests that there is not a simple extrapolation to higher $L_{\rm UV}$ QSOs and some other process is influencing the star formation and hence submillimetre brightness.

It is important to note that this study uses somewhat deeper 850 μm imaging than was performed with SCUBA in some of the previous studies. Six of the detections would not have been captured in the Priddey et al. (2003) work, however, all of the

HQSOs would have been detected by Stevens et al. (2005) or Page et al. (2001). There are also caveats with the *Hershel*-SPIRE studies relative to this SCUBA-2 study, since measurements at 500 μm, 350 μm, and 250 μm are less favourable than 850 μm for detecting high-redshift ($z > 2.5$) QSOs, due to the relative K-corrections at these wavelengths (e.g., Blain et al. 2002). The confusion noise introduced by *Herschel* with larger beam sizes and higher source densities also make detection of distant objects more difficult. Additionally, the SPIRE surveys also did not cover sufficient area to include such rare high luminosity QSOs as the KBSS sample ($L_{\mathrm{UV}} \sim 10^{14} \mathrm{L}_{\odot}$), and thus the targeted 850 μm data set used in this work is unique in this regard.

5.3.2 Dust mass

Dust mass is a useful quantity because it has recently been demonstrated that M_{d} may act as a useful proxy for the mass of the entire molecular ISM (e.g., Scoville et al. 2014). The dust mass M_{d} of a galaxy can have a large uncertainty because it requires knowledge of its dust temperature. The dust mass is better estimated from a single long-wavelength observation than the infrared luminosity L_{IR}, with the uncertainly in M_{d} being at least only linear with T_{d}. In the Rayleigh-Jeans spectral regime that is probed with the 850 μm data, the flux density from a galaxy $S_{850} \propto \nu^{2+\beta} M_{\mathrm{d}} T_{\mathrm{d}}$. Therefore if T_{d} is uncertain to within some factor, then M_{d} is uncertain to within the same factor. By contrast, as is explored in 5.3.3, $L_{\mathrm{IR}} \propto M_{\mathrm{d}} T_{\mathrm{d}}^{4+\beta}$, or equivalently $L \propto S_{850} T_{\mathrm{d}}^{3+\beta}$. Thus an uncertainty in T_{d} corresponds to a proportionally much larger uncertainty in the inferred value of L_{IR}.

Dust mass is calculated for the HQSOs by adopting dust temperatures constrained from the SCUBA-2 flux measurements, or using 40K if only an upper limit on temperature is constrained from the lack of a 450 μm detection, with the dust masses being then treated as lower limits as well. The average dust masses (lower limit) are estimated using this technique for the HQSO sample, yielding $M_{\mathrm{d}} = (5.9 \pm 2.2) \times 10^7$ M$_{\odot}$.

Dust masses and uncertainties that have been derived from dust temperature constraints are listed in Table 1. In Hill et al. (2019), the dust masses are compared directly to the gas masses measured from ^{12}CO(3-2) demonstrating typical gas/dust ratios for submillimetre galaxies (approximately 100), and may suggest the L_{850} is

mostly due to star formation heating the dust, since AGN are not typically identified in submillimetre galaxies as contributing to the L_{IR} in submillimetre galaxies (e.g., Chapman et al. 2005; Alexander et al. 2005).

5.3.3 Luminosities and dust temperatures

Star formation is one of the most complex, yet critical processes that influence galaxy formation and evolution. The amount of star formation activity in a galaxy is typically quantified using the SFR, which is defined as the mass of new stars formed per unit time. For high-redshift galaxies, where individual stars cannot be resolved, it is necessary to estimate the SFR using an indirect measurement of the star formation activity. These measurable quantities, referred to as SF indicators, are calibrated using models to reflect the total amount of star formation in a galaxy. SFR indicators exist over the entire spectrum, however, the most common techniques involve probing the light that has been directly emitted from star formation in the UV or indirectly through absorption and reradiation by dust in the IR. By measuring the UV luminosity of high-redshift galaxies, which is dominated by short-lived, hot massive stars, astronomers are effectively probing the population of young stars. A pivotal paper by Kennicutt Jr (1998b) derives a linear scaling relationship that enables the UV luminosity to be used as a proxy for SFR, assuming the star formation history has remained constant over the past 100 Myr. One of the biggest challenges in determining an estimate of the SFR from L_{UV} measurements is that the dust absorption properties must be accurately modelled.

Dust surrounding the star forming region efficiently absorbs the UV emission and reradiates it in the IR as thermal emission with characteristic temperatures of 30K-50K (Calanog et al., 2013). In submillimetre galaxies, the majority of the UV emission is absorbed by the intrinsically high dust content, rendering it virtually impossible to measure the UV emission. Under the assumption that only young stars are contributing to the dust heating and that all of the UV radiation is absorbed, L_{IR} can be used to derive an approximate quantitative measure of the SFR.

In this work, the IR luminosities and dust temperatures are estimated for all 15 sources to probe the star formation activity. Ideally the IR luminosity would be estimated by probing the IR emission over many different wavelengths to provide a

tighter constraint on the luminosity estimate. One of the biggest challenges in the submillimetre, however, is that the only reliable data typically comes from 850 μm flux measurements. Therefore the 850 μm flux were calibrated to give L_{IR} estimates using an empirical conversion factor of 1×10^{12} per mJy (Barger et al., 2014). The study by Barger et al. (2014) assumes a modified black body with a 40 K dust temperature (T_{d}) template fit through the rest frame $\simeq$ 230 μm wavelengths probed at these QSO redshifts. Studies by Swinbank et al. (2014) and Chapman et al. (2005) suggest that there is only a very narrow range of dust temperatures in submillimetre galaxies, therefore adopting 40K dust temperature is a reasonable place to start.

To assess the validity of applying this single template $\sim$40K scaling of S_{850} to L_{IR} from Barger et al. (2014) to the sample used in this work, a composite SED template presented in Swinbank et al. (2014) is normalized to the SCUBA-2 850 μm measurements. This template combines multi-wavelength data from a large population submillimetre galaxies detected with ALMA, and represents the typical submillimetre galaxy over the z=2-3 redshift range. To illustrate the constraint on T_d provided by the 450 μm flux measurements, figure 5.5 shows the SED template normalized to the redshift and 850 μm flux of the most luminous QSO, HS1549. The observed-frame 850 μm fluxes for all the other QSOs were then shifted to lie on the same template accordingly to their redshifts.

From figure 5.5, it is clear that the $T_{\mathrm{d}} = 40$ K template is too cold to fit the SCUBA-2 data in the six cases where useful constraints from the 450 μm measurements exist. The modified black body curves (assuming an emissivity of β=1.5) were adjusted by increasing T_{d} until the 450μm flux data point was fit. This increase in T_{d} yields a corresponding increase in L_{IR}, which is listed in Table 1. Subsequent analysis adopts these higher luminosities associated with the fits to the 450 μm points, and those with only limits at 450 μm are treated as lower bounds on L_{IR}. For the nine QSOs with only limits measured at 450 μm, if the limit constrains T_{d} to less than 175 K (the hottest detected source in the sample), the limiting T_{d} value is explicitly indicated, otherwise the limit is not listed, since the T_{d} is not constrained to <200 K in any of the other sources. Figure 5.5 shows the modified blackbody curves for all 15 of the HQSOs, with 450 μm non-detections indicated as 3σ upper limits (arrows).

The measurements presented in figure 5.6 show that galaxies hosting these HQSOs
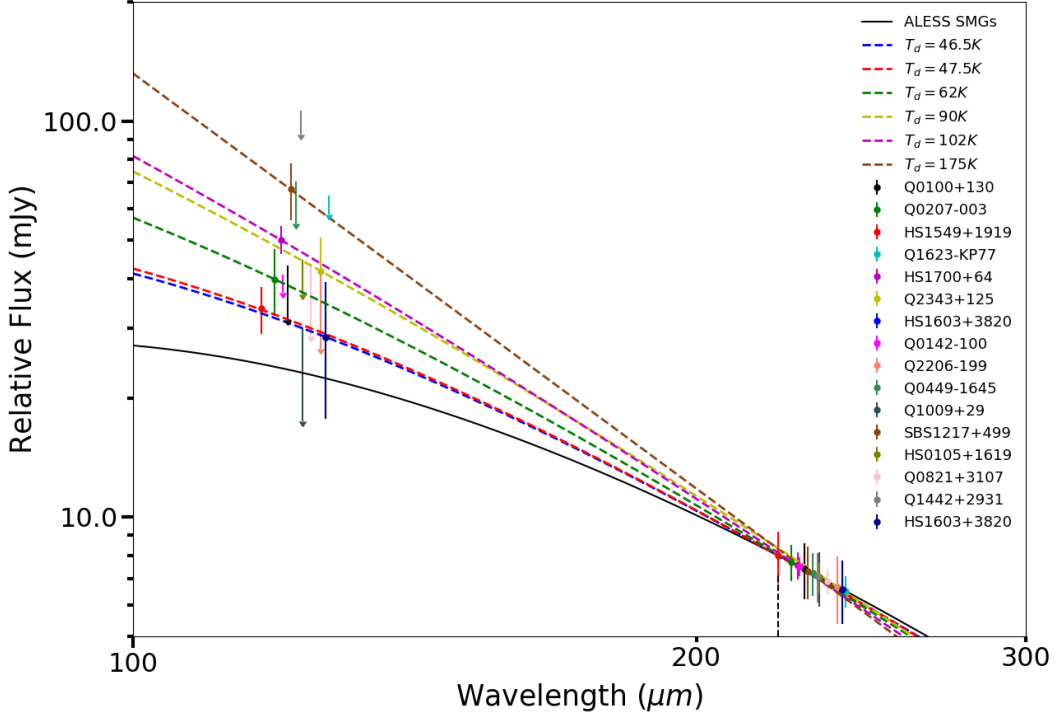
Figure 5.5: Flux at $850\mu m$ relative to the HS1549 QSO versus wavelength for all 15 KBSS sources. The black curve shows the best-fit SED for a sample of ALMA submillimetre galaxies (Swinbank et al., 2014). This template SED is fit to the $850\mu m$ observed flux for HS1549 (*rest wavelength shown by vertical dashed line*) , with all other sources normalized to lie on the same template (shifting their redshift and $850\mu m$ flux) to study the variation in $450\mu m$ measurements. Arrows represent 3σ upper-limits. Modified black body curves are fit to all $450\mu m$-detected sources to determine their dust temperature, as depicted by the coloured dashed lines.

often have hotter dust temperatures than typical submillimetre galaxies, which is discussed further in 5.4. One HQSO, SBS1217+499, stands out with a substantially hotter T_d=175 K value than the other five, which have an average T_d=(67$\pm$24) K, suggesting that star formation alone is unlikely to be the source of the large L_{IR}. With SBS1217+499 included, the sample of six 450 μm-detected HQSOs have an average T_d=(79^{+100}_{-52}) K.

It is important to note that the dust temperatures quoted in this work are not really an average dust temperature across the entire galaxy, but a contribution from a hot inner and cooler outer component of the galaxy. In the central region, the QSO
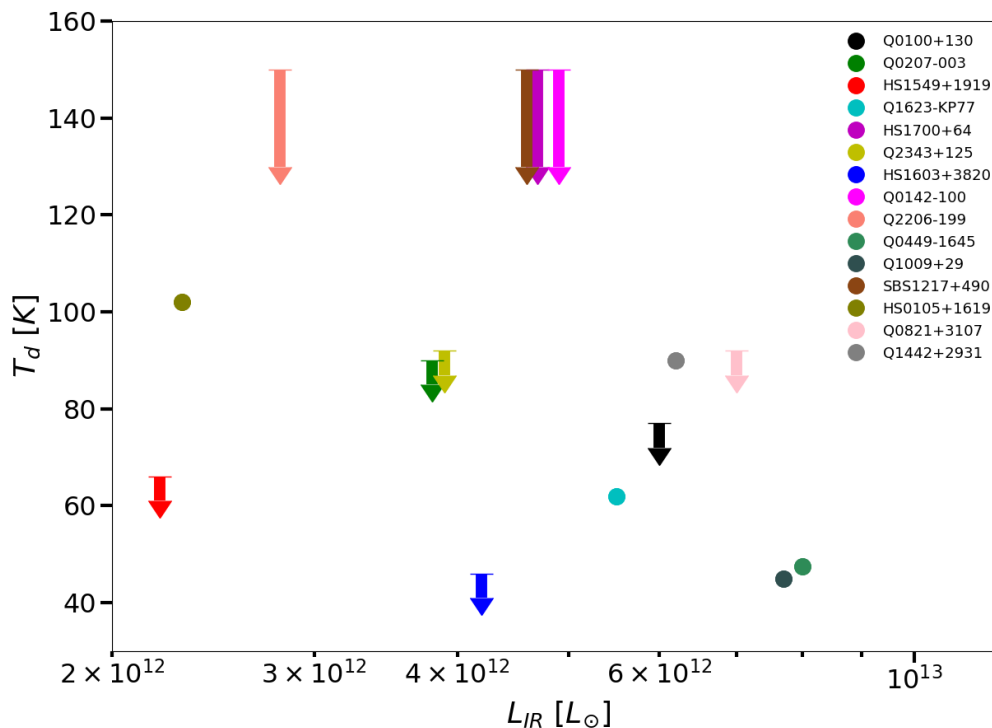
Figure 5.6: Infrared luminosity versus dust temperature. When T_d is constrained from the relative flux measurements the estimated value is adopted, otherwise an upper limit is placed at 150 K. The measurements show that galaxies hosting these HQSOs often have hotter dust temperatures than typical submillimetre galaxies.

will heat a relatively small amount of surrounding dust to a high temperature, but if the host galaxy is sufficiently large and undergoing a starburst phase, there will still be a dominant low temperature gas component. Therefore the 850 μm photometry may still be used to derive a reasonable estimate of the dust mass and SFR. If additional photometry points were available, it would be possible to fit multiple blackbodies to assess the distribution between these two different contributions. Since this study is limited to 850 μm photometry, only a single blackbody fit is adopted.

5.4   Discussion

The results have shown that this sample of HQSOs appear to be more uniformly luminous at far-IR wavelengths compared to larger samples of less UV-luminous QSOs from the literature, where finding far-IR luminosities exceeding a few $\times 10^{12}$ L$_\odot$ is

relatively uncommon (typical detection rates of 15-30%). However, it is important to note that the individually measured far-IR luminosities for the HQSOs are not exceptionally high compared to other QSOs that have been detected at submillimetre wavelengths (e.g. the measurements in this work never exceed $S_{850\mu m}$=10 mJy). Some possible explanations for why the sample as a whole stands out in its IR properties are explored.

It is first of interest to understand if the host galaxies of these HQSOs are significantly different from typical field submillimetre galaxies. In terms of far-IR luminosity, these HQSOs are typically somewhat brighter than field submillimetre galaxies, since they have comparable 850 μm luminosities, but higher dust temperatures on average. One can infer that there may be some heating from the AGN involved in the higher T_d and L_{IR} values. As calculated in 5.3.2, the dust mass carries an uncertainty which is linear with dust temperature. Where the dust temperature has been reasonably constrained, the dust masses are seen to be somewhat larger than those estimated for field submillimetre galaxies with dust temperatures constrained by Kovacs et al. (2006) and Swinbank et al. (2014). This issue was also further explored in Hill et al. (2019), where they concluded from the CO(3-2) emission that several of the HQSOs did depart significantly in gas and dynamical mass properties from field submillimetre galaxies at similar redshifts, although the bulk of the sample did not distinguish itself statistically from the submillimetre galaxies.

By examining the environments of the HQSOs (the density of star forming galaxies surrounding each HQSO), Trainor & Steidel (2012) noted that the halo masses of these HQSOs were not unusually large compared to host halo masses of QSOs with much lower (∼10 times) L_{AGN}. They concluded that the HQSOs were rare AGN bursts in fairly typical galaxy haloes. This result is thus consistent with the findings in this work, and that of Hill et al. (2019), that these HQSO hosts are fairly typical submillimetre galaxies (in terms of L_{IR}, dust mass, gas mass, and line widths as a proxy for dynamical mass) – they are not exceptionally massive galaxies within this dusty star forming population. The one difference in HQSO host properties from typical submillimetre galaxies that this study has uncovered is evidence for somewhat hotter dust temperatures, which might be expected with a partial heating of the dust from the bright AGN.

Within the QSO population itself then, it appears that the high UV luminosities of the HQSOs are the only characteristic that correlates with the findings of high submillimetre detection rates. The QSOs are also not significantly reddened. With reference to figure 5.7, it should be noted that a confluence of two factors may be contributing to this correlation of high L_{AGN} and L_{IR}. The Harris et al. (2016) characterization of the average L_{IR} of QSOs is consistent with approximately the lower 50% of the sources in L_{IR}. For the remaining 50% which lie above the Harris et al. (2016) envelope, it is noted that the hosts do not need to be nearly as large an outlier as at lower L_{AGN} to be submillimetre galaxies. Thus this bursty phase of the host galaxy may simply be more common at the higher L_{AGN} probed in this work.
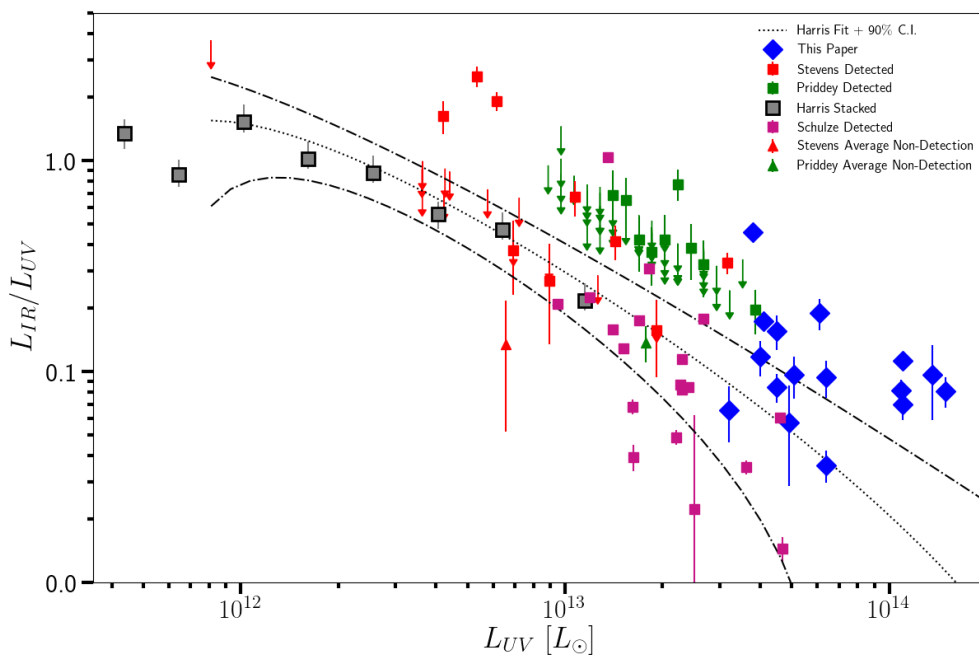
Figure 5.7: Ratio of IR luminosity to UV luminosity for SCUBA-2 detected QSOs from this work and several other submillimetre-luminous quasar samples observed at the same wavelength (Priddey et al. (2003), Stevens et al. (2005), and Schulze et al. (2019)). The blue points show the data from this study, while red, green, and magenta show the data from Stevens et al. (2005) and Priddey et al. (2003), and Schulze et al. (2019) respectively. For these samples, a detection threshold of 3σ is considered. Grey squares with black borders are stacked SFR data from Harris et al. (2016) and black lines depict the adopted models based on fits to *Herschel*-SPIRE stacking on QSOs and its 90% confidence interval.

Kim & Im (2019) find that high-redshift (z $\geq$ 6) quasars with low Eddington ratios (defined as L/L_{Edd}) and, similarly high L_{IR}, have UV spectrum being consistent with no extinction. The authors interpret these low Eddington ratio quasars as being at the end of their nuclear activities, while their host galaxies continue to form the bulk of their stars. By contrast, this study also finds high L_{IR} in these HQSOs, but with what are likely very high Eddington ratios since the host galaxy masses presented in Hill et al. (2019) imply typical BH masses and the high L_{AGN} therefore being close to the Eddington limit.

An additional possibility to explain the large submillimetre continuum emission detected in these KBSS QSOs is that there is often a neighbouring submillimetre-luminous galaxy within the SCUBA-2 beam. If the neighbouring galaxy is merging with the target galaxy, one might expect elevated levels of star formation. Major mergers are frequently linked to massive bursts of star formation (e.g., Tacconi et al. 2008; Engel et al. 2010), which in turn generate large amounts of submillimetre radiation from starlight reprocessed as dust. Therefore, one might expect that merger events in these QSOs are important.

Hill et al. (2019) explored this issue further, finding directly faint offset companion submillimetre galaxies to four of the HQSOs, and further that many of the CO lines of the HQSOs were clearly double peaked, possibly indicating a close merging submillimetre galaxy companion to the HQSO. Three of the four offsets were clearly resolved by the SCUBA-2 detections, however, the fourth was blended into the source emission. An important outcome from the Hill et al. (2019) study was the redshifts of the companion sources, confirming that the neighbouring sources were at the same redshift as the target source. In the cases where double peaked CO lines are observed, this may indicate true major merger processes at play. To confirm this and rule out other possibilities will be a topic of future work.

5.5   Conclusions

This work has surveyed a sample of 15 QSOs with $L_{UV} \sim 10^{14} L_{\odot}$, lying within the KBSS fields, as part of the *SCUBA-2 Web* survey with SCUBA-2, detecting all of them at 850μm. Six of these QSOs are detected at 450μm, suggesting these objects have hotter dust temperatures than typical field submillimetre galaxies (e.g., Swinbank

et al. 2014). This is further supported by the observed far-IR luminosities, which imply that the 450μm detections are accordingly higher than typical submillimetre galaxies. The remainder of the HQSO sample do not have strong enough constraints from 450 μm data to limit their dust temperatures relative to field submillimetre galaxies.

The main findings of this work are that:

• The WISE IR colours of the HQSOs are slightly redder than catalogued sources with a comparable redshift range.

• The 100 per-cent submillimetre detection rate contrasts with previous attempts to measure the far-IR output of QSOs which is typically 10-30 %, and at best achieved 50 per-cent in a sample of X-ray absorbed QSOs.

• A confluence of two factors may be contributing to the correlation of high L_{AGN} and L_{IR}. The Harris et al. (2016) characterization of the average L_{IR} of QSOs is consistent with approximately the lower 50% of the sources in L_{IR}. For the remaining 50% which lie above the Harris et al. (2016) envelope, it is noted that the hosts do not need to be nearly as large an outlier as at lower L_{AGN} to be submillimetre galaxies. Thus this bursty phase of the host galaxy may simply be more common at the higher L_{AGN} probed in this work.

• These HQSOs have comparable 850 μm flux densities to typical field submillimetre galaxies from SCUBA-2 surveys (Geach et al., 2017), implying comparable dust masses. Compared to studies of large samples of QSOs at rest frame far-IR wavelengths, the majority (13/15) of the KBSS QSOs are outliers with larger far-IR luminosities than average. These are consistent with the strongest outliers from other surveys of QSOs at 850μm which are individually detected. However, in this highest range of $L_{UV} \sim 10^{14}$ $L_{\odot}$ probed by the KBSS QSOs, a larger proportion of the sample is found to be outlying from the general QSO population, implying activity in the hosts appears to accompany the most luminous phases or largest black hole masses of QSOs.

• Several of 850μm detections show sizeable offsets from the QSO, significant enough that at least part of the 850 μm luminosity may not represent emission from the QSO host, but rather a companion SMG. This has been verified indirectly in several cases by the ^{12}CO survey of these sources in Hill et al. (2019), where a second CO(3-2)

emitter was detected offset from the QSO.

5.6   Future Work: AO Follow-Up of the HQSO Sample

The idea of performing AO on distant QSOs was briefly introduced in section 4.3.5. Since furthering the work presented in this chapter will involve performing AO follow-up of the 15 HSQSO's, it is instructive to provide an outline of the anticipated process of resolving the host galaxies and their properties.

5.6.1   Introduction

Since the bright central QSO often outshines the host galaxy by several orders of magnitude, resolving the faint emission from background star formation presents a significant observational challenge. To probe the underlying processes in the host galaxy, the PSF of the QSO must be accurately modelled and removed. For ground-based telescopes, modelling the PSF can be quite challenging due to the short time scales over which atmospheric conditions cause the PSF to vary. For this reason, astronomers typically use space-based imaging systems to observe the host galaxy and model the relatively stable QSO PSF and can then be subtracted. As we move to high redshift objects (i.e. z>2), such as the ones explored in this work, additional challenges associated with the size of the host galaxy make it increasingly difficult to disentangle the QSO from the host galaxy. For redshifts greater than z = 1, the distant galaxies become quite small, having angular scales on the same order as the PSF halo created by either ground-based atmospheric seeing conditions or space-based resolution and sensitivity limits. To address these issues and begin to resolve the host galaxy, astronomers look to a combination of near-infrared integral field spectroscopy (IFS) and laser-guide star AO to remove the overpowering QSO emission. IFS observations of unresolved QSO emission (i.e. broad-line emission from H-alpha or continuum) provide a useful tool for constructing the QSO PSF, which can then be normalized and subtracted from the various wavelength channels in the ISF data cube.

5.6.2 Observations

The anticipated follow-up studies of the HQSOs in this work will be performed using the Gemini North facility which houses the ALTtitude conjugate Adaptive optics for the InfraRed (ALTAIR) natural/laser guide star AO system and the Near-Infrared Integral Field Spectrometer (NIFS). The NGS guide star magnitude limits for AL-TAIR are 11-12 magnitude stars for full correction, and 15-16 magnitude stars for partial correction. Since the R-band magnitudes of the HQSOs in this work range from 15.6 (HS1549) to 17.5 (Vega magnitude), the sources are not suitable for NGS observations. However, all 5 of the sources are suitable for the LGS mode on Gemini, falling into the low-Strehl correction limits of guide star magnitudes between 15<R<17.5-18.5. Therefore, this work will aim to take a similar approach to that presented in Vanyard et al. 2016, which used the QSOs to perform tip/tilt correction with an artificial on-axis LGS for higher order correction.

5.6.3 Data Analysis – PSF Construction and Subtraction

Resolving the faint host galaxy involves modeling the QSO PSF and subtracting the bright QSO emission from the host galaxy. Following the process outlined in Vayner et al. (2017), this involves characterizing the broad line emission from H-alpha and/or continuum emission coming from the unresolved compact gas region surrounding the central SMBH out to a few parsecs. Multiple spectral channels that encompass the broad line emission are used to construct a pure PSF image of the QSO that can then be used to subtract the QSO contribution from the IFS data cube. Careful consideration is placed on using high signal-to-noise spectral channels that do not contain OH emission lines or host galaxy emission. These channels are all combined to yield the 2D image of the QSO PSF, which is then normalized to the QSO flux at the peak pixel value and then subtracted from the individual channels in the data cube.

5.6.4 Science

After successfully removing the QSO PSF, only the narrow line emission will be present. Previous studies that have analyzed high SNR spectral data from these

types of systems (e.g. Vayner et al. 2017 and Inskip et al. 2011) reveal two distinct narrow lines features: An AGN narrow line region that has been produced by gas residing far away from the central core and narrow line emission from host galaxy itself. In the case of the AGN narrow line region, gas that has been excited by photons within the accretion disk can indicate signs of outflows and shocks. The emission from the host galaxy is typically in the form of an extended disk (approx. 1 arsec FWHM) of rotating stars, and the H-alpha emission line can be used as tracer of kinematics in AGN host. It is expected that both the AGN narrow line region and the host galaxy disk will break up into clumpier structures, which will push the resolution limits of Gemini's 8-meter telescope (approx. 0.2-0.3 arcsec). In future TMT-NFIRAOS observations, the structure within these clumps could be investigated to see if they represent smooth distributions of gas, or fragment into much clumpier structures on the fine scale achievable by NFIRAOS ($\sim$0.02 arcsec), ten times smaller than the apparent size resolved by Keck-OSIRIS AO system used in Vanyner et al. If these star formation regions were found to be similar to giant molecular clouds in our own Milky Way, and nearby galaxies, then we would expect clumping of these structures on scales comparable to the NFIRAOS PSF. Resolving these regions will be important for determining the characteristic scale of star forming regions in these galaxies and will probe the rotating gas at the core of the galaxy to see if it is influenced by the powerful AGN.

Chapter 6

Conclusion

This thesis has presented two independent studies linked to next-generation AO systems and the opportunity to advance both technology developments and our scientific understanding of the distant universe. The development of a novel, low-power integrated solution to scaling driver electronics for high-actuator count deformable mirrors was introduced in Chapter 3. While many industries have moved towards the adoption of integrated circuit technologies, this approach has yet to be employed in ground-based AO systems. Given that there have been recent developments in this field to produce MEMS-based DM solutions, the next natural step is to provide a compatible driver architecture that can scale with these high-actuator count devices. Through successful co-development of these two technologies, next generation AO systems will enable large-diameter telescopes to achieve their full resolution and sensitivity potential, moving us into a new era of astronomy. The device presented in this thesis was designed and fabricated using the ams 0.35 μm HV process technology, resulting in a 9-channel driver IC prototype optimized for use with a low-voltage, low-current MEMS DMs. Design parameters were derived from the functional requirements imposed by the Thirty Meter Telescope International Observatory (TIO), which has a Canadian-led AO instrument development team. This work was recognized as one of the key technology development areas necessary to reduce the cost and complexity of highly multiplexed MOAO systems. By minimizing the total number of HV transistors and implementing gate protection strategies, the IC driver presented in this work was able to achieve the necessary drive voltages and actuator stroke to comply with these requirements. The IC was shown experimentally to provide $\pm$ 20 μm of stroke on a Lorentz Force MEMS actuator using a $\pm$5 mA current in a 0.1T magnetic field. To maximize the potential of these devices, packaging and integration avenues with the MEMS DM were also explored at the end of this chapter.

Future instrument development avenues will include increasing the dynamic range

of the IC to accommodate large-stroke applications, pairing the IC with a fully populated MEMS array plus mirror membrane to study the impact on stroke, and scaling the device such that it can drive a full 25×25 actuator array. Once these fundamental requirements are met, further investigation into packaging and integration techniques will be explored. This step will be necessary to reduce the contribution from parasitic elements and device signal routing complexity for high-actuator count applications. Upon successful integration, a prototype 25×25 element device will be deployed on an 8-10-metre class telescope to characterize on-sky performance before being tested on a 30-metre class telescope.

A population of rare, extremely bright HQSOs, and their host galaxy environments were explored as part of the SCUBA-2 Web Survey. This study used submillimetre data that were collected using SCUBA-2 on the JCMT to follow-up optical observations of 15 fields known to contain some of the brightest QSOs ever observed. The HQSOs are interesting because they lie within a redshift range known to contain a peak in star formation and AGN activity, making them excellent targets to study both processes simultaneously. To assess the relationship between star formation in the host galaxy and the role of the central QSO, the link between IR luminosity and the very high UV luminosity was explored. In general, the QSOs were found to have comparable IR luminosities to typical submillimetre galaxies. However, when compared with a broader sample of QSOs from the literature, this work finds that the majority of the HQSOs are outliers with larger IR luminosities than expected in normal star forming galaxies. In cases where a hotter than normal dust temperature was able to be constrained from 450 μm detections, it was concluded that star formation alone is unlikely to be the only source of the observed IR luminosity. One possibility to explain the high IR luminosities observed in these sources is that accretion onto a central SMBH is contributing to the observed luminosities. An additional possibility is that a neighboring submillimetre luminous galaxy is merging with the target galaxy. Results from Hill et al. (2019) support the latter by directly observing offset companion galaxies in 5 of the HQSOs and finding many instances of clearly double peaked CO lines. Further investigation into the mechanism by which these sources are achieving elevated IR luminosities will require the ability disentangle the host star formation process from the overpowering central QSO activity. The increase

in resolution and sensitivity that will be possible with AO-enabled, large diameter telescopes presents an optimal solution to decomposing the different contributions to the overall emission. Given that all 15 of the target sources include a bright QSO, they represent an ideal population to perform AO follow-up studies, using the central QSO as a guide star.

To further characterize the host environments of these high-redshift HQSOs from ground-based observatories will require a new generation of AO system optimized for large diameter telescopes. A first step towards this effort will be the first light AO instrument, the Narrow Field InfraRed Adaptive Optics System (NFIRAOS), that will be deployed on the TMT. Using AO-assisted imaging, NFIRAOS will be capable of achieving 15 milli-arcsec resolution in the H-band at 1.6 μm. This level of spatial resolution will allow for the characterization of the host galaxy much closer to the central QSO than would be possible with an 8-metre telescope. Moreover, the use of a future generation instrument like the Infrared Multi-Object Spectrograph (IRMOS) planned for TMT, will allow for observations of faint double nuclei in the ionized gas of the ISM, confirming an ongoing merger as implied by the double peaked CO lines in Hill et al. (2019). The work presented in this thesis is critical to such developments by significantly reducing the cost and complexity of the highly multiplexed MOAO architectures used in these systems. The low-voltage, low-current MEMS DM with IC driver electronics concept presented in Chapter 3 is recognized as an essential development avenue for future TMT MOAO type instruments.

Bibliography

Alexander D., Bauer F., Chapman S., Smail I., Blain A., Brandt W. N., Ivison R., 2005, The Astrophysical Journal, 632, 736

Antonucci R., 1993, Annual review of astronomy and astrophysics, 31, 473

Babcock H. W., 1953, Publications of the Astronomical Society of the Pacific, 65, 229

Barger A., et al., 2014, The Astrophysical Journal, 784, 9

Barnes J. E., 2004, Monthly Notices of the Royal Astronomical Society, 350, 798

Benson A., Bower R., Frenk C., Lacey C. G., Baugh C., Cole S., 2003, The Astrophysical Journal, 599, 38

Berta S., Lutz D., Genzel R., Förster-Schreiber N., Tacconi L., 2016, Astronomy & Astrophysics, 587, A73

Blain C., 2012, PhD thesis

Blain A. W., Smail I., Ivison R., Kneib J.-P., Frayer D. T., 2002, Physics Reports, 369, 111

Blain A. W., Combes F., Draine B. T., 2006, The Cold Universe: Saas-Fee Advanced Course 32, 2002. Swiss Society for Astrophysics and Astronomy. Vol. 32, Springer Science & Business Media

Blanton M. R., Roweis S., 2007, The Astronomical Journal, 133, 734

Bloechl M., Bataineh M., Harrell D., 2004, in IEEE SoutheastCon, 2004. Proceedings.. pp 123–146

Calanog J., et al., 2013, arXiv preprint arXiv:1304.4593

Casey C. M., 2012, Monthly Notices of the Royal Astronomical Society, 425, 3094

Casey C. M., Narayanan D., Cooray A., 2014, Physics Reports, 541, 45

Cattaneo A., Bernardi M., 2003, Monthly Notices of the Royal Astronomical Society, 344, 45

Chapin E. L., et al., 2011, Monthly Notices of the Royal Astronomical Society, 411, 505

Chapin E. L., Berry D. S., Gibb A. G., Jenness T., Scott D., Tilanus R. P., Economou F., Holland W. S., 2013, Monthly Notices of the Royal Astronomical Society, 430, 2545

Chapman S. C., Blain A., Smail I., Ivison R., 2005, The Astrophysical Journal, 622, 772

Chapman S., et al., 2015a, Monthly Notices of the Royal Astronomical Society: Letters, 449, L68

Chapman S., et al., 2015b, Monthly Notices of the Royal Astronomical Society, 453, 951

Chernichenko D., Kushnerov A., Ben-Yaakov S., 2012, in Electrical & Electronics Engineers in Israel (IEEEI), 2012 IEEE 27th Convention of. pp 1–4

Choudhuri A. R., 2010, Astrophysics for physicists. Cambridge University Press

Ciotti L., Ostriker J. P., 2012, in , Hot Interstellar Matter in Elliptical Galaxies. Springer, pp 83–120

Croom S. M., Smith R., Boyle B., Shanks T., Miller L., Outram P., Loaring N., 2004, Monthly Notices of the Royal Astronomical Society, 349, 1397

Da Cunha E., Charlot S., Elbaz D., 2008, Monthly Notices of the Royal Astronomical Society, 388, 1595

De Vaucouleurs G., 1959, in , Astrophysik iv: Sternsysteme/astrophysics iv: Stellar systems. Springer, pp 275–310

Delvecchio I., et al., 2014, Monthly Notices of the Royal Astronomical Society, 439, 2736

Dempsey J. T., et al., 2013, Monthly Notices of the Royal Astronomical Society, 430, 2534

Draine B. T., 2006, The Astrophysical Journal, 636, 1114

Dubois Y., Gavazzi R., Peirani S., Silk J., 2013, Monthly Notices of the Royal Astronomical Society, 433, 3297

Elbaz D., et al., 2011, Astronomy & Astrophysics, 533, A119

Elia D., Pezzuto S., 2016, Monthly Notices of the Royal Astronomical Society, 461, 1328

Engel H., et al., 2010, The Astrophysical Journal, 724, 233

Esposito S., et al., 2011, in Astronomical Adaptive Optics Systems and Applications IV. p. 814902

Fabian A., Celotti A., Erlund M., 2006, Monthly Notices of the Royal Astronomical Society: Letters, 373, L16

Farrah D., et al., 2013, The Astrophysical Journal, 776, 38

Ferrarese L., Merritt D., 2000, The Astrophysical Journal Letters, 539, L9

Fried D. L., 1965, josa, 55, 1427

Geach J., et al., 2017, Monthly Notices of the Royal Astronomical Society, 465, 1789

Gebhardt K., et al., 2000, The Astrophysical Journal Letters, 539, L13

Genel S., et al., 2014, Monthly Notices of the Royal Astronomical Society, 445, 175

Granato G. L., De Zotti G., Silva L., Bressan A., Danese L., 2004, The Astrophysical Journal, 600, 580

Guanziroli F., Bassoli R., Crippa C., Devecchi D., Nicollini G., 2012, IEEE Journal of solid-state circuits, 47, 686

Harris K., et al., 2016, Monthly Notices of the Royal Astronomical Society, 457, 4179

Harrison C. M., 2016, Observational constraints on the influence of active galactic nuclei on the evolution of galaxies. Springer

Hildebrand R. H., 1983

Hill R., et al., 2019, Monthly Notices of the Royal Astronomical Society, 485, 753

Hogg D. W., Baldry I. K., Blanton M. R., Eisenstein D. J., 2002, arXiv preprint astro-ph/0210394

Holland W. S., et al., 1999, Monthly Notices of the Royal Astronomical Society, 303, 659

Holland W., et al., 2013, Monthly Notices of the Royal Astronomical Society, 430, 2513

Hopkins P. F., Hernquist L., Martini P., Cox T. J., Robertson B., Di Matteo T., Springel V., 2005, The Astrophysical Journal Letters, 625, L71

Hubble E. P., 1926, , 64, 321

Hughes D., Robson E., Dunlop J., Gear W., 1993, Monthly Notices of the Royal Astronomical Society, 263, 607

Inskip K., Jahnke K., Rix H.-W., Van de Ven G., 2011, The Astrophysical Journal, 739, 90

Ivison R., Smail I., Blain A., Kneib J.-P., Frayer D., 1999, Astrophysics and Space Science, 266, 285

Jenness T., Stevens J. A., Archibald E. N., Economou F., Jessop N., Robson E., 2002, Monthly Notices of the Royal Astronomical Society, 336, 14

Jenness T., Currie M. J., Tilanus R. P., Cavanagh B., Berry D. S., Leech J., Rizzi L., 2015, Monthly Notices of the Royal Astronomical Society, 453, 73

Kennicutt Jr R. C., 1998a, Annual Review of Astronomy and Astrophysics, 36, 189

Kennicutt Jr R. C., 1998b, The Astrophysical Journal, 498, 541

Kim Y., Im M., 2019, , 879, 117

King A., 2003, The Astrophysical Journal Letters, 596, L27

Koller J. G., Athas W. C., 1992, in Proceedings of Physics of Computation Workshop. pp 267–270

Kormendy J., Beckman J., Colina L., Netzer H., 1993, Consejo Superior de Investigaciones Científicas (Madrid, 1993)

Kovacs A., Chapman S., Dowell C., Blain A., Ivison R., Smail I., Phillips T., 2006, The Astrophysical Journal, 650, 592

Kuiper G. P., 1938, The Astrophysical Journal, 88, 472

Lacaille K. M., et al., 2019, Monthly Notices of the Royal Astronomical Society, 488, 1790

Lam C. K., Tan M. T., Cox S. M., Yeo K. S., 2012, IEEE Transactions on Power Electronics, 28, 3870

Lin C. W., Hsieh B.-S., Lin Y. C., 2009, in Proceedings of the Conference on Design, Automation and Test in Europe. pp 1397–1402

Lin L., Wu X., Zhao J., Zhao M., 2012, in 2012 IEEE International Conference on Electron Devices and Solid State Circuit (EDSSC). pp 1–3

Lutz D., 2014, Annual Review of Astronomy and Astrophysics, 52, 373

Madau P., Dickinson M., 2014, Annual Review of Astronomy and Astrophysics, 52, 415

Madau P., Ferguson H. C., Dickinson M. E., Giavalisco M., Steidel C. C., Fruchter A., 1996, Monthly Notices of the Royal Astronomical Society, 283, 1388

Madec P.-Y., 2012, in Adaptive Optics Systems III. p. 844705

Magorrian J., et al., 1998, The Astronomical Journal, 115, 2285

Max C. E.,

McLure R. J., Dunlop J., 2002, Monthly Notices of the Royal Astronomical Society, 331, 795

Murray N., Quataert E., Thompson T. A., 2005, The Astrophysical Journal, 618, 569

Noeske K., et al., 2007, The Astrophysical Journal Letters, 660, L43

Noll R. J., 1976, JOsA, 66, 207

Ohyama Y., Taniguchi Y., Shioya Y., 2004, The Astronomical Journal, 128, 2704

Oke J. B., Sandage A., 1968, The Astrophysical Journal, 154, 21

Omont A., Beelen A., Bertoldi F., Cox P., Carilli C. L., Priddey R. S., McMahon R. G., Isaak K. G., 2003, Astronomy & Astrophysics, 398, 857

Page M., Mittaz J., Carrera F. J., 2000, Monthly Notices of the Royal Astronomical Society, 318, 1073

Page M., Mittaz J., Carrera F., 2001, Monthly Notices of the Royal Astronomical Society, 325, 575

Page M., Carrera F. J., Ebrero J., Stevens J., Ivison R., 2006, arXiv preprint astro-ph/0610229

Park B., 2018

Park B., Afsharipour E., Chrusch D., Shafai C., Andersen D., Burley G., 2017, Journal of Micromechanics and Microengineering, 27, 085005

Park B., Afsharipour E., Chrusch D., Shafai C., Andersen D., Burley G., 2018, Sensors and Actuators A: Physical, 280, 197

Pilbratt G., et al., 2010, Astronomy & Astrophysics, 518, L1

Pitchford L., et al., 2016, Monthly Notices of the Royal Astronomical Society, 462, 4067

Priddey R. S., Isaak K. G., McMahon R. G., Omont A., 2003, Monthly Notices of the Royal Astronomical Society, 339, 1183

Reddy N. A., Steidel C. C., Pettini M., Adelberger K. L., Shapley A. E., Erb D. K., Dickinson M., 2008, The Astrophysical Journal Supplement Series, 175, 48

Richards G. T., et al., 2002, The Astronomical Journal, 123, 2945

Richards G. T., et al., 2006, The Astronomical Journal, 131, 2766

Rudie G. C., et al., 2012, The Astrophysical Journal, 750, 67

Saitoh T. R., Daisaka H., Kokubo E., Makino J., Okamoto T., Tomisaka K., Wada K., Yoshida N., 2009, Publications of the Astronomical Society of Japan, 61, 481

Sandage A., 1986, Astronomy and Astrophysics, 161, 89

Sandell G., 1994, Monthly Notices of the Royal Astronomical Society, 271, 75

Sawicki M., 2002, The Astronomical Journal, 124, 3050

Schaye J., et al., 2014, Monthly Notices of the Royal Astronomical Society, 446, 521

Schulze A., et al., 2019, Monthly Notices of the Royal Astronomical Society

Scoville N., et al., 2014, The Astrophysical Journal, 783, 84

Scoville N., et al., 2016, The Astrophysical Journal, 820, 83

Silk J., Rees M. J., 1998, arXiv preprint astro-ph/9801013

Sluse D., Hutsemékers D., Courbin F., Meylan G., Wambsganss J., 2012, Astronomy & Astrophysics, 544, A62

Steidel C. C., Adelberger K. L., Giavalisco M., Dickinson M., Pettini M., 1999, The astrophysical journal, 519, 1

Steidel C. C., Adelberger K. L., Shapley A. E., Erb D. K., Reddy N. A., Pettini M., 2005, The Astrophysical Journal, 626, 44

Steidel C. C., Bogosavljević M., Shapley A. E., Kollmeier J. A., Reddy N. A., Erb D. K., Pettini M., 2011, The Astrophysical Journal, 736, 160

Stevens J. A., Page M., Ivison R., Carrera F. J., Mittaz J., Smail I., McHardy I., 2005, Monthly Notices of the Royal Astronomical Society, 360, 610

Swinbank A., et al., 2014, Monthly Notices of the Royal Astronomical Society, 438, 1267

Tacconi L., et al., 2008, The Astrophysical Journal, 680, 246

Thomas H. S., Currie M. J., 2014, Starlink Cookbook, 21

Trainor R. F., Steidel C. C., 2012, The Astrophysical Journal, 752, 39

Trainor R., Steidel C. C., 2013, The Astrophysical Journal Letters, 775, L3

Trakhtenbrot B., Lira P., Netzer H., Cicone C., Maiolino R., Shemmer O., 2017, The Astrophysical Journal, 836, 8

Tsai C.-W., et al., 2015, The Astrophysical Journal, 805, 90

Tyson R. K., 2015, Principles of adaptive optics. CRC press

Vayner A., Wright S. A., Murray N., Armus L., Larkin J. E., Mieda E., 2017, The Astrophysical Journal, 851, 126

Wall J. V., Pope A., Scott D., 2008, Monthly Notices of the Royal Astronomical Society, 383, 435

Wang L., et al., 2013, Monthly Notices of the Royal Astronomical Society, 431, 648

Yu Q., Tremaine S., 2002, Monthly Notices of the Royal Astronomical Society, 335, 965